PLASMONIC METASURFACES UTILIZING EMERGING MATERIAL PLATFORMS

by

Krishnakali Chaudhuri

A Dissertation

Submitted to the Faculty of Purdue University

In Partial Fulfillment of the Requirements for the degree of

Doctor of Philosophy

School of Electrical & Computer Engineering

West Lafayette, Indiana

August 2019

THE PURDUE UNIVERSITY GRADUATE SCHOOL
STATEMENT OF COMMITTEE APPROVAL

Dr. Alexandra Boltasseva
School of Electrical and Computer Engineering
Dr. Vladimir M. Shalaev
School of Electrical and Computer Engineering
Dr. Alexandar V. Kildishev
School of Electrical and Computer Engineering
Dr. Zhihong Chen
School of Electrical and Computer Engineering

Approved by:

Dr. Dimitrios Peroulis
Head of the Graduate Program

To Baba,

For you believed in me, I believed in myself

ACKNOWLEDGEMENTS

I would like to thank my amazing adviser Professor Alexandra Boltasseva. Thank you for giving me this wonderful opportunity to be a part of your academic family and for providing constant support and encouragement through the last few years at Purdue. Without you and your guidance, reaching here today wouldn't have been possible.

I would also like to thank my other adviser Professor Vladimir Shalaev for sharing his vast knowledge and wisdom with students. I truly learned a lot from you and your kind words have always encouraged me to push forward.

I would like to thank Professor Alexander Kildishev for his constant availability and guidance in the theoretical and numerical parts of my research.

It has been a great honor to collaborate with Prof. Yury Gogotsi and his research group members Mohamed Alhabeb and Kathleen Maleski from Drexel University through last few years. I would like to thank them for sharing their resources and knowledge with us.

I would like to express my sincere gratitude and appreciation to all the current and former research group members- Dr. Amr E. Shaltout, Dr. Zhuoxian Wang, Aveek Dutta, Soham Saha, Dr. Naresh Emani, Dr. Clayton DeVault, Shaimaa I. Azzam, Xiaohui Xu, Dr. Justus Ndukaife, Deesha Shah, Di Wang, Sajid Choudhury, Dr. Urcan Guler, Dr. Jongbum Kim, Dr. Rohith Chandrasekhar, Dr. Mikhail Shalaginov, Dr. Nathaniel Kinsey, Dr. Zakxylyk Kudyshev, Harsha Reddy, Samuel Peana, Dr. Alexei Lagoutchev, Dr. Simeon Bogdanov, Sarah Chowdhury, Maowen Song, and more. Specifically, I would like to thank Dr. Amr Shaltout for his incredible help and guidance in shaping my first project on metasurfaces. Thanks to my friend Aveek Dutta for always being there for valuable discussions. Thanks to all my friends, colleagues and staff members of Birck Nanotechnology Center- for contributing to my success here at Purdue.

Finally, I would like to thank my father ('Baba') and mother ('Maa') for their unremitting love and unconditional support and encouragement every step of the way. And I thank my beautiful sister ('Di') for being there for me through each day of this journey.

And lastly, with all my heart I feel blessed that Rahul stepped into my life along the way on this journey. He held my hand amidst the all the chaos and have been the constant source of strength through it all every day. I can't ever, thank him enough. Just that, - you're the best thing that has happened to me. With you, life is beautiful.

TABLE OF CONTENTS

LIST OF FIGURES

LIST OF TABLES

ABSTRACT

Author: Chaudhuri, Krishnakali. PhD
Institution: Purdue University
Degree Received: August 2019
Title: Plasmonic Metasurfaces Utilizing Emerging Material Platforms
Committee Chair: Alexandra Boltasseva

Metasurfaces are broadly defined as artificially engineered material interfaces that have the ability to determinately control the amplitude and phase signatures of an incident electromagnetic wave. Subwavelength sized optical scatterers employed at the planar interface of two media, introduce abrupt modifications to impinged light characteristics. Arbitrary engineering of the optical interactions and the arrangement of the scatterers on plane, enable ultra-compact, miniaturized optical systems with a wide array of applications (e.g. nanoscale and nonlinear optics, sensing, detection, energy harvesting, information processing and so on) realizable by the metasurfaces. However, maturation from the laboratory to industry scale realistic systems remain largely elusive despite the expanding reach and vast domains of functionalities demonstrated by researchers. A large part of this multi-faceted problem stems from the practical constraints posed by the commonly used plasmonic materials that limit their applicability in devices requiring high temperature stability, robustness in varying ambient, mechanical durability, stable growth into nanoscale films, CMOS process compatibility, stable bio-compatibility, and so on.

Aiming to create a whole-some solution, my research has focused on developing novel, high-performance, functional plasmonic metasurface devices that utilize the inherent benefits of various emerging and alternative material platforms. Among these, the two-dimensional MXenes and the refractory transition metal nitrides are of particular importance. By exploiting the plasmonic response of thin films of the titanium carbide MXene ($Ti_3C_2T_x$) in the near infrared spectral window, a highly broadband metamaterial absorber has been designed, fabricated and experimentally demonstrated. In another work, high efficiency photonic spin Hall Effect has been experimentally realized in robust phase gradient metasurface devices based on two different refractory transition metal nitrides –titanium nitride (TiN) and zirconium nitride (ZrN). Further, taking advantage of the refractory nature of these plasmonic nitrides, a metasurface based

temperature sensor has been developed that is capable of remote, optical sensing of very high temperatures ranging up to 1200^{o}C.

CHAPTER 1. METASURFACES AND EMERGING MATERIALS

Maturation of sophisticated and precisely controlled micro- and nano-fabrication techniques has led us to the current era of efficient, miniaturized technologies. Within just a few decades, in electronics, the room-sized devices have shrunk to palm fitting ones and in optics, made possible to control light in manners unprecedented before. Ability to determinately control the light-matter interaction through engineered material blocks, brought forth the development of the game-changing technology of three-dimensional (3D) metamaterials. With 3D metamaterials, it was possible to control and manipulate not only light but also thermal and even acoustic waves propagation which weren't deemed possible with naturally existing individual material systems[1–3]. By artificially structuring material systems into sub-wavelength sizes building blocks, the effective dielectric and magnetic properties can be manipulated efficiently to in turn control the responses of these systems to incident electromagnetic radiation. In addition to tuning of the inherent material properties, one can also control shapes, sizes, spatial arrangements etc. of the building blocks to enable desired functionalities. 3D metamaterials alone have demonstrated, in the past, many interesting phenomena in nanoscale optics e.g. negative index of refraction[4–6], high resolution imaging[7], invisibility cloaking[8,9], optical black holes[10,11], super radiance[12,13], hyperbolic optical properties[14–16], and so on.

A more specific sub-class of metamaterials are the two-dimensional metasurfaces. Distinct from 3D metamaterials, metasurfaces enable many new and interesting physical phenomena and opens a whole new paradigm of applications. To obtain full control of amplitude and phase of light, metasurfaces employ sub-wavelength sized scatterers arranged on a planar surface. The scatterers are metallic and/or dielectric materials based sub-wavelength sized nano structures or apertures. While in conventional optics, phase control is achieved through continuous phase accumulation, in metasurfaces, optical resonators placed at the interface of two media, give access to an abrupt phase change to the impinged electromagnetic waves[17].

Based on use of materials and physical nature of the light matter coupling at play, metasurfaces can be broadly classified into two main categories, namely plasmonic and dielectric. As the name suggests the dielectric metasurface uses structured dielectric surfaces whereas the plasmonic one rely more on plasmonic (metallic) counter-parts. Surface plasmon is a quantum of free electron oscillation that couples to light and exists at the interface of a metallic and dielectric

media.[18] In metallic nanostructures, localized oscillations of plasmons can confine electromagnetic energy to nano-scale volumes and enhance light matter interactions by orders of magnitude[19,20]. Plasmonic metasurfaces, therefore, employ such metallic nanostructures to manipulate light propagation. Electric field of incident electromagnetic radiation interacts with the free electrons within a nano structure and creates charge polarization. A restoring Coulomb force acts on the electron cloud displaced in space by the excited plasmon oscillation. The metal nanostructure, therefore, behaves as an electric dipole oriented along the electric field direction. The resonance condition of such localized plasmon oscillations depend strongly on the size, geometry, composition, dielectric environment, and spatial separation of neighboring nanostructures[21,22].

As in conventional optics, light propagation is governed usually by the gradual accumulation of phase along the light path controlled by the refractive index and surface geometry of the carrying media. On the other hand, phased arrays at radio frequencies are well-known method of the past, where an array of antennas controlled by external signals to control radiation pattern that can introduce abrupt phase shifts along the optical path to steer electromagnetic wave[23]. Frequency selective surface (FSS) in microwave and radio waves used similar principles in a two-dimensional planar structure[24]. By individually controlling each unit cell antenna element, a specifically tailored wave front can be generated. By engineering the phase shifts, a FSS can function as a lens[25,26], a reflector[27], or an absorber[28] and more. Metasurfaces were developed as an optical counterpart of the FSS, with optical nano-scale antenna arrays to control phase profile on a surface. For passive devices, as long as the change of phase occurs within a small thickness, effect of wave propagation this this layer is negligible and the phase discontinuity can be regarded as inherently contained in the surface. Under this circumstances, the standard Snell's law that characterizes reflection and refraction characteristics, is rewritten into a more generalized form[17].

Physical realization of a nanostructured surface with a phase profile is a non-trivial problem. Nanoscale plasmonic antenna elements and their arrangement in space can both be designed accurately to obtain a required phase profile at a surface. Anisotropic rectangular brick antennas showing distinct responses to orthogonal polarization components of incoming radiation are commonly used[29,30]. Another type is the V-shaped antennas, that break the symmetry in geometry and offers a wide number of degrees of freedom to modify the phase distribution at the interface[31]. In recent past, numerous demonstrations have utilized the planar metasurface architecture to realize functional flat optical devices such as ultra-compact lenses[32–35], wave-plates[36–38], planar

holograms[39–42], spectrometers[43], polarization rotators[30,44,45], etc. These planar devices benefit from a simpler fabrication process flow, ultra-compact make, and wide applicability in many areas of the miniaturized technology market. Historically, noble metals (Au, and Ag) were used in most of all plasmonic devices due to their high quality plasmonic resonances in the visible and infrared frequency domains. However, they pose some serious limitations when it comes to durability, compatibility with the standard CMOS processing techniques and stability at high temperature, which is inevitable when electromagnetic energy is confined to small volume in the vicinity of metals.

Despite a range of exciting and promising laboratory demonstrations of achievable optical functions, maturation to real-life applications remain largely elusive. Optical losses in plasmonic metals deteriorate the efficiency of devices and are regarded as one of main challenges of metal-based material platform. In an ideal plasmonic material, low losses and high metallicity is desired, which is physically unrealizable. In addition, even with negligible bulk optical losses, nano-patterning leads to truncation of the magnetic component of the impingent electromagnetic wave interacting with the free electrons in the metal. The stored magnetic energy therefore converts into the kinetic energy of the free electrons and leads to loss termed as landau damping [46]. Therefore, plasmonic metasurfaces suffers inherently from lower efficiencies as compared to dielectric based counterparts however benefits from tighter field confinement, broader operating bandwidth, and significantly smaller device footprint. In application of plasmonic metasurfaces therefore is a trade-off between field confinement and optical loss. Plasmonic metasurfaces are particularly beneficial for applications where the optical losses can be of use for a particular functionality, for example in energy harvesting in absorbers[47] or nanoscale heaters[48,49]. Numerous examples of emerging applications for plasmonic metasurfaces exploits the ability to strongly confine electromagnetic field to nanoscale volumes such as, enhanced non linearity[50], and harmonic generation,[51–53] detection sensitivity improvement[54,55], color filters and displays[56,57], absorbers[58–60], thermal emitters[61], energy harvesting systems like photocatalysis[62], solar and thermo-photovoltaics[63], heat assisted magnetic recording[64], and so on.

Conventional noble metals such as gold and silver have been profically used for most of the early metasurface applications owing to their superior optical properties (high metallicity, lower loss) leading to higher quality plasmonic resonances. Silver exhibits good plasmonic properties in the visible frequencies, however, commonly used evaporation deposited

polycrystalline silver, suffers from relatively higher optical losses stemming from electron scattering at the grain boundaries[65,66]. It has been shown experimentally, that gold and silver films when grown ultrathin (on the order of few nanometers), tend to form nano islands. This makes it challenging to use these metals in cases where uniform ultrathin films are required. From the standpoint of on-chip integration of nanophotonic devices, gold and silver are not compatible with the standard silicon based complementary metal-oxide-semiconductor (CMOS) technology, as silver has poor chemical stability and gold acts as a defect inducing contaminant. In addition, these noble metals are soft, malleable with low melting points. When nanostructured, a further degradation in temperature dependent mechanical and structural stability is observed[67]. Consequently, noble metals are not suitable for applications requiring high temperature stability, which poses a dilemma in plasmonics because the localized plasmon oscillations and confined electromagnetic field unavoidably raise local temperatures significantly, at least within the spatial field confinement. Therefore, new, and durable plasmonic materials are deemed necessary for allowing stronger field confinement and high-temperature applications beyond the conventional material capabilities.

For bridging the gap between laboratory test-bench and industrial production of commercial device, reduction in design complexity as well as development of more application oriented material system is imperative. The planar geometry of metasurface supports easier bottom-up fabrication scheme and can be integrated easily into existing planar architecture of on-chip devices. The planar structure provides easier integration for additional functionality such as a dynamic modulation through an external control[68]. Additionally, these two dimensional metamaterials can be designed to embody many different physical processes simultaneously as a tool to enhance efficiency, such as optical trapping using combination of optical, thermal, and an electrical bias force at the same time[69]. The reduced dimensionality of metasurfaces enables new physical effects which do not have volumetric counterparts, such as the relaxation of Snell's law.

Naturally, in the recent past, significant research effort has focused on the development of plasmonic materials overcoming some limitations of Au, Ag etc. Most of these alternatives come from the metal oxides and nitrides families although many other materials have been suggested[70]. Transition metal nitrides[70–72] provide ceramic plasmonic materials, which can tolerate difficult operating environment and very high temperatures and can be fabricated using CMOS compatible processes. Additionally, heavily doped semiconductor oxides[70,73,74] have enabled devices with low

permittivity values in the telecommunications wavelength range which is important for confinement of plasmonic waves as well as near zero permittivity. They also provide an extra degree of freedom of material control through modulation of the free carrier concentration through electrical or optical means[75,76]. This is very promising to be used to build active or reconfigurable metasurfaces.

In the following chapters of this report, we discuss our pursuits in evaluating two of these emerging material platforms in the context of linear metasurfaces-based applications. Chapter 2 and 3 elaborates our study of optical properties of the emerging material class of two-dimensional MXenes and the work of creating a metasurface based broadband absorber utilizing the lossy nature of the titanium carbide MXene. MXenes are a recently developed material class of two dimensional titanium carbides, nitrides, and carbon nitrides[77]. They are chemically synthesized and make up a family of more than 60 predicted and 20 synthesized materials.[78] They are unique in their high metallic conductivity and ability to store charges in the interlayer spaces[79,80]. We demonstrate localized surface plasmon resonances in nanostructures made of a continuous film of titanium carbide ($Ti_3C_2T_x$) MXene. The inherent losses of the material together with its ability to support plasmon resonances in nanostructures have been utilized to design, fabricate and test a broadband absorber metamaterial.

In the next chapter 4, we discuss our work with two prominent members of the refractory metal nitrides' family, namely titanium and zirconium nitride. We have designed and fabricated a classic phase gradient metasurface exhibiting photonic spin Hall Effect[81] utilizing these two metal nitrides. The design uses a unit-cell based on multiple layered stack of metal-dielectric to improve efficiency and demonstrates similar performance to other noble metal based design counterpart. This first demonstration is a key step towards successful integration of refractory metallic nitrides into practical, on-chip, planar metasurface devices.

In a following work, discussed in the following chapter 5, a metasurface has been developed using high temperature stable titanium nitride that will function as a high –temperature sensor device. The sensitive plasmonic resonances increase detection efficiency, while also providing a remotely controlled operation scheme, together with very high detection range (beyond 1200^{o}C).

Chapter 6 discusses briefly the ongoing work of demonstration of a dielectric (TiO_2) based high Q-factor metasurface by realizing bound states in continuum at visible optical frequencies.

CHAPTER 2. STUDY OF OPTICAL PROPERTIES OF MXENES

ABSTRACT

In the past decade, two dimensional (2D) materials have had a significant impact on the physics and optics research community as they are observed to interact with light in a large variety of unique ways. MXenes have been added to this class of 2D in 2011. Ever since their discovery, they have been explored by a growing number of different fields of research, including optics and nanophotonics. In relation to optics, in the past few years, researchers have demonstrated a number of widely useful and interesting features of the MXenes, for example, optical transparency, plasmonic behavior, optical nonlinearity, efficient photo-thermal conversion, tunability of optical response etc. These have led to application of the MXenes in functional metamaterial devices, mode-locked lasers, surface enhanced Raman spectroscopy (SERS), photo-thermal therapy (PTT) and so on. In this chapter, we start by reviewing the theoretical and experimental approaches in studying the optical properties of the MXenes and then discuss the impactful optical device demonstrations.

2.1 Optical Properties of 2D Materials

Ever since the discovery of graphene in 2004[82], the family of two-dimensional (2D) materials has grown steadily. Beyond graphene, transition metal di-chalcogenides, commonly known as TMDs or TMDCs (such as MoS_2, WS_2, WSe_2, $MoTe_2$ etc.)[83], and phosphorene or black phosphorous[84] are particularly notable. Each of these materials exhibit unique characteristics that are reflected in their unusual mechanical, electronic, and optical properties. In a single-to-few layer form, they support distinctly strong light-matter interactions, that can be used as a tool to probe unusual physical processes in such condensed matter systems[85]. Many 2D materials and their hetero-structures are excellent candidates for low power, electrically switchable electronic[86] and optical

devices[87]. In addition, they provide an excellent platform to enhance light matter interactions through effective integration with nanophotonic structures, and inherent polaritonic resonances.[87] Graphene contains a single layer of SP^2 hybridized carbon atoms arranged in a plane in a honeycomb lattice structure. Each 'C' atom contains an extra electron in the p_z orbital. The orbitals of adjacent atoms overlap and interact giving rise to bonding and antibonding states and the corresponding π-bands in graphene[88]. This results in the linear energy-momentum relation experienced by electrons in graphene. Thus, they behave as massless Dirac fermions[88,89], leading to a variety of interesting transport and optical phenomena[85,90]. Linearly dispersive Dirac electrons can interact with a broad bandwidth of photon energies[91] strengthening the potential of the material for many optical applications. The Pauli blocking principle leads to a strong saturable absorption[92] and a strong luminescence that can be created and modulated externally[93,94]. The transmittance of graphene is a function of its fine-structure constant[95], which makes it naturally visible[96] although it is only a fraction of a nanometer thick.

Monolayer transition metal di-chalcogenides (TMDC) consist of a single layer of transition metal atoms placed with a layer of chalcogen atoms on either side, placed in a trigonal prismatic structure. Bulk TMDs are indirect bandgap semiconductors while the monolayers exhibit a direct bandgap lying in the near-infrared (IR) and visible spectral regions. In addition to a broken in-plane inversion symmetry[97], TMDs exhibit tightly bound room temperature stable excitons[98–100] and spin- and valley- selective electronic and optical properties[97,101]. Broken inversion symmetry allows strong nonlinear optical processes such as second harmonic generation (SHG), third harmonic generation (THG) and saturable absorption to exist within the body of ultra-thin layers of TMDs[102–104]. Planar photonic and plasmonics are coupled to the strong excitonic systems to realize unique exciton-polaritons[105], ultra-thin gain material for lasing[106], and even single photon emitters[107].

More recently, black phosphorous (BP) was reintroduced to the optics and electronics community as an anisotropic 2D material[84,108,109]. The layer dependent direct bandgap of BP ranges from 0.3 eV in bulk to 1.5 eV in monolayer form. This bandgap falls in between the gapless graphene and large gap TMDs establishing it as an excellent material platform for near- and mid-IR optics and optoelectronics. Unlike graphene, it has an orthorhombic crystal structure consisting of puckered layers of phosphorous atoms[110]. This also exhibits an anisotropic electronic and optical response with respect to the armchair and zigzag direction of the lattice. The structural anisotropy

extends itself to unique anisotropic excitons, electron mobility, optical absorption, thermal conductivity, and plasmons[111–115]. The band gap, the exciton binding energies, optical absorption spectrum, and linear polarization energy window can be tuned widely by changing the number of layers in a stack of BP. In addition, likewise to other 2D materials, BP exhibits strong saturable absorption type nonlinearity[116–118].

MXenes are a relatively new addition to this exciting class of 2D materials which have drawn a great amount of interest due to their tunable properties and wide range of applications[119]. Although discovered 7 years ago, synthesis and isolation of single to few layer flakes of MXene are scalable, tunable, and processable into variety of solvents in comparison to other extensively studied 2D materials [120] (also see Chapter 2.4). More than 60 MXene compositions have been predicted with over 20 experimentally synthesized, making them among the fastest growing and the most diverse 2D materials[78]. MXene has been explored in a variety of applications including transparent electrodes[121], metal ion batteries[122], supercapacitors[123–125], and electromagnetic interference shielding[126,127] due to its high electrical conductivity[78]. Utilizing the optical properties of MXene, other applications such as effective light to heat conversion[128], saturable absorption for mode-locked lasing[129], surface-enhance Raman scattering (SERS)[130,131], and plasmonic broadband absorber[132], and photonic diodes[133] have also been demonstrated. However, the most studied MXene, titanium carbide, $Ti_3C_2T_x$, has been the material of choice for most of all these studies and optical properties of other MXenes are yet to be investigated.

In this chapter, we will overview the theoretical and experimental approaches to study optical properties of MXenes, and discuss some of the optical device demonstrations based on MXenes.

2.2 Theoretical Predictions of Electronic and Optical Properties of MXenes

In the last decade, a number of groups have focused on the understanding of the physical behaviors of MXenes with the intention integrating them into nanoscale devices[134]. In particular, MXene compounds with $Ti_{n+1}X_n$ (X=C, N and n=1,2) were studied extensively in both theory and experiments to understand and predict the characteristics with changing elements, lattice structures, and surface functionalization groups (fluorinated or hydroxylated derivatives). Optical response of a materials is intricately related to its structural as well as electronic properties, e.g. band-to-band electronic transitions result in enhanced optical absorption at certain frequencies. Theoretical

framework can provide a complete understanding of such potential mechanisms behind material optical response and can also predict behavior of other similar systems. This is particularly useful for the rapidly growing family of synthesized MXenes.

H. Lashgari et al. has used density functional theory formulation to calculate the density of states (DOS) and band structures, which is used to predict respective optical behavior of single [135]. Electronic properties confirm the metallic nature of most $Ti_{n+1}X_n$ MXenes with their valence and conduction bands overlapping with the Fermi level. The 3d orbital of the Ti in $Ti_{n+1}X_n$ MXenes contributes largely to the metallicity near the Fermi level.

H. Lashgari et al. made use of the full-potential linearized augmented plane wave (FP-LAPW) method[136] and Random Phase Approximation (RPA) formalism[137] to calculate the optical response (complex dielectric function (ε), reflection, absorption, and electron energy loss function) of the two-dimensional $Ti_{n+1}X_n$ MXene compounds such as Ti_2C, Ti_2N, Ti_3C_2, Ti_3N_2. The imaginary part of the dielectric function, *Im* ε, is calculated as

$$Im\ \varepsilon_{ij}^{[interband]}(\omega) = \frac{h^2e^2}{\pi m^2\omega^2}\sum_n \int dk\ \langle\psi_k^{C_n}|p^i|\psi_k^{V_n}\rangle\ \langle\psi_k^{V_n}|p^j|\psi_k^{C_n}\rangle\ \delta\left(E_k^{C_n} - E_k^{V_n} - \omega\right)$$

Equation 2.1

where $\psi_k^{V_n}$ corresponds to the occupied valence band levels, $\psi_k^{C_n}$ represents the empty conduction band levels over k points of the first Brillouin zone, $E_k^{C_n}$ and $E_k^{V_n}$ stands for the unoccupied conduction band and occupied valence band states respectively, and ω is the frequency of the interacting electromagnetic wave. Using inverse transformation, the corresponding real part is obtained as

$$Re\ \varepsilon_{ij}^{[interband]}(\omega) = \delta_{ij} + \frac{2}{\pi}P\int_0^\infty \frac{\omega' Im\varepsilon_{ij}(\omega)}{(\omega')^2-\omega^2}$$ Equation 2.2

where P is the principal value of the integral.

Contributions from the intra-band transitions are calculated separately as

$$Im\ \varepsilon_{ij}^{\{intraband\}}(\omega) = \frac{\Gamma\omega_{pl,ij}^2}{\omega(\omega^2+\Gamma^2)}$$ Equation 2.3

$$Re\ \varepsilon_{ij}^{\{intraband\}}(\omega) = 1 - \frac{\omega_{pl,ij}^2}{\omega(\omega^2+\Gamma^2)}$$ Equation 2.4

Where, $\omega_p^2 = \frac{ne^2}{\varepsilon_o m}$ Equation 2.5

ω_p^2 denotes the plasma frequency, n is the free carrier or electron concentration, m is the effective electron mass, and Γ is the damping/loss term in the Drude model. The complete dielectric function with contribution from both inter- and intra-band electronic transitions can therefore be written as

$$\varepsilon(\omega) = \varepsilon^{\{intraband\}}(\omega) + \varepsilon^{[interband]}(\omega) \quad \text{Equation 2.6}$$

Monolayers of $Ti_{n+1}X_n$ (X=C, N and n=1,2) contain a hexagonal space group symmetry with three atoms for Ti_2X and five for Ti_3X_2. Due to this symmetry, under the excitation of an electric field parallel (E||x) and perpendicular (E||z) to the *c*-axis, the complex dielectric function (ε) tensor has only three nonzero components $\varepsilon^{xx}(\omega) = \varepsilon^{yy}(\omega)$, and $\varepsilon^{zz}(\omega)$. Figure 2.1 (a) plots the corresponding dielectric tensors. The peaks in the *Im* ε has direct contributions from the different inter- and intra- band electronic transitions. The real part of the ε, *Re* ε, is then obtained using the the *Kramers-Kronig* relations[138,139], shown in Figure 2.1 (a)- inset. With the knowledge of the frequency dependent complex dielectric function, other important optical parameters such as the reflectivity and absorption coefficient can be calculated. The absorption spectrum (A) is proportional to the total contribution of inter-band transitions from filled valence band states to empty conduction band levels (Figure 2.1 (b)).

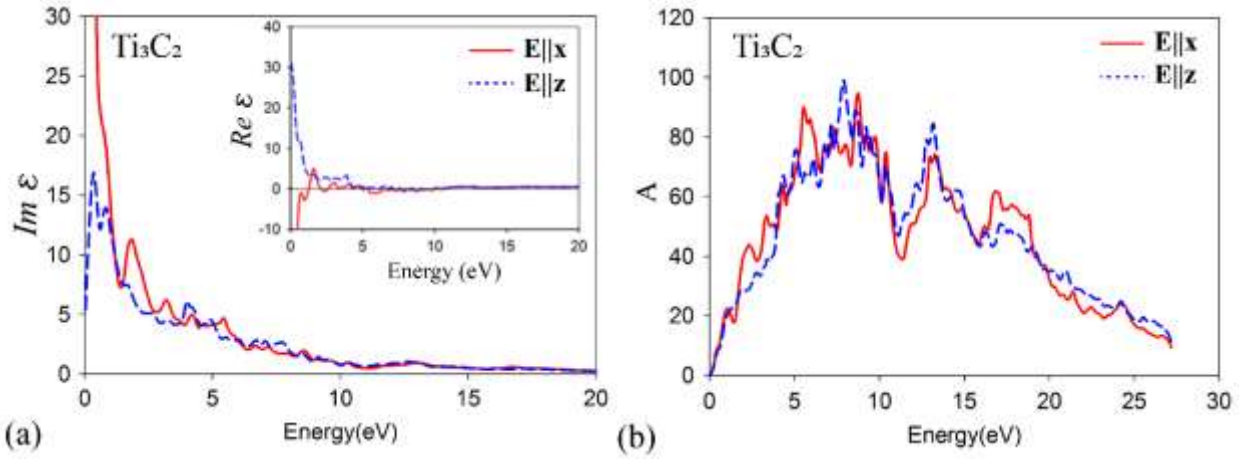

Figure 2.1 Calculated (a) imaginary part of the dielectric function (inset shows the real part), (b) absorption coefficient for Ti_3C_2 MXene. The two non-zero components of the dielectric tensor $\varepsilon^{xx}(\omega)$ and $\varepsilon^{zz}(\omega)$ for electric field perpendicular (E||x) and parallel (E||z) to c-axis are represented by the solid red and dashed blue line. Adapted from [135]

The outermost transition metal atoms of a single layer of MXene were experimentally found to be passivated by functional groups, such as –F, -O, and –OH, due to the synthesis

processes as described in Chapter 2.4. Recent studies have shown that the surface functionalization can largely affect both structural and electronic properties of MXenes[140–142]. It has also been demonstrated that specific attributes of the MXene properties (electron transport, capacitance etc.) can be tailored by tuning the surface functional groups. A recent work by *G. Berdiyorov* discussed the effect of the functionalization on the optical properties of $Ti_3C_2T_2$ MXene, where 'T' represents a surface functional group (either –F, -O or –OH), using computational methods[143]. Here, the susceptibility tensor $\chi(\omega)$ of the MXene monolayer system is calculated using the well-known Kubo-Greenwood formula[144], often used to calculate electronic conductivity in materials. The frequency dependent complex dielectric properties of the material system are derived from the electric susceptibility as $\varepsilon(\omega) = Re\,\varepsilon + Im\,\varepsilon = 1 + \chi(\omega)$.

Real and imaginary parts of the frequency dependent dielectric functions were calculated and compared for the experimentally shown functional groups, $Ti_3C_2F_2$, $Ti_3C_2(OH)_2$, $Ti_3C_2O_2$, and pristine Ti_3C_2 in Figure 2.2 (a, c). Considerable variation in the dielectric functions are noted with the variation of the functional groups and spectral range of interest. Using the dielectric functions, the frequency dependent refractive index, *n*, and extinction coefficient, *k*, and absorption spectra has been calculated for $Ti_3C_2T_2$ (shown in Figure 2.2 (b, d)). Significant differences between functional groups were observed in the absorption spectra, particularly in the lower photon energy regime, showing the importance of how the surface groups impact eventual properties. The peaks observed agree well with the various inter- and intra- band transitions obtained through density functional theory (DFT) predictions reported previously[135,141].

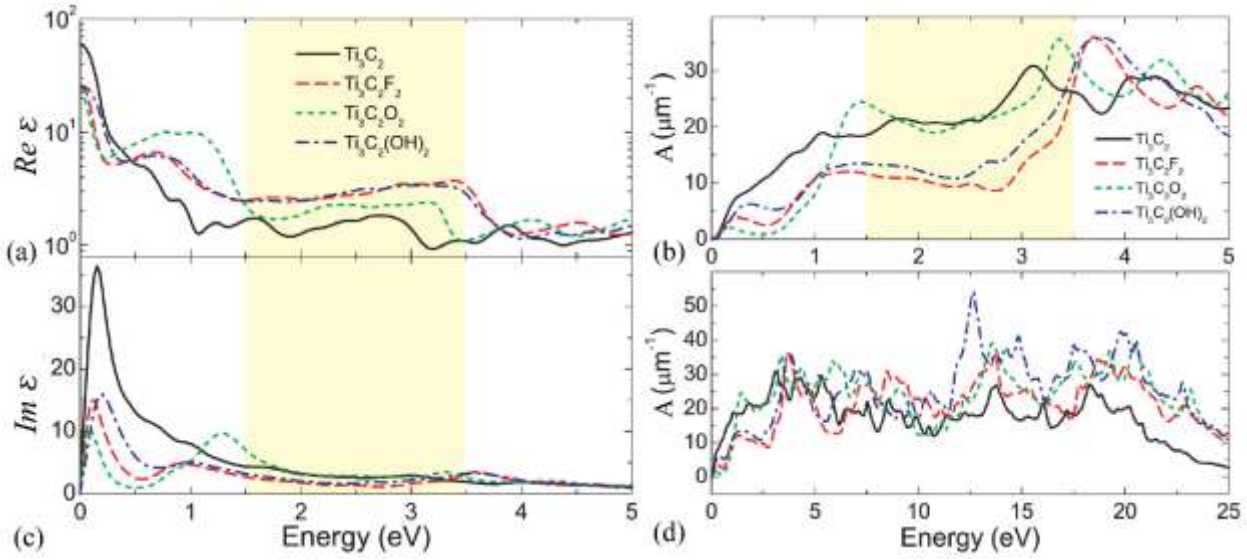

Figure 2.2 Real (a) and imaginary (b) part of the dielectric function as a function of incident photon energy for Ti_3C_2 MXene with different surface functionalization groups as indicated (shaded area shows visible range of the spectrum). Absorption spectra of $Ti_3C_2T_x$ MXene for small (0-5 eV) (a) and large (0-25 eV) (b) range of photon energy. Adapted from [143]

2.3 MXenes for Plasmonics: Theory and Experiments

MXenes initially were evaluated largely for energy storage applications owing to their 2D structure and ion intercalation properties. However, the growing family of materials are gaining significant attention from the optics and optoelectronics community as well due to their high metallic conductivity[79] and large transmissivity[145] in single to a few layer form. This has led to the exploration of MXene-based transparent electrodes[121,145], photo-thermal therapy (PTT)[146,147], and effective electromagnetic interference shielding[126]. More recently, other interesting attributes such as plasmonic properties[79,132], and large nonlinearities[129,148] have been observed and implemented in various experimental devices.

Here, we will be focusing largely on the most well studied MXene, Ti_3C_2. It shows high metallic conductivity, down to a single monolayer, and has been investigated for bulk and surface plasmons. Plasmons are collective electron oscillations formed of light-matter interaction[18]. Surface plasmons (SP) are electron oscillations that exists at a metal-dielectric interface at the surface of the metal whereas bulk plasmons (BP) can form deeper within the body of a free carrier containing system[149].

In early investigations of plasmons in Ti_3C_2 MXene, theoretical and experimental measurements of the electron energy loss function were used. Following the formalism discussed in section 4.2.2, *H. Lashgari et al.* calculated the electron energy loss function for a single layer of pristine Ti_3C_2 MXene as in Figure 2.3 (a)[135]. The interaction of a fast moving electron through a solid may experience an energy loss through mechanisms such as band transitions (inter- and intra-) or excitation of plasmons. The contribution of such interactions can be identified by utilizing electron energy loss spectroscopy (EELS). *V. Mauchamp et al.* experimentally measured the high resolution electron energy loss spectra (HREELS) in the energy range of 0.2 -30 eV along with an *ab initio* theoretical frame work to demonstrate detectable SPs in nanoscale MXene systems[150]. Results from their calculations are summarized in Figure 2.3 (b). Electron energy loss spectra (EELS) was obtained for $Ti_3C_2T_2$ MXene, with nanoscale multilayered sheets with thickness ranging from 5 nm to 45 nm. The EELS spectra were compared both experimentally and theoretically. In calculations, the surface functionalization ('T') is assumed to be either exclusively -OH, or –F, however, it should be noted that -OH, -O, and -F terminations can be present on the surface of the material as hydrofluoric etching techniques were used. Strong SP modes are observed at very low energy (less than 10 eV) range.

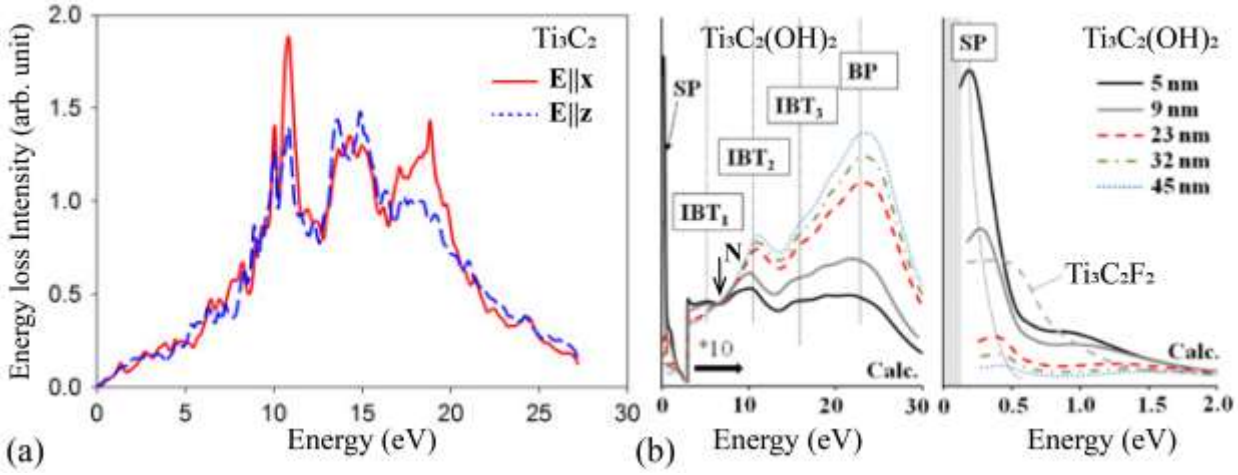

Figure 2.3 Calculated EELS for (a) Ti_3C_2 MXene for electric field perpendicular (E||x) and parallel (E||z) to c-axis (adapted from [135]), and (b) $Ti_3C_2(OH)_2$ multilayered MXene of different thicknesses. The spectra are normalized at 7 eV (labeled N) and are magnified by a factor of 10 above 3 eV to make the bulk plasmon (BP) peaks better visible. Figure on the right shows a detailed view of the surface plasmon (SP) energy region. Inter-band transition peaks are labeled by IBTs. Adapted from [150].

This can be explained by weak inter-layer coupling that exists between neighboring layers in a few-layer thick multilayer $Ti_3C_2T_2$ stack. In contrast to other 2D materials, such as graphene, h-BN, or TMDs, with increasing layer thickness, electronic band structure and valence band electron densities are modified, resulting in considerable spectral shifts in the BP energy (peak position)[151].

Experiments reveal the dominance of SP contribution over the BP counterpart for $Ti_3C_2T_2$ thicknesses up to 45 nm or approximately 45 single layer sheet of Ti_3C_2 (assuming each $Ti_3C_2T_2$ layer is ~1 nm). This observation is in contrast to other plasmonic metals, such as aluminum or gold, where the SP vanishes for thicknesses greater than 30 nm, suggesting metallic Ti_3C_2 exhibits different optical properties in comparison to aluminum or gold[152,153]. The small value of the SP damping factor (extracted from the full width at half maximum (FWHM) of the Gaussian peak fitted to the SP peak in Figure 2.4 (a, c)), weak inter-layer coupling, and lower probability of low energy SP decay into higher energy inter-band transition channels lead to a reduction in bulk plasmon excitation probability and in turn, a SP dominance in the $Ti_3C_2T_2$ system (Figure 2.4 (b)). Thus, SP resonances in MXene can be tuned by altering the electronic structure while controlling the thickness. Electronic band structure of $Ti_3C_2T_2$ MXene can be modified by the surface functionalization groups ‘T’ added during the synthesis process. Changing the functionalization from –OH to –F, the peak of the inter-band transition can be frequency shifted, allowing existence of higher energy SPs.

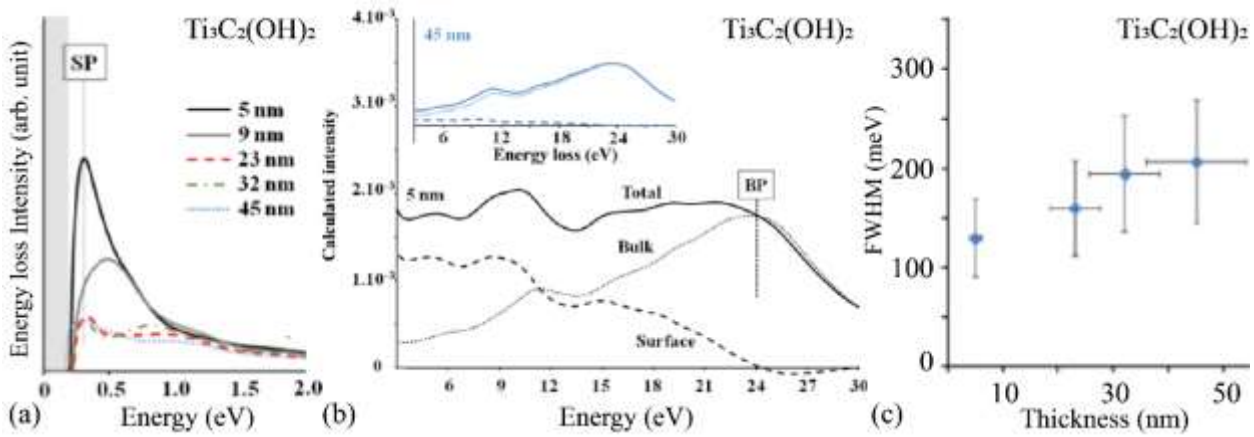

Figure 2.4 (a) Experimentally measured EELS of $Ti_3C_2(OH)_2$ MXene for different multilayered thicknesses indicating the surface plasmon (SP) energy peaks. (b) Surface (dashed) and bulk (dotted) contributions to the total (solid) inelastic cross section of a 5 nm thick $Ti_3C_2(OH)_2$ MXene sample (inset shows same quantities for a 45 nm thick sample). (c) Full width at half maximum (FWHM) extracted from Gaussian fitting of the experimentally recorded SP peak of $Ti_3C_2(OH)_2$ MXene as a function of thickness. Adapted from [150]

Another study has revealed that the strongly metallic and plasmonic behavior is retained in $Ti_3C_2T_x$ MXene thin films as well, in contrast to measuring on multilayered stacks of MXene. The films are made of overlapping arrangements of individual single layer sheets[79]. The experimentally retrieved complex dielectric functions have shown a dielectric to metallic cross-over (*Re* ε falls below 0) at a wavelength of ~1130 nm for MXene films of varying thicknesses (Figure 2.5 (a)). This further corroborates earlier findings that surface plasmon polaritons (SPP) can be excited in the multilayered MXene at near- to mid- IR frequencies.

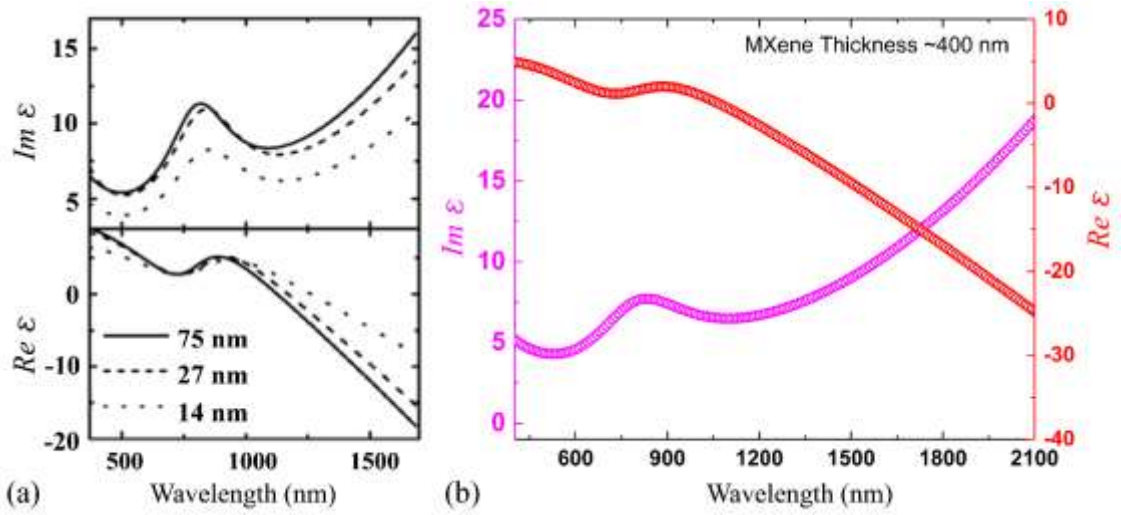

Figure 2.5 Optical properties of spin coated MXene thin films measured using spectroscopic ellipsometry. (a) Imaginary (top) and real (bottom) part of frequency dependent dielectric function ε for different thicknesses of spin-coated $Ti_3C_2T_x$ thin films as indicated (adapted from [79]). (b) Imaginary (left-axis, magenta) and real (right axis, red) part of ε for a 400 nm thick film of $Ti_3C_2T_x$ MXene (adapted from [132]).

More recently, MXene films of much higher thickness (~400 nm) have been used as building blocks of plasmonic metamaterial devices. The spectral dependence of the real and imaginary parts of the dielectric function (ε) were measured (using a variable angle spectroscopic ellipsometer) for the spin coated $Ti_3C_2T_x$ films. A dielectirc to metallic crossover at ~1.07 μm indicates plasmonic behavior at near- and mid- IR for MXene film thicknesses up to 400 nm[132]. Using a Drude-Lorentz model, optical parameters are extracted (shown in Figure 2.5 (b)). Optical properties of the thicker MXene films are qualitatively similar to the previously discussed thinner MXene films[79]. Large *Im* ε or optical losses in the films are attributed in parts to the intrinsic absorption due to interband transitions (at ~5.36 eV (0.23 μm) and ~1.54 eV (0.8 μm))[135] and to losses stemming from surface roughness and bulk disorder related scattering of carriers.

2.4 Mode-locked Laser, PTT and Other Applications

So far, there are a handful of experimental demonstrations of optics devices with MXenes. The notable ones include a plasmonic absorber with nanostructured MXenes, mode-locked laser using MXene saturable absorber, and surface-enhanced Raman scattering substrates using MXene sheets.

In addition to the plasmonic resonances, another significant optical property of 2D MXenes is their large nonlinearities which enable applications in laser science. Controllable optical nonlinearities in different types of materials have led to many interesting phenomena such as second harmonic generation, Kerr effect, optical rectification, four-wave mixing, saturable absorption etc[154]. Many of these play crucial roles in the development of ultra-compact, high power, and ultrafast femtosecond pulsed laser sources. Femtosecond lasers are of critical importance in field such as advanced micromachining, molecular, chemical, and optical spectroscopy techniques, as well as in information processing. In the past few decades, the development of ultrafast lasers has had tremendous impact on industry and research alike.

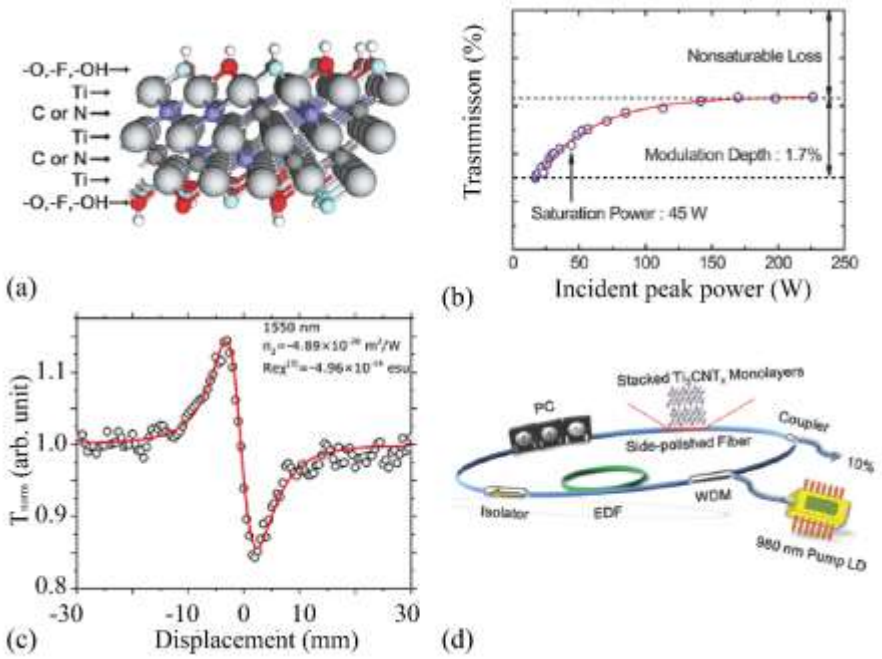

Figure 2.6 (a) The structure of Ti_3CNT_x (Tx: -O, -F, -OH). (b) Measured nonlinear energy-dependent transmission curve of the prepared side-polished fiber with the deposited Ti_3CNT_x monolayer film. (c) Closed aperture Z-scan of MXene $Ti_3C_2T_x$ at 1550 nm wavelength performed to reveal the nonlinear refractive index (n2) and the real part of the third-order nonlinear optical susceptibility (Re $\chi^{(3)}$). (d) Schematic of the ring-cavity erbium-doped fiber laser incorporating the stacked Ti_3CNT_x SAs. Here, PC, EDF, WDM, and LD denote a polarization controller, an Er-doped fiber, a wavelength division multiplexing, and a laser diode, respectively. ((a, b, d) adapted from [129], (c) adapted from [148])

Saturable absorber is one of the key building block of lasers generating high power, ultra-narrow pulses using Q-switching and/or mode-locking methods. In saturable absorbers, the light

absorption is modulated with the intensity of the impinged light as $\alpha(I) = \frac{\alpha_0}{(1+I/I_s)}$, where α_0 is the linear absorption coefficient, I is the incident intensity and I_s is the saturation intensity (defined as the incident intensity at which the absorption coefficient is half of the linear absorption coefficient $\alpha_0/2$. Maximum modulation of absorption coefficient at a specific wavelength of incident radiation for a saturable absorber is termed as the modulation depth. Several 2D materials display outstanding saturable absorption behavior e.g. increased modulation depth and fast recovery time and can be beneficial for mode-locking, Q-switching, pulse shaping in ultra-compact lasers.

Recently, researchers have reported strong saturable absorption behavior in 2D MXenes as well. This was first reported for Ti_3CNT_x MXene by *Y. Jhon et al* (schematic of molecular structure of Ti_3CNT_x is shown in Figure 2.6 (a))[129]. A mode-locked femtosecond fiber based ring cavity laser was implemented, with a Ti_3CNT_x MXene stack as a saturable absorber. The generated pulse widths are comparable to the best reported TMD based saturable absorbers in lasers[129] (Figure 2.6 (b)). $Ti_3C_2T_x$ MXene has also been studied for its broadband, nonlinear optical response in the near-IR regime (between 800-1800 nm), measured using Z-scan measurement technique by *X. Jiang et al* (Figure 2.6 (c))[148]. The maximum nonlinear coefficient is found to be on the order of 10^{-21} m^2/V^2, comparable or even exceeding in magnitude to the values reported for other 2D materials. The calculated effective nonlinear optical absorption coefficient of $Ti_3C_2T_x$ is two orders of magnitude higher than MoS_2 and black phosphorus, indicating an efficient optical switching ability. Peak saturation intensity is extracted to be at a few tens of GW/cm^2 for the near-IR spectral range. High intensity illumination induced nonlinear refractive index for $Ti_3C_2T_x$ MXene, measured using an open aperture Z-scan, is also comparable in magnitude (~ -10^{20} m^2/W for the near-IR spectral window) to previous reports on graphene (Figure 2.6 (d)). When implemented in a fiber based cavity, the $Ti_3C_2T_x$ MXene based saturable absorber generates mode-locked, ultra-short (159 fs) duration pulses. The fundamental origin and thickness dependence of the saturable absorption behavior of $Ti_3C_2T_x$ MXene is further studied by *Y. Dong et al*[133]. Open aperture Z-scan measurements on MXene films of varying thickness (5-100 nm) revealed thickness dependence of the modulation depth. This arises from the plasmon induced increase in absorption at incident energies above the dielectric to metallic crossover frequency after which the free carrier oscillation becomes more favorable. A maximum modulation depth of 50% is measured at incident intensity of 70 mJ/cm^2 for a 67 nm thick $Ti_3C_2T_x$ MXene, indicating a higher damage threshold

than other 2D materials. A $Ti_3C_2T_x$ MXene based photonic diode that achieves nonreciprocal transmission of nanosecond laser pulses is demonstrated[133].

Apart from strong plasmonic resonances and nonlinear behavior, MXenes also exhibit a large optical transparency window and strong surface sensitive optical characters. Large transmission coefficient of few layer stacks of metallic MXenes is promising for applications as transparent electrode materials[121,145]. The ability to dynamically modulate the transmittance of MXene films by chemical intercalation method enables adaptive device designs[145]. On the other hand, the surface plays a crucial role in determining optical properties (including characteristics of surface plasmons) of 2D MXene (see also, section 4.4.2) making them utile for sensing applications. This has led to demonstration of effective surface-enhanced Raman scattering (SERS) substrates based on MXene sheets either in pristine, or in specially synthesized nanoparticle-hybridized form[130,131].

Recently, MXenes have been identified for their efficient and tailorable photo-thermal conversion property and as potential candidates for biomedical applications of photo-thermal therapy or PTT. In the past, many inorganic substances including plasmonic nanoparticles[155], carbon based nanomaterials[156], and other 2D materials graphene[157], MoS_2[158], WS_2[159] etc. have been investigated as novel photo-thermal agents for cancer therapy. And recently, MXene ceramics (such as Ti_3C_2, Ta_4C_3, Nb_2C) have demonstrated extraordinarily high efficiency of converting light to heat energy in ultrathin 2D nano sheets[146,147,160]. Large absorption of electromagnetic energy in the NIR bio window I (750 – 1000 nm) and II (1000 – 1350 nm) causing local hyperthermia can be utilized *in vivo* and *in vitro* that can lead to thermal ablation of affected tumor tissue. As an added benefit, MXenes can be synthesized and surface modified to be photo-thermally stable as well as stable and non-toxic in physiological environment containing many bodily fluids[147,160].

2.5 Conclusion and Outlook

This chapter provides an overview of the recent advances in the field of 2D MXenes for optics and nanophotonics. The unique optical properties of MXenes have enabled fascinating applications such as ultrafast laser pulse generation, broadband absorber, and SERS. We have placed emphasis on the plasmonic properties of $Ti_3C_2T_x$ MXenes which enables plasmonic device designs in the near-IR. Although demonstrations of new device concepts have shown the potential of 2D MXenes

for optical applications, many challenges remain to be overcome and new opportunities should be explored.

One of the main challenges for nanophotonic and plasmonic applications of MXenes is to develop a solid understanding of the optical properties of MXenes, especially the dielectric functions of single to few layer MXenes. Even though there have been reports on the band diagrams and the optical properties of monolayer MXenes through density functional theory (DFT) simulations[135,141,143], the results are yet to be verified by experimental measurements. This requires fabrication of uniform single to few layer MXene films on a large area. Improvements in the optical stability of MXenes flakes, especially for colloidal solutions and single to few layer films, is another great challenge. It has been shown that the environmental and chemical stability of single MXene flakes is dependent on the synthesis and processing method, where the overall stability of single flakes in air can be improved from hours to several days[78,161]. Nevertheless, highly stabilized MXene flakes in longer time periods will provide more reliable device performance.

The recent reports on the large nonlinear response and plasmonic behavior of $Ti_3C_2T_x$ MXene films brings with it further exciting opportunities to explore other members of the MXene family. Even though large nonlinear optical response of MXene films has been observed in a broad wavelength range with z-scan experiments[148], the time dynamics and source of the nonlinearity haven't been studied yet. Carrying out pump-probe experiments could provide us a deep understanding of the nonlinear process in MXene films[75]. Second, in addition to ultrafast laser pulse generation, MXenes could improve the figures of merit of another important type of laser source, random lasers. It has been theoretically predicted that the exotic optical response of 2D materials could offer new avenues to control random lasers due to the extraordinarily low threshold for saturable absorption[162]. The colloidal solution of single to few layer MXene serves as a perfect candidate for the experimental demonstration due to its ease of fabrication[163]. And lastly, due to the larger carrier density, $Ti_3C_2T_x$ MXene shows plasmonic behavior in the near-IR. This provides the material platform for abundant plasmonic device designs in addition to perfect metamaterial absorber. Overall, considering the multifaceted nature of MXene family and their highly electronic/optical tunability, MXenes have a great potential to be used in nonlinear photonics, optoelectronics and plasmonics.

CHAPTER 3. HIGHLY BROADBAND ABSORBER USING PLASMONIC TITANIUM CARBIDE MXENE ($TI_3C_2T_X$)

ABSTRACT

Control of light transmission and reflection through nanostructured materials has led to demonstration of metamaterial absorbers that have augmented the performance of energy harvesting applications of several optoelectronic and nanophotonic systems. Here, for the first time, a broadband plasmonic metamaterial absorber is fabricated using two-dimensional titanium carbide ($Ti_3C_2T_x$) MXene. Arrays of nano disks made of $Ti_3C_2T_x$ exhibit strong localized surface plasmon resonances at near-infrared frequencies. By exploiting the scattering enhancement at the resonances and the optical losses inherent to $Ti_3C_2T_x$ MXene, high efficiency absorption (~90%) for a wide wavelength window of incident illumination (~1.55 μm) has been achieved.

3.1 Introduction

Versatile capability of light manipulation using plasmonic resonators has led to development of nanoscale perfect lenses[164], sensors[165], absorbers[67], detectors[166], light sources[167,168], and other planar nano photonic devices. Metamaterial absorbers, in particular, have been shown to bring about some of a new generation of energy harvesting systems such as nanoscale heat sources[169], photo-thermal[170], solar photovoltaic[171], and thermoelectric devices[172], as well as photo-catalysis[173]. Also, utilizing some phenomenon such as localized heating through light absorption of metamaterials has led to demonstration of thermophoresis-assisted and other heat-assisted nanoscale particle manipulation and printing schemes that are now of wide interest for various applications[69].

Generally, well-known noble metals such as Au[174], and Ag[175] as well as other lossy metals such as Cu[176], and Ti[47] have been extensively used as plasmonic absorbers. More recently, absorbers with refractory plasmonic compounds (e.g., TiN[67,177]) have been also used in designing

devices requiring elevated temperature operation. Furthermore, due to their unique electronic and optical properties, 2D materials such as graphene, transition metal di-chalcogenides, phosphorene etc. have also been implemented in devices with tunable[178], perfect[179], and saturable absorption[104,117,180,181]. To design plasmonic absorbers, localized surface plasmon resonances in metallic nano-antenna structures are often employed to significantly increase the optical cross-section which leads to absorption amplification in the spectral range of interest[18,182]. In many of these examples, the operation bandwidth is largely determined by the full width at half maximum (FWHM) of the plasmonic resonances at play. Therefore, spectrally shifted resonances (from one or more resonating elements) can be harnessed to achieve a large absorption bandwidth.[59,183] However, the collective response of the device is affected by individual antenna geometry beside the interaction of resonances from the neighboring elements. These factors necessitate an absorber device that can combine high efficiency, robust broadband operation in an ultrathin, easy-to-fabricate and scalable design.

Recently, 2D transition metal carbides and nitrides called MXenes, have drawn a great interest due to their tunable properties and wide range of applications[119]. The chemical formula of MXene compositions is written as $M_nX_{n+1}T_x$, where 'M' denotes the transition metal (e.g., Ti, Ta, Nb, Zr, Hf, Cr, Mo etc.), 'X' is either C and/or N, and T represents surface functional groups[184,185]. In contrast to other 2D materials often exfoliated by mechanical exfoliation of their bulk counterparts, single to few layer flakes of MXene are isolated through chemical exfoliation of bulk ternary carbides and nitrides, known as 'MAX' phase, in fluorine-containing solutions[120]. More than 60 varieties of MXenes have been predicted and more than 20 have been experimentally synthesized, making them among the fastest growing and the most diverse 2D materials[78]. In particular, titanium carbide ($Ti_3C_2T_x$) MXene exhibits high electrical conductivity[78] and has been explored in a variety of applications such as transparent electrodes[121], metal ion batteries[122], supercapacitors[123–125], electromagnetic interference shielding[126], etc. Utilizing the optical properties of ($Ti_3C_2T_x$) MXene, other applications such as effective light to heat conversion[128], saturable absorption for mode-locked lasing[129], and as surface enhance Raman resonance (SERS) substrates[130,131] have also been demonstrated. However, investigations of ($Ti_3C_2T_x$) MXenes in the context of nanophotonics and plasmonics[18,19] have been limited in both theory[150] and experiment[130,148].

In this work, for the first time, plasmonic resonances in nanostructured $Ti_3C_2T_x$ MXene have been used to create a simple and easy-to-fabricate metasurface[186] device. Large absorption over a broad bandwidth (~1.55 μm), covering a significant visible to near-IR spectral window, was obtained by utilizing both the large optical absorption and the scattering enhancement of plasmonic resonances of nanostructured $Ti_3C_2T_x$ at longer wavelengths. Integrating MXenes with planar metamaterials is expected to have a significant impact on the large scale energy harvesting systems by improving conversion efficiency of light to heat, light to electricity, and heat to electricity etc.

3.2 Film preparation and characterization

$Ti_3C_2T_x$ is the first discovered and the most studied MXene; however, it was chosen as the primary focus for this work due to its high metallic conductivity[120,161], environmental and chemical stability[161], controllable surface hydrophilicity[187], dynamic control through easy intercalation[145], and scalable synthesis (~100 gram per batch in the lab). Due to the wet chemical synthesis in fluorine-containing media, the surface of 2D $Ti_3C_2T_x$ sheets are terminated with functional groups (T_x) such as -F -O, and –OH[188]. Although the surface chemistry can affect some properties such as the hydrophilicity, electrical conductivity and free carrier concentration[188,189], the core layer of Ti metal in $Ti_3C_2T_x$ is predominantly behind the high electrical conductivity of this MXene. Moreover, it has been shown that the surface of $Ti_3C_2T_x$ can be modified as per requirements of specific application[190,191]. In our experiments, the $Ti_3C_2T_x$ was prepared via minimally intensive layer delamination (MILD) method (Figure 3.1 (a)), which results in flakes of $Ti_3C_2T_x$ MXene with 1-10 μm in lateral dimension[161] and we recently described it in detail elsewhere[78]. With larger single- or few-layer flakes in the initial solution dispersion, spin-coated thin films become uniform over a larger area, which is critical for subsequent processing steps (for details, see Methods).

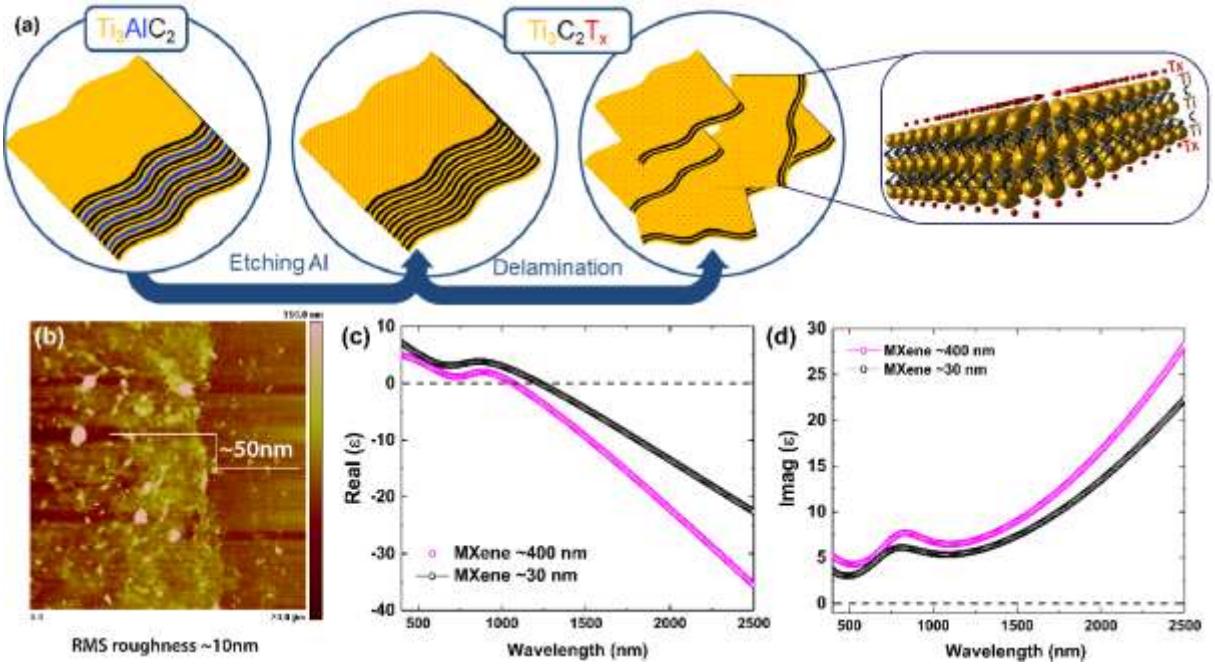

Figure 3.1 (a) Schematic of synthesis of MXene and the structure of a single layer of $Ti_3C_2T_X$, (b) AFM image of a spin coated MXene film with a scratch to measure the thickness (indicated inside), (c, d) experimentally measured real (c) and imaginary (d) parts of permittivity (ε) of $Ti_3C_2T_X$ films with thickness 30 nm and 400 nm.

The colloidal solution of single- to few-layer flakes of MXene can be used for vacuum assisted filtration[192], or spray coating[126] to create large-area freestanding micron-thick sheets of MXene, as well as produce nanometer-thin films by spin coating on a substrate of choice[193] (Figure 3.7S), rendering the process highly scalable and cost-effective. In this work, thin MXene films of varying thicknesses (~30-400 nm) were used. Bulk in-plane conductivity of ~6500±800 S/cm in N_2 atmosphere and ~2000 S/cm in open air, carrier density of ~ (3.1±0.7) $x10^{22}$ cm^{-3}, and Hall carrier mobility of ~0.9±0.1 $cm^2 V^{-1} s^{-1}$ have been reported previously for $Ti_3C_2T_x$ films of similar thickness[79]. Continuous films with thickness down to ~5 nm, exhibiting similar metallic characteristics have also been successfully demonstrated[79]. A high conductivity of ~4600±1100 S/cm (in air) and field effect mobility of ~2.6±0.7 $cm^2 V^{-1} s^{-1}$ have been reported for individual $Ti_3C_2T_x$ flakes[161]. The low carrier mobility in these films have been explained intuitively by inter-flake hopping-type conduction[79,194]. Thickness of the films were measured using a profilometer and/or atomic force microscope (AFM) after carefully making a scratch on the film (Figure 3.1 (b)).

First, spectral dependence of the real and imaginary parts of the dielectric permittivity (ε) was measured for the spin coated $Ti_3C_2T_x$ films of varying thickness, using a variable angle spectroscopic ellipsometry (VASE) set up (Figure 3.6S). One Drude term and two Lorentz type oscillators are used to fit the measured raw VASE data and extract the parameters of the dielectric functions (Table 3.1S). The Drude term describes the metal-like behavior whereas the two Lorentz oscillators account for the inter-band electron transitions. A dielectric to metallic crossover at ~1.07 μm corroborates the existence of surface plasmon polaritons (SPPs) at the MXene interface in the near- and mid- infrared (IR) frequencies. Figure 3.1 (c, d) compares the dielectric permittivity values measured from MXene films of thickness ~30 nm and, ~400 nm. A large imaginary part of the relative dielectric permittivity (*Im*(ε)) was observed for both films, increasing with the thickness (higher for thickness of about 400 nm). In addition, thicker films appear to be more metallic (lower cross-over wavelength for thickness of about 400 nm). Optical losses were attributed in parts to the intrinsic absorption due to inter-band transitions (at ~5.36 eV (0.23 μm) and ~1.54 eV (0.8 μm))[135] and to losses stemming from surface roughness and bulk disorder related scattering of carriers (Figure 3.1 (d)). Lorentz oscillators at similar frequencies obtained through ellipsometry measurement, summarized in Table 3.1S.

3.3 Theory and design discussion

Secondly, we evaluated the performance of $Ti_3C_2T_x$ nanostructures through numerical simulations by utilizing the optical properties data retrieved from ellipsometric characterization of the continuous MXene films. Full wave three-dimensional (3D) finite-element method (FEM) simulations were performed using commercially available multi-physics tool 'COMSOL' for large area array of disks/pillars of MXene on glass substrates with varying diameters and thicknesses. The measured frequency-dispersive dielectric permittivity values of the MXene film were input into the model. The optical parameters (transmission, *T*, and reflection, *R*) as a function of the wavelength were calculated under excitation of TM polarized light. An incident angle of 20^o was assumed for this study (for details on experimental set-up, see Supporting Information Section 1), unless specified otherwise. The calculated reflection spectra from arrays of disks/pillars with varying diameter (*d*) as 250 nm, 350 nm and 450 nm are shown in Figure 3.2 (a). Corresponding transmission and absorption spectra are shown in Figure 3.8S. A periodic spacing (*P*) of 600 nm and thickness (*t*) of 400 nm were used for these calculations. The plot clearly indicates signatures

of a resonance (peak in the resonance spectra) at ~1.26 µm and for *d* =450 nm. This is determined to be localized surface plasmon (LSP) resonance from the cross-section electric field maps shown in Figure 3.2 (c) and displacement current maps (shown in Figure 3.9S). As expected, optical losses cause the resonance to be broad and, with reduced resonator dimension, the resonance peak frequency blue shifts. But, with relatively less metallic real part of the relative dielectric permittivity *Re(ε)* along with the large enough *Im*(ε) at the blue-shifted wavelength, the quality factor of the resonance drops significantly (the peak almost disappears for disk *d* = 250 nm). Additionally, for smaller *d*, lower filling fraction (disk area/ unit cell area) allows increased transmission (*T*) through the structure. MXene resonators have dielectric like optical properties at higher energies, and when surrounded by a lower index medium (air), create a weak lattice mode in the periodic array (small peak in the reflection spectra at ~0.9 µm). For λ < 1 µm, the MXene disks support weak photonic resonance modes that also contributes in part to enhanced absorption in the visible spectral window (Figure 3.10S). Deeper into near-IR, beyond ~1.8 µm, MXene is more Drude type metallic which renders large reflection amplitude.

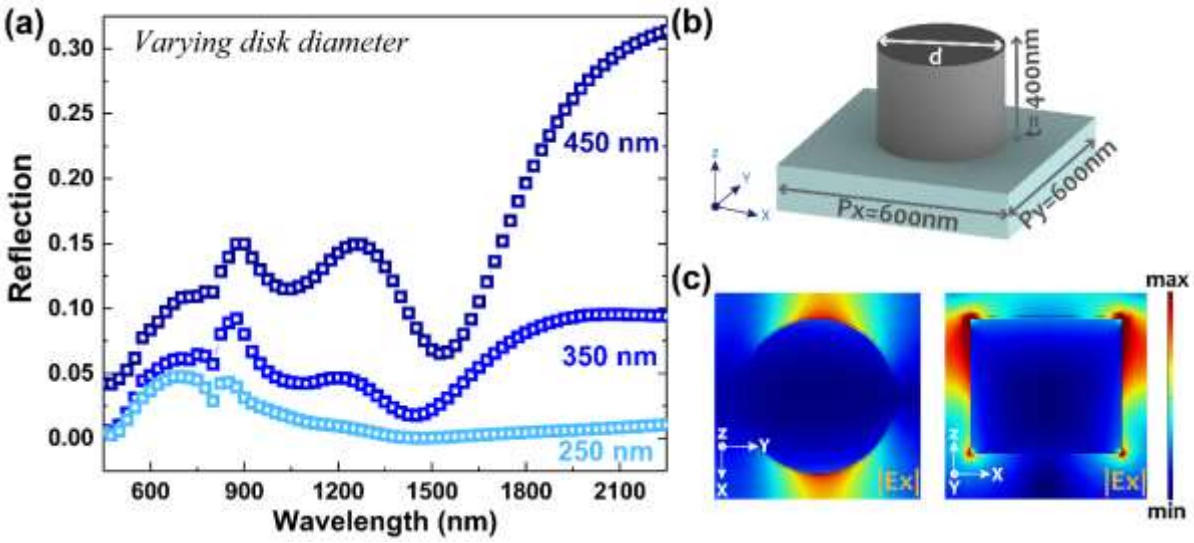

Figure 3.2 (a) FEM simulation generated reflection spectra for $Ti_3C_2T_X$ disk arrays on glass substrate with varying disk diameters (450 nm, 350 nm and 250 nm, respectively) for TE polarized incident light, (b) schematic of a typical unit cell with critical dimensions indicated and, (c) electric field intensity map at a horizontal (at z = t/2 from the top of the disk – left image) and vertical (y = d/2 from the edge of disk – right image) planar cross-section through the disk. Localized surface plasmon induced dipolar resonant mode at wavelength (λ) ~1.26 µm can be inferred.

Losses inherent to the bulk MXene and existence of LSP resonances in nanostructures led us to investigate the potential of nano-patterned MXene as an absorber metamaterial. In the

simulation, the absorption (*A=1-T-R*) is calculated as a function of the incident excitation wavelength (λ). Dimensions of different components were optimized to maximize the amplitude as well as the absorption bandwidth. For an array of $Ti_3C_2T_x$ disks with d = 450 nm, P = 600 nm and t = 400 nm sitting on a glass substrate, over 85% absorption efficiency was achieved across 0.4-1.4 μm bandwidth (blue curve in Figure 3.3 (a)) Simulations were also performed to calculate the absorption from an as-coated continuous film of the same thickness (red curve on Figure 3.3 (a)). Absorption in the visible and very near-IR originates largely from inter- and intra-band transitions of electrons[135,150]. At longer wavelengths, resonance aids increased scattering cross-section. Together, these two phenomena create high absorption efficiency over a large spectral window. However, the absorption in the patterned disk array shows significant improvement (~2.5 *times* at ~1.5 μm) when compared to the unpatterned film (Figure 3.3 (a)).

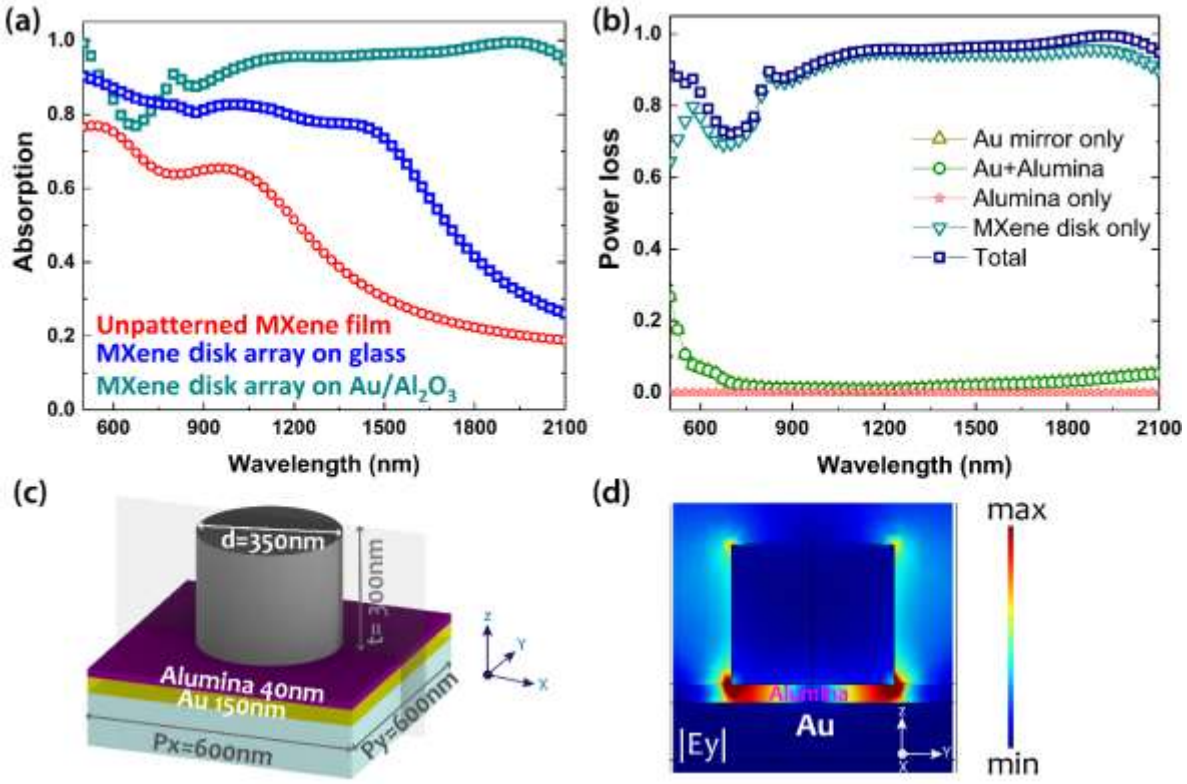

Figure 3.3 (a) Simulated absorption spectra comparison of unpatterned MXene film, MXene disk array on glass and MXene disk array on Au/alumina (incident light is TE polarized, angle of incidence is 20^{o}), (b) comparison of volume integrated power loss density (simulated) in the individual components e.g. MXene disk only, Au mirror only, Alumina only, Au+Alumina and total structure, (c) schematic of a unit cell with relevant dimensions and, (d) vertical cross-section (y = d/2 from edge of disk) electric field map at λ~ 1.85 µm

To further increase the performance of this broadband absorber design, we added a thin mirror (Au) and dielectric spacer layer (Al_2O_3) underneath the disk array. Schematic of a unit cell is shown in Figure 3.3 (c). This geometrical configuration supports gap surface plasmon (GSP) resonance[195]. This mode is formed when a resonator is placed close to metal surface but separated by a nanoscale gap (in a practical scenario, a dielectric spacer layer)[196]. The mode is the result of interaction of surface plasmons on the two adjacent dielectric-metal interfaces and efficient reflection from the ends of the finite dimension resonator on the top surface. The forward and backward propagating gap surface plasmons (GSP) interfere constructively and destructively to create standing wave resonances in a Fabry-Perot like cavity at certain frequencies. This causes a high electric field confinement in the gap region which can largely enhance the power efficiency of the device[197]. Figure 3.3 (d) shows the cross-section electric field map of this gap plasmon

resonance. The mode (at λ ~1.85 μm in this structure) displays a strong field confinement in the alumina (Al_2O_3) spacer layer. The Au layer at the bottom of the structure is optically thick and blocks all light transmission. Optical properties of Au and Alumina used in simulation were measured by VASE technique (summarized in Figure 3.12S). This mode attribute can be controlled by the optical properties and thickness of the spacer dielectric, as well as the properties of the top resonator. This extended parameter space was utilized for obtaining maximum absorption (>90%) over an even broader operating bandwidth. Through optimization in full wave 3D FEM simulations, design parameters were determined to be a 40 nm thick alumina spacer on top of a 150 nm thick Au film and the periodic MXene disk array to be of d = 350 nm, t = 300 nm, and P = 600 nm.

Absorption in this gap plasmon structure mainly originates from the MXene disk for almost the entire bandwidth of investigation. Absorption contributions for different structural components (MXene disk only, Au mirror only, Al_2O_3 spacer only, Au + Al_2O_3, and all together) were calculated separately by volumetric integration of power loss density ($P_{loss} = \frac{1}{2}\omega Im(\varepsilon)|E|^2$) and the comparison is shown in Figure 3.3 (b). Localized resonances, as seen in the electric field intensity maps, aid field concentration near the surfaces of the MXene resonators, which is the main source of losses in near-IR. Low quality factor of this hybrid resonance mode at ~1.85 μm is responsible for achieving near-perfect absorption over a broad region of the spectrum. The noble metal (Au) back mirror is highly metallic at longer wavelengths (large negative $Re(\varepsilon)$) and therefore functions as an almost perfect reflector having negligible contribution to total absorption. Between 600-900 nm MXene behave as a lossy dielectric. The small dip in the absorption spectra at ~ 680 nm stems from a hybrid resonant mode. This arises from a weak coupling between a photonic mode in the MXene disk and an SPP- like mode in the Au-Alumina interface (Figure 3.11S (b))[198].

3.4 Experimental implementation and characterization

Next, the MXene nano-disk arrays were fabricated following the two designs discussed above (Figure 3.4 (a, b)), and optical scattering parameters were measured using a VASE set up (see Methods for details of fabrication and measurement). Reflection (R) and Transmission (T) were measured for different incident angles and both orthogonal polarizations (TM and TE). Absorption

(A) is calculated as *A= 1-T-R*, as before and is shown in Figure 3.4 (c). Large absorption (≥ 80%) over 0.4 μm to 1.3 μm is observed for just the disk array on glass (blue curve in Figure 3.4 (c)). For the other design, with the disk array sitting on an Au/Al_2O_3 bilayer stack, similar large absorption (~85% - 90%) is obtained, but in addition, the bandwidth is stretched further to ~1.55 μm (green curve in Figure 3.4 (c)). Significant enhancement of absorption as compared to the unpatterned MXene film, throughout the entire bandwidth of operation was demonstrated in the experiments. A good qualitative agreement in comparative trend between the experimentally measured curves (~2 *times* improvement in absorption in the MXene disk array on Au/alumina over an un-patterned film of similar thickness (*t*) at λ ~ 1.6 μm) with the ones obtained through simulation is apparent.

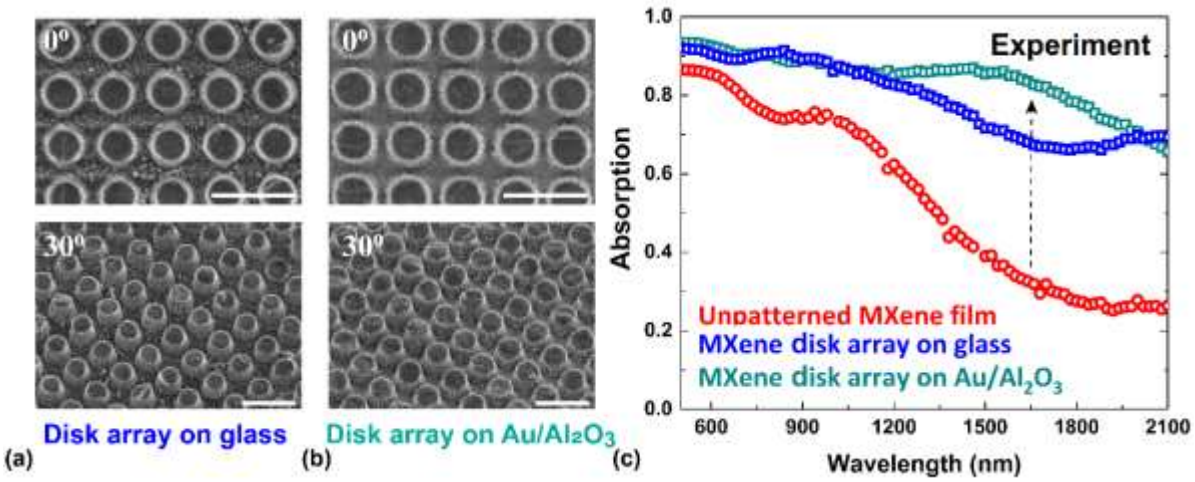

Figure 3.4 SEM images collected from 0° (top) and 30° inclined angle (bottom) from the fabricated (a) disk array on glass, (b) disk array on Au/alumina (scale bars indicate 1 μm in all images) and, (c) measured absorption spectra comparison for the two types of disk arrays and unpatterned MXene film (incident light is TE polarized, angle of incidence is 20°).

The measured absorption spectra for both TE and TM polarized excitation match almost perfectly for low incident angles (< ~40°) as shown in Figure 3.5 (a). An incident angle dependence of the absorption spectra was observed for both orthogonal polarizations. This was extracted in simulation and summarized in Figure 3.5 (b) and Figure 3.13S. Large absorption over the entire bandwidth of interest was maintained with incident angles ranging from 0° to 65° for TE polarized incident light (all angles were calculated from normal, i.e. 0° is equivalent to normal incidence). However, for TM polarized incidence, this angular bandwidth ranged from 0° to 45° (Figure 3.13S).

Deviation of the observed experimental data from the simulated ones stems from a few factors. It is well known that surface plasmon-polaritons and nature of LSP and GSP resonances have high sensitivity to the adjacent environment and geometry of the resonators[18]. This has propelled prolific use of plasmonic resonators in sensing[199,200]. Similarly, in the absorber design discussed here, the geometry as well as the surface chemistry of $Ti_3C_2T_x$ MXene, affect the LSP, GSP resonances and in turn the overall absorption spectrum.

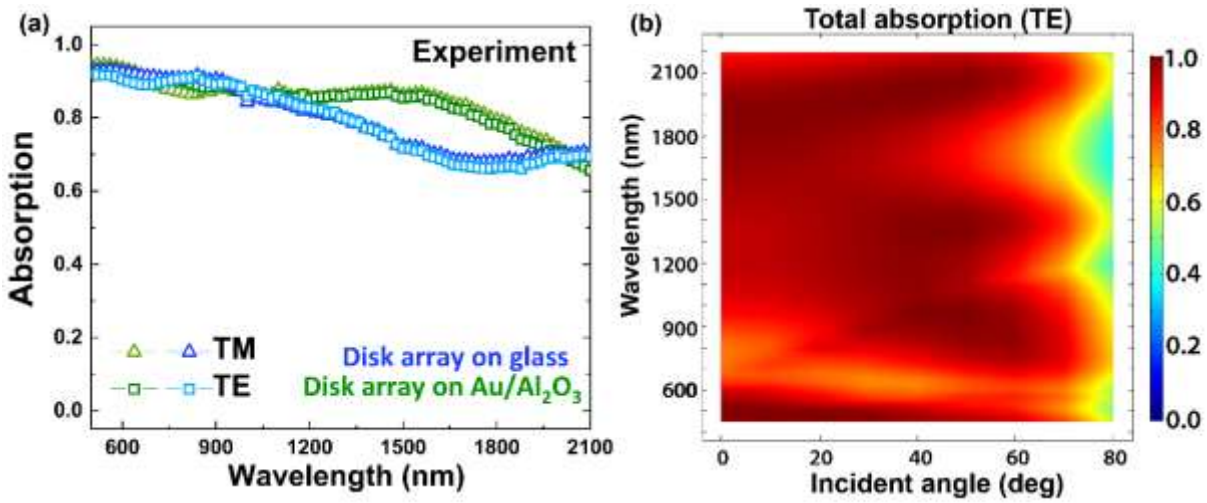

Figure 3.5 (a) Experimentally measured absorption spectra for two orthogonal polarizations (TE and TM) for both fabricated disk array designs (on glass and on Au/alumina back layer) at 20^o angle of incidence, (b) simulated angular bandwidth for the disk array on Au/alumina for TE polarized incidence. The map plots wavelength (λ) vs. incident excitation angle (measured from normal), and the amplitude of absorption is indicated by the color bar.

3.5 Conclusion

In this work, we used nanoscale structures of 2D $Ti_3C_2T_x$ MXene to demonstrate localized surface plasmon type resonances. The optical properties of thin films of overlapping flakes of $Ti_3C_2T_x$ are studied and used to design metasurfaces exhibiting broadband absorption. Both proposed MXene based designs are relatively simple to fabricate into sub-wavelength sized disk structures, in contrast to previous reports of plasmonic absorbers with complex geometries. Large operation bandwidth (maximum of ~1.55 μm) and high efficiency (80%-90%) are attained. The highly broadband absorber reported here for $Ti_3C_2T_x$, along with the ability to tune the surface properties of MXene, will open doors to investigating MXenes in important applications, such as harvesting energy from light, biomedical imaging, and sensing. With more than 20 MXenes already reported

and dozens more predicted, the processing and nanofabrication techniques developed for $Ti_3C_2T_X$ are of high relevance for other members of the MXenes family. This work serves as a first step toward successful integration of MXenes into the field of nanophotonics.

3.6 APPENDIX Methods

$Ti_3C_2T_x$ MXene thin film preparation:

Fused silica glass substrates (from PG&O) with dimensions 1.5 cm x 1.5 cm were cleaned with 10 mL of liquid bleach (Sr5900-1 GAL, Fisher Scientific) and diluted in 10 mL of deionized water (DI H_2O) using bath sonication (model 2510R-DTH, Bransonic) for 5 min. The substrates were further bath-sonicated in 20 mL DI H_2O (4 times for 2 min) and 20 mL ethanol (4 times for 2 min) before being purged with argon. Prior to spin coating, the glass substrates were further treated with ozone (O_3) plasma for 20 min followed by purging in N_2 to enhance their surface hydrophilicity and to improve the adhesion and the uniformity of the $Ti_3C_2T_x$ coated film.

Spin coating was done by drop casting 200 µL of $Ti_3C_2T_x$ MXene solution (30 mg/mL) on the substrate followed by spinning at 800, 1000, 2000, and 5000 rpm for 1, 1, 4 and 4 min, respectively. $Ti_3C_2T_x$ films coated on the glass substrates were dried during the spinning while MXene coated on Al_2O_3 substrates was dried in air for 15 min. Both substrates were further dried in vacuum oven at 150 ˚C for 15 h. Different thicknesses of coated films were achieved by variation of spinning conditions and the concentration of flakes in the initial solution. For the hybrid design, 10 nm Ti, 150 nm Au and 40 nm Al_2O_3 were deposited subsequently onto a clean glass substrate by electron beam evaporation. MXene was coated onto this sample using the same method as discussed above.

Simulation:

In commercially available multiphysics tool COMSOL, wave-optics module has been used to perform full wave finite element method simulations (frequency domain). Direct stationary "PARDISO" solver is chosen for the calculations. Periodic boundary condition and port excitation mode is used. Transmission, Reflection and absorption are calculated using S-parameters. Relevant geometry parameters are discussed in the main text. Experimentally measured spectral dependence of complex dielectric permittivity values for MXene, Au and Alumina (as presented in Figure 3.1 (c, d) and Figure 3.12 (a, b)) were input into the COMSOL model as well.

Fabrication:

Electron beam lithography followed by dry etching was used to fabricate the nanostructures. The samples with spin-coated MXene films were dipped into acetone and dried in nitrogen. First, a sacrificial layer of PMMA (950 A2) was coated followed by baking at 160^{o}C for 5 min. This layer helps protecting the MXene from subsequent lithography processing. After cooling to ambient temperature, a second layer of electron beam resist 'Flowable oxide', (FOX-16 by Dow Corning Chemicals) was coated and cured at 120^{o}C for 3 min. Thickness of this resist layer was ~600 nm. After electron beam exposure, the resist was developed using tetra-methyl ammonium hydroxide (TMAH) (25% in H_2O) solution for 1 min followed by 30 s rinse in DI water. Since the MXene surface is hydrophilic and both water and TMAH are intercalants for MXene, it is crucial to protect the film structure with the PMMA sacrificial layer. At this stage, the intended pattern was transferred onto the resist layer.

In the first step of dry etching, the sacrificial PMMA layer was etched using O_2 plasma. Following that, an inductively coupled plasma of halogenated (BCl_3, Cl_2) and Argon (Ar) gas mixtures was used to produce the MXene pillars. To maintain a high degree of anisotropy in the structure, a relatively large source power, low pressure and a small bias power were used. Etching time varied depending on the film thickness. SEM images of the final structure tilted at 30^{o} inclination are shown in Figure 3.4 (a, b).

Optical measurements:

Transmission (*T*) and Reflection (*R*) were measured for each sample using a VASE setup for two orthogonal polarizations of the incident beam (Supporting information Section 1). Incident angle was varied from 20^{o} to 80^{o} at steps of 10^{o}. Absorption spectra were then calculated using $A=1-T-R$.

3.7 APPENDIX Supplementary Information

Section1: Optical measurements:

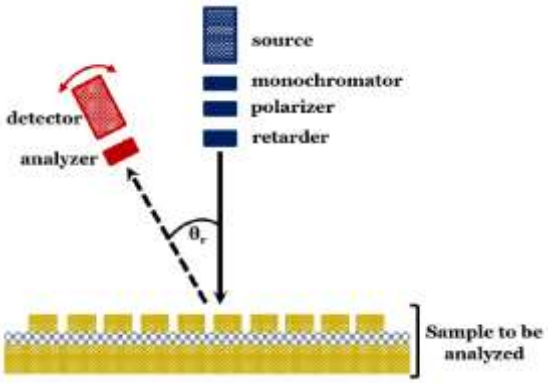

Figure 3.6S Schematic of a variable angle spectroscopic ellipsometer setup used for measurement of optical properties and scattering parameters (T, R, A).

Optical properties (permittivity values) as well as the measurement of the scattering parameters (*T, R*) was done using the variable angle spectroscopic ellipsometry setup. Schematic of the setup is shown in the figure. The detector arm can rotate to measure spectrum at variable angles. The smallest attainable angle between the source and the detector arm is ~18^{o}. For extracting optical permittivity of the MXene films, a Drude- Lorentz oscillator model (shown in the equation below) was used. The 2nd term on the right-hand side represents the Drude part and 3rd and 4th part comes from the Lorentz oscillators representing in this case inter-band electronic transitions in the Ti_3C_2Tx.

$$\varepsilon(\omega) = \varepsilon_{\infty} - \frac{\omega_p^2}{\omega(\omega + i\Gamma_p)} + \frac{f_1}{\omega_1^2 - \omega^2 - i\omega\Gamma_1} + \frac{f_2}{\omega_2^2 - \omega^2 - i\omega\Gamma_2} \qquad \text{Equation 3.1S}$$

For a 400 nm thick MXene film, extracted parameters of the model are summarized in the following table.

Table 3.1S Optical properties model parameters as derived from ellipsometry measurements of a ~400 nm thick $Ti_3C_2T_X$ film.

	Drude		***Lorentz 1***			***Lorentz 2***		
ε_∞	ω_p^2 ***(eV)***	Γ_p***(eV)***	f_1	ω_1 ***(eV)***	Γ_1***(eV)***	f_2	ω_2 ***(eV)***	Γ_2***(eV)***
0.901	15.21	0.298	5.21	1.549	0.74	190.97	5.362	4.79

Section 2: Scalable synthesis:

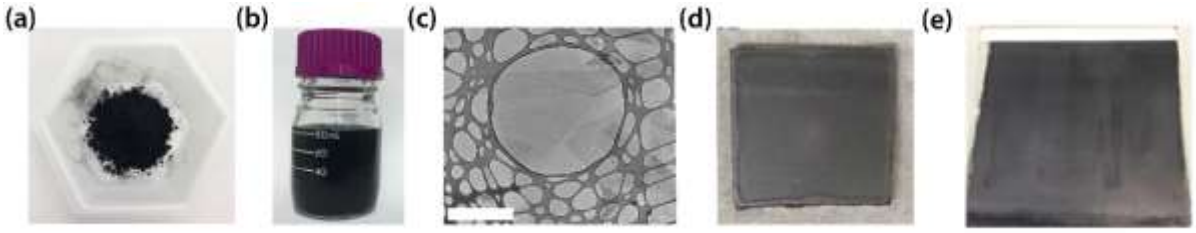

Figure 3.7S $Ti_3C_2T_X$ (a) in powdered form, (b) in colloidal aqueous solution used for spin-coating, (c) in a monolayer form (TEM image), the scale bar denotes 2 µm, (c) spin-coated on a glass substrate (of dimension ~ 15mm x 15mm) to create a ~200 nm film and, (d) coated on a large area (of dimension ~ 15 cm X 15 cm) PET (polyethylene terephthalate) transparency sheet.

Section 3: Transmission and absorption variation with disk array diameter:

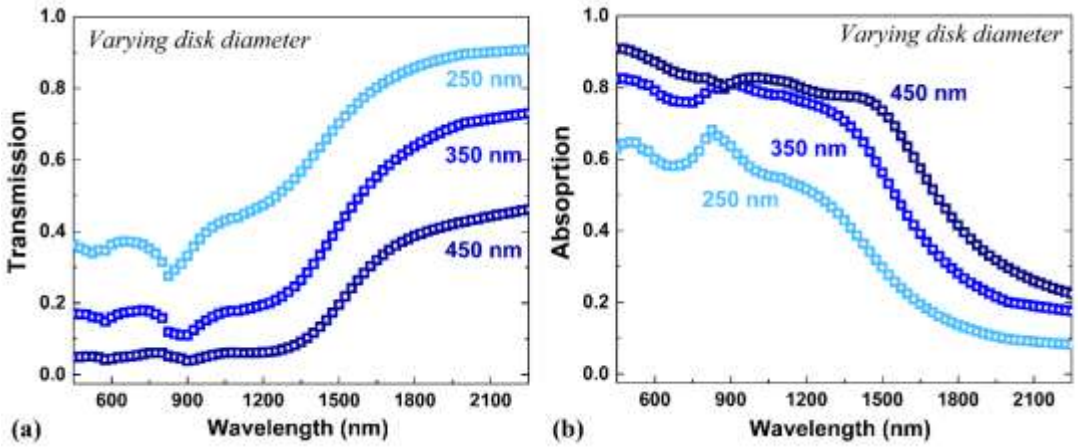

Figure 3.8S.FEM simulation generated (a) transmission and (b) absorption spectra for $Ti_3C_2T_X$ disk arrays on glass substrate with varying disk diameters (450 nm, 350 nm and 250 nm, respectively) for TE polarized incident light.

Section 4: Electric Field and Displacement current map:

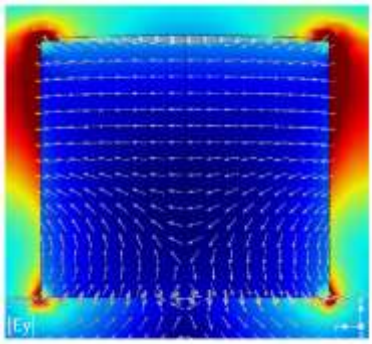

Figure 3.9S Electric displacement field map ($|E_y|$) within a MXene disk (d= 450 nm, t= 400 nm, P= 600 nm) array at resonance peak at $\lambda = 1.26$ µm, showing dipolar resonance caused by localized surface plasmon oscillations.

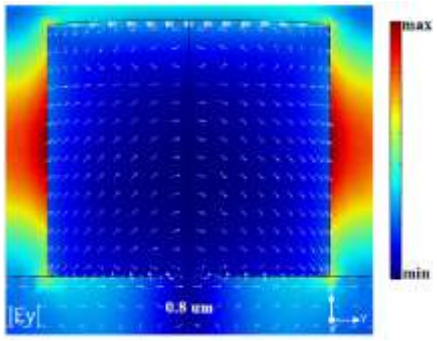

Figure 3.10S Electric displacement field map ($|E_y|$) within a MXene disk (d= 450 nm, t= 400 nm, P= 600 nm) array at $\lambda = 0.8$ µm, showing signature of weak photonic mode. For $\lambda < 1$ µm, the MXene behaves as a high permittivity, lossy dielectric and supports photonic dipole-type resonance modes that contributes in part to absorption in the MXene disk array in the lower end of the spectrum.

Section 5: Hybrid resonance mode:

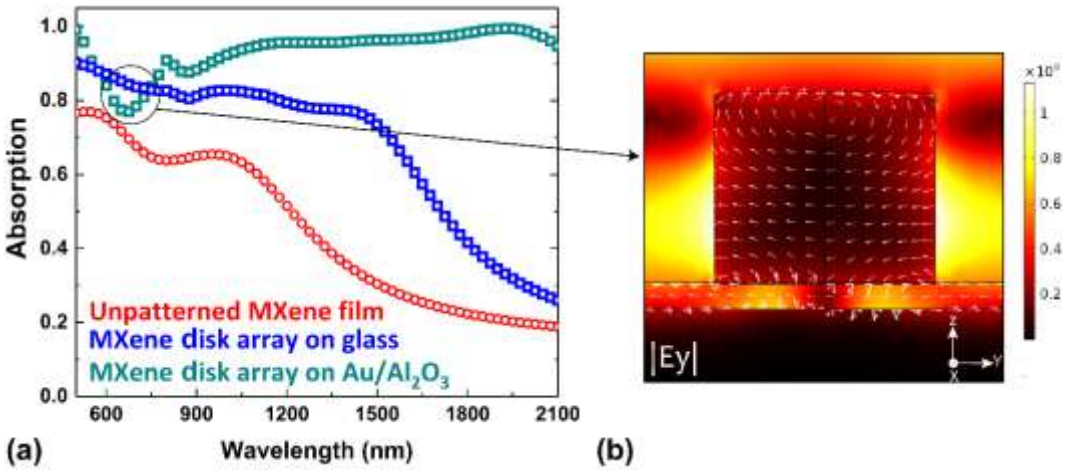

Figure 3.11S (a) Simulated absorption spectra comparison of unpatterned MXene film, MXene disk array on glass and MXene disk array on Au/alumina, (b) vertical cross-section (y = d/2 from edge of disk) electric field map at the indicated absorption dip at $\lambda \sim 0.675$ μm. The arrows indicate the three component electric displacement current vectors. A photonic dipolar type resonance and an SPP-type component at the Au-Al_2O_3 interface is observed. Hybridization leads to weak field confinement in the lower index dielectric Al_2O_3.

Section 6: Au, Alumina optical properties:

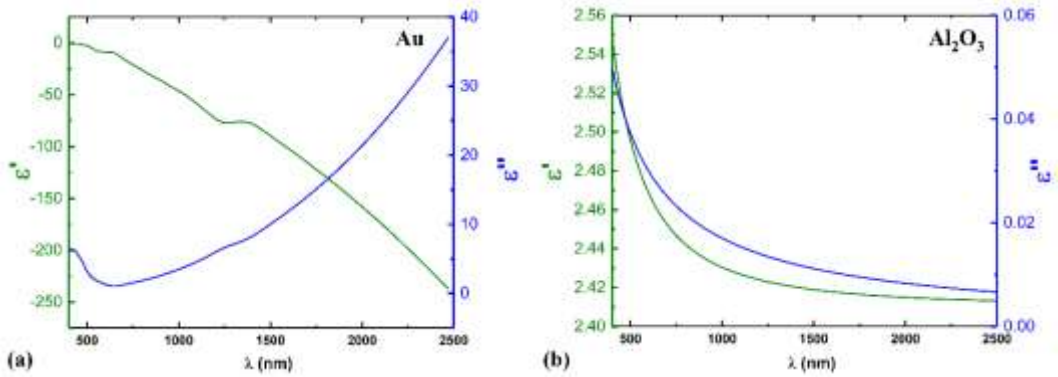

Figure 3.12S Experimentally measured real (left axes- green curve) and imaginary (right axes-blue curve) parts of complex permittivity (ε) of e-beam deposited Au (a) and Alumina (b) films with thicknesses of 150 nm and 400 nm respectively.

Section 7: Angular bandwidth:

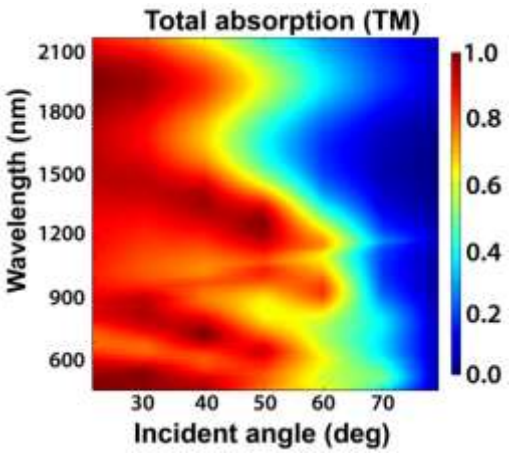

Figure 3.13S Simulated angular bandwidth for the disk array on Au/alumina for TM polarized incidence. The map plots wavelength vs. incident excitation angle (deg), and the amplitude of absorption is indicated by the color bar. All angles were calculated from normal, i.e. 0^{o} is equivalent to normal incidence.

CHAPTER 4. PHOTONIC SPIN HALL EFFECT IN ROBUST PHASE GRADIENT METASURFACES UTLIZING TRANSITION METAL NITRIDES

Contents of this chapter have been reprinted with permission from Chaudhuri, K.; Shaltout, A.; Shah, D.; Guler, U.; Dutta, A.; Shalaev, V. M.; Boltasseva, A. Photonic Spin Hall Effect in Robust Phase Gradient Metasurfaces Utilizing Transition Metal Nitrides. ACS Photonics 2019, 6 (1), 99–106.

ABSTRACT

Robust and high-temperature stable (refractory) transition metal nitrides are an emerging class of nanophotonic materials aimed at durable, bio- and CMOS-compatible plasmonic and metasurface applications. In this work, we experimentally demonstrate titanium nitride and zirconium nitride-based phase manipulating optical metasurfaces that exhibit a photonic spin Hall Effect. In the developed all-nitride system, metal nitrides are combined with dielectric nitrides such as aluminum nitride and silicon nitride to design a highly anisotropic, multilayer resonator geometry that supports gap plasmons and enables high power efficiency (~40%) and broad bandwidth of operation in the near-infrared wavelength region. A one-dimensional phase gradient created by geometric rotations of the resonators lead to simultaneous, spatial separation of right and left circular polarization as well as different frequency components of the incident light. This work shows that transition metal nitrides can be successfully integrated into efficient metasurface building blocks for planar, rugged optical devices.

4.1 Introduction

Metasurfaces embody a vast range of planar optical devices that achieve advanced control of light propagation, amplitude and phase by employing carefully designed metallic and/or dielectric optical scatterers at the interface[201,202]. In the past decade, numerous demonstrations have employed planar metasurface architecture to realize a wide variety of optical elements[203], ultra-compact flat lenses[35,204,205], planar holograms[41,206,207], wave-plates[37,38,208,209], spectrometers[210–213], and polarization rotators[30,44,214,215]. Among them, plasmonic metasurfaces, provide a unique capability enabled by metallic resonators, as they confine electromagnetic energy beyond the diffraction limit and enhance light-matter interactions, leading to significant scale-down of the

device footprint[216]. Plasmonic metasurfaces have been proven beneficial when it comes to augmenting bio-, molecular or chemical sensing[217–219], detection[55], energy harvesting[61,132,220], and even information encoding systems[221–223]. However, all metallic components suffer from finite optical losses that may negatively impact the device efficiency in many cases[46,224]. On the other hand, low loss dielectric materials may improve the metasurface device efficiency but often at the cost of relatively intensive fabrication, high aspect-ratio requirement, and more bulky resonator structures[225,226]. Recently, a multilayered, metal-insulator-metal stacked resonator geometry has emerged as a complementary approach that combines high efficiency and compactness[29,227]. A periodic array of metal nanoantennas placed on a metal back plane, separated by a thin dielectric layer supports gap surface plasmon (GSP) resonances, and enables improved amplitude and phase control in metasurfaces[195,197].

Along with the optimally efficient geometry, selection of constituent materials is yet another crucial part of metasurface design. In case of plasmonics, the two most prolifically used metallic components for optical metasurfaces are gold (Au) and silver (Ag). These noble metals show excellent plasmonic behavior in the visible to near-infrared (NIR) spectral range as well as strong chemical inertness (for Au)[70]. Most plasmonic metasurfaces have therefore been built utilizing these metals. However, with the expanding reach of metasurface functionalities, limitations of the existing materials become apparent. When considered for practical devices, noble metals pose significant challenges[228–230]. Owing to their relatively low melting point when nanostructured and high malleability, noble metals' applicability is limited in practical devices requiring high temperature stability, robustness to high-intensity lasers, mechanical durability, stable growth into ultra-thin films, and CMOS process compatibility for on-chip applications. In contrast, transition metal nitrides (TMNs) have been gaining attention as a robust and CMOS-compatible plasmonic platform for harsh environment applications[71,231,232].

Metallic TMNs such as titanium nitride (TiN), zirconium nitride (ZrN), hafnium nitride (HfN), niobium nitride (NbN), and tantalum nitride (TaN) have been used in variety of electronic applications since early eighties[233,234]. Generally, these conductive ceramics display high mechanical durability and more importantly, strong refractory nature that is very high bulk melting points (> 3000^{o}C). TiN and ZrN are commonly used as hard, protective coatings for medical equipments and mechanical parts. In appearance they closely resemble Au and are often used as their cheaper alternatives in large scale manufacturing as well. In addition, most of the constituent

transition metals (Ti, Ta, Hf) as well as some nitrides (TiN, TaN) are already-existing parts of the CMOS processing[235,236]. Their mechanical properties, similar optical properties to noble metals, and CMOS compatibility have led the interest of the plasmonics research community to metal nitrides. Following the first reports of the useful plasmonic properties of titanium nitride (TiN) and , zirconium nitride (ZrN)[72,228,234,237], their growth techniques, material and optical properties have been rigorously investigated[74,238–241]. The plasma frequencies of both TiN and ZrN are in the visible range, but they typically exhibit larger optical losses as compared to commonly used noble metals. Strong optical nonlinearity[242–244], temperature dependent complex dielectric permittivity[245,246], and elevated damage threshold of the nitrides[177,244,247] allow for stable device operation in various harsh environment conditions. In addition, the binary nature of the nitrides provides room to tailor the optical properties via varying the stoichiometry. The optical response of the TMNs depends on many factors including the lattice structure, crystal defects, surface roughness, grain sizes, stoichiometry, and so on. As a result of differing growth parameters during thin film deposition in literature, the optical properties of the metal nitrides vary within a large spectrum[233]. High quality thin films are typically obtained on specific substrate materials and at elevated deposition temperatures that present additional constraints to the achievable device design and pose challenges in their integration into planar optical devices[238,248,249].

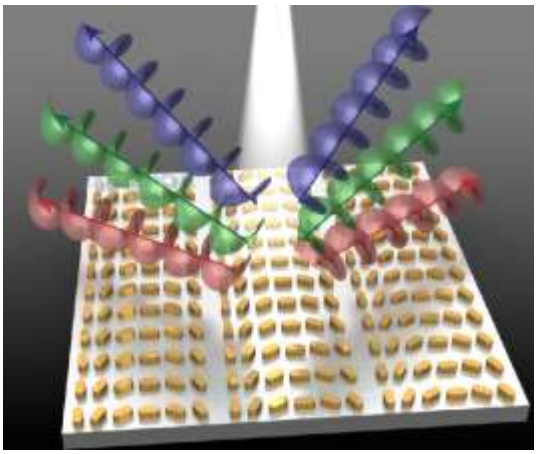

Figure 4.1 Schematic of the metasurface exhibiting photonic spin Hall Effect (SHE) by separating the two circular polarizations (or photonic spins) in opposite angular directions.

The growing knowledge base of plasmonic metal nitrides has naturally led to the development of practical metamaterial and metasurface designs in the past years. Broadband

perfect absorbers[67,177], local heat sources[48], and arbitrary lattice optics[250] using TiN planar structures are particularly noteworthy applications that have utilized the lossy nature of nitrides as well as their plasmonic property. Here, for the first time, we introduce the plasmonic metal nitrides to the realm of plasmonic phase-gradient metasurfaces employing GSP resonances in multilayered, metallic nanoantennas (NA) to create a desired spatial phase profile and manipulate the propagating wavefront. We have experimentally illustrated photonic spin Hall Effect (SHE) in the NIR, by reflecting the two spin states (right circular and left circular polarizations, RCP and LCP) in the opposite directions with mirror-symmetric angular dispersion of frequency components as shown in the schematic of Figure 4.1, realizing a circular dichroism spectrometer. Circular dichroism (CD) spectrometers are used extensively in biological sensing and pharmaceutical application spaces to detect the chirality of molecules that have different optical responses to circularly polarized light components[251,252]. Typically, CD spectrometers operate by sequentially switching between the LCP and RCP at the input[253]. A metasurface based approach achieves this complex operation by simutaneously generating two polarization (spin) states with high efficiency in a planar, ultra-thin, light weight device and can therefore eliminate the need for typical bulky and expensive spectrometers, and polarization switchable sources. An optical metasurface device with this functionality was previously introduced by *Shaltout et. al.* using subwavelength Au nanoantenna elements[212]. Based on a similar approach, a geometric phase gradient metasurface displaying photonic SHE is designed and implemented for both TiN and ZrN based nanoantenna elements. The nitride based metasurface spectrometer can further reduce the cost, increase durability of the device and be integrated in *in-situ* bio-compatible sensing tools as well. This work emphasizes the ability to integrate the refractory plasmonic metal nitrides into practically realizable, planar optical devices.

4.2 Material growth and characterization

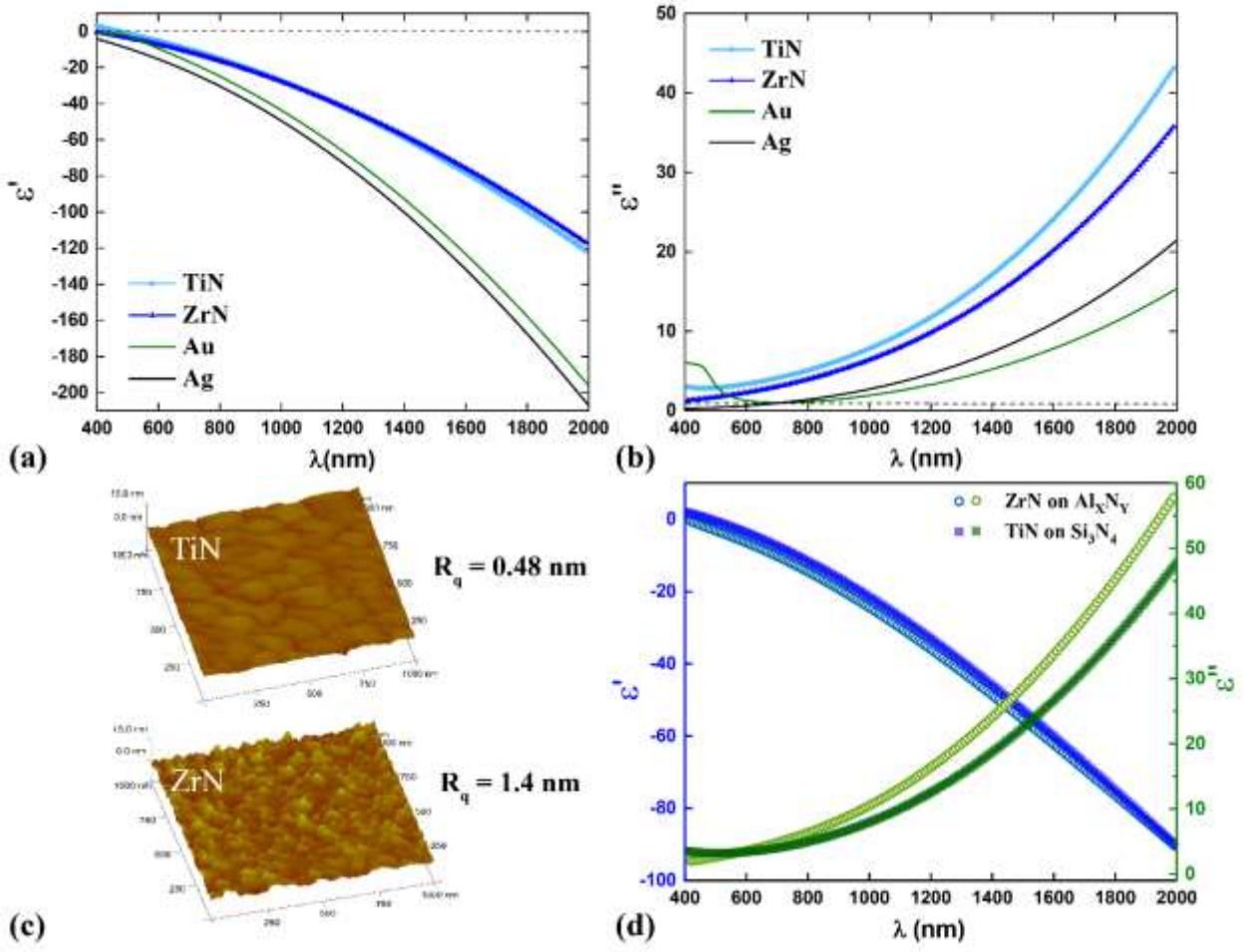

Figure 4.2 Comparison of experimentally measured real (ε') (a) and imaginary (ε") (b) parts of the complex dielectric function (ε) of TiN, ZrN, Au and Ag films of thickness ~200 nm (optically thick). TiN, ZrN films are deposited on crystalline MgO substrate and Au, Ag films are deposited on fused silica/glass substrate. (c) Surface roughness of corresponding TiN and ZrN films measured using atomic force microscopy (AFM) technique. Measured root mean sqaure (rms) values of surface roughness (R_q) are indicated. (d) Experimentally measured real (ε') (left axis-blue) and imaginary (ε") (right axis-green) parts of complex ε of polycrystalline TiN (~70 nm) and ZrN (~ 80 nm) grown on amorphous dielectrics Al_xN_y and Si_3N_4 respectively.

We measured the spectral profile of the complex dielectric function (ε) of thin films of TiN and ZrN, and comparing them to well-known noble metals, Au and Ag. TiN and ZrN are deposited using DC reactive magnetron sputtering, whereas the Au and Ag films are deposited using electron beam evaporation. A variable angle spectroscopic ellipsometry (VASE) set up (Figure 4.6S) is used to measure the optical response of the films, which is then fitted to an analytical model

(containing Drude and Lorentz type oscillators) to extract the complex permittivity, ε (Equation 4.6S,

Table 4.1S). A dielectric to metallic crossover for the real part of the permittivity ε', at ~500 nm (for TiN) and ~400 nm (for ZrN) indicates plasmonic behavior in the part of the visible range and NIR. In the spectral range of 0.5 – 2 μm, both TiN and ZrN behave as metals (large negative real part of permittivity, ε', Figure 4.2 (a)) similar to Au and Ag but at the same time exhibit a relatively higher magnitude of the imaginary part of permittivity, ε'', indicating larger optical losses in these films (Figure 4.2 (b)). The losses stem from the interband electronic transitions, represented by the Lorentz oscillators (Equation 4.6,

Table 4.1S) as well as electron-electron, electron-phonon, surface defects and grain boundary scattering processes experienced by the large number of free electrons in the lattice. Surface roughness of the films are measured using an atomic force microscopy (AFM) technique. The AFM scanned images collected from the nitride films are presented in Figure 4.2 (c). The plasmonic behavior of transition metal nitrides are critically dependent on their fine crystal structure which is largely affected by the growth conditions as well as the nature of the underlying substrate. The epitaxial growth of TiN on a lattice matched, single crystalline MgO substrate results in a much lower surface roughness and larger grain boundaries for TiN (0.48 nm (rms)) as compared to polycrystalline ZrN (1.4 nm (rms)) on MgO. In the case of the multilayered, GSP type resonator structure used in the metasurface design, the optical properties of the top metal layer grown on a thin dielectric are also critical. Therefore, we look at the experimentally measured complex permittivity dispersions of TiN grown on silicon nitride (Si_3N_4) and ZrN grown on aluminum nitride (Al_xN_y) (Figure 4.2 (d)). Nitride based dielectrics are chosen over more commonly used oxides (such as Al_2O_3 or SiO_2) to avoid oxygen contamination into the metal nitride. Silicon nitride and alumnium nitride are high refractive index dielectrics that confines the gap-plasmon resonating mode and are deposited using chemical vapor deposition (CVD) and DC sputtering, respectively. The amorphous nature of the dielectrics leads to polycrystalline structures of the top TiN and ZrN layers resulting in reduced metallicity and increased optical losses (Figure 4.2 (d)). Measured ε' are compared for Al_xN_y and Si_3N_4 in Figure 4.7S. These measured optical properties of all constituent layers of the resonator are input into the multiphysics simulation (for details, see supporting information, section 1) to achieve an optimized geometry.

4.3 Design, simulation and, demonstration

A photonic SHE is generated from the interaction of photon spin or the polarization state of light and asymmetric nano-structured antennas[213,254,255]. Unique arrangement of the anisotropic resonating elements creates different phase gradients seen by the two circular polarized (RCP and LCP) components of the incident light. To achieve high efficiency of operation, a reflection mode unit cell supporting gap-plasmon type resonance was chosen. The unit cell consists of a rectangular brick shaped plasmonic NA made of TiN or ZrN placed on a bilayer metal-dielectric stack Figure 4.3 (a-c)). This geometrical configuration supports a GSP resonance mode which achieves strong confinement of the electromagnetic energy to the narrow dielectric (spacer/gap) region[196]. The forward and backward propagating surface plasmons (SP) at the two adjacent dielectric-metal interfaces interfere constructively and destructively to create standing wave resonances in a Fabry-Perot like cavity at certain frequencies which causes the high electric field confinement in the gap region. This enhances the quality factor of the resonance that in turn improves the power efficiency of the metasurface device as compared to devices with a single layer of metal NA unit cells. Strong coupling of the incident light into the GSP resonance mode, also allows for large phase accumulation[197,227]. With the optimum aspect ratio (length/width) of the rectangular NA, a π-phase delay between the reflection coefficient components along the major and minor axes can be achieved.

To arrive at an optimal geometry, first a single unit cell (meta-unit) response is theoretically analyzed. The polarization and phase state of the reflected light beam is represented by Jones calculus. The Jones matrix for an anisotropic NA element can be written as[256],

$$\widehat{M} = \widehat{R}(-\alpha)\begin{pmatrix} r_o & 0 \\ 0 & r_e \end{pmatrix}\widehat{R}(\alpha) \qquad \text{Equation 4.1}$$

where r_o and r_e are reflection coefficients for incident light polarized along the two principal axes of the antenna. $\widehat{R}(\alpha)$ denotes the rotation matrix and α is the rotation angle of resonating element (indicated in Figure 4.3 (b)),

$$\widehat{R}(\alpha) = \begin{pmatrix} cos\,\alpha & sin\,\alpha \\ -sin\,\alpha & cos\,\alpha \end{pmatrix} \qquad \text{Equation 4.2}$$

$\widehat{M} = \widehat{R}(-\alpha)\begin{pmatrix} r_o & 0 \\ 0 & r_e \end{pmatrix}\widehat{R}(\alpha)$ Equation 4.1, can be rewrittern in circular basis as[256,257],

$$\widehat{M}_{circular} = \begin{pmatrix} \frac{1}{2}(r_o - r_e)e^{-i2\alpha} & \frac{1}{2}(r_o + r_e) \\ \frac{1}{2}(r_o + r_e) & \frac{1}{2}(r_o - r_e)e^{i2\alpha} \end{pmatrix} \quad \text{Equation 4.3}$$

For a right- or left- handed circular polarized incident light ($E_i^{R/L}$), the reflected light from the anisotropic meta unit, $E_r^{R/L}$ is expressed as

$$E_r^{R/L} = \widehat{M}.E_i^{R/L} \quad \text{Equation 4.4}$$

$$E_r^{R/L} = \frac{1}{2}(r_o + r_e)\, E_i^{L/R} + \frac{1}{2}(r_o - r_e)e^{im2\alpha}\, E_i^{R/L} \quad \text{Equation 4.5}$$

The first term on the right-hand side (RHS) of $E_r^{R/L} = \frac{1}{2}(r_o + r_e)\, E_i^{L/R} + \frac{1}{2}(r_o - r_e)e^{im2\alpha}\, E_i^{R/L}$

Equation 4.5 represents the circularly polarized reflected light component that has the opposite spin state as the incident one and the second term on the RHS is the part with the same photon spin state. This second component is the *co-polarized* component of reflected light associated with an additional geometric Panchratnam-Berry phase[258] of magnitude $m2\alpha$, where $m = \begin{cases} -1, & for\ RCP \\ +1, & for\ LCP \end{cases}$ incident light. This phase gradient term can attain any value within the entire 2π phase space by geometric rotation of the meta-units. The first term on the RHS represents the *cross-polarized* reflected light component that has no phase dependence.

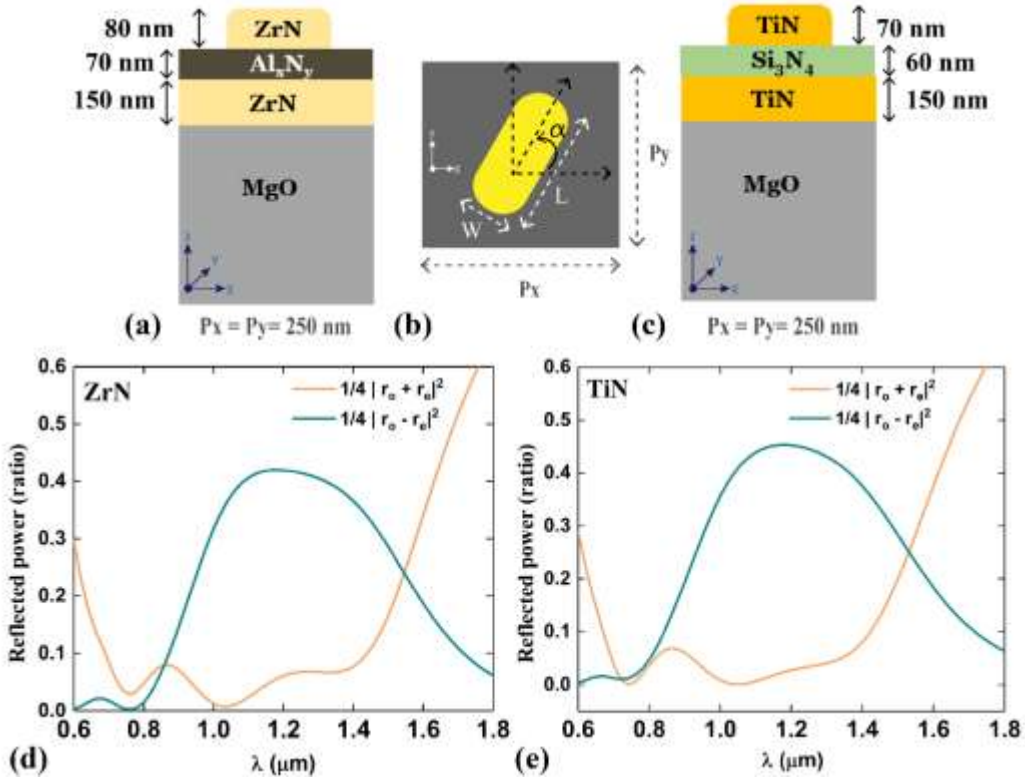

Figure 4.3 (a) Cross-section view of ZrN-AlxNy-ZrN based unit cell (optimized thickness for each layer is indicated). (b) Top-view schematic of a single NA element rotated at an angle of α. Edges are rounded to make the design realistic to fabricated structures. (c) Cross-section of TiN-Si3N4-TiN based unit cell (optimized thickness for each layer is indicated). Simulation results for both ZrN (d) and TiN (e) based meta-unit array showing maximum power output to the co-polarized component (indicated $1/4\,|(r_o - r_e)|^2$) while minimized power reflected to the normal cross-polarized mode (indicated $1/4\,|(r_o + r_e)|^2$).

All geometric dimensions of the meta-units are varied to obtain maximum power reflected into the *co-polarized* mode while simultaneously minimizing the efficiency of the *cross-polarized* mode. This is attained at frequencies where r_o and r_e are out of phase with each other. Design optimization was performed through full-wave 3D finite element method (FEM) simulation using commercially available multi-physics solver, COMSOL. The optimized dimensions of each meta-unit are indicated in Figure 4.3 (a, c). In one device, the 80 nm thick ZrN NA sits on a stack of 70 nm thick aluminum nitride (Al_xN_y) spacer on a 150 nm thick ZrN (mirror) film. In the other one, the bilayer stack consists of a 60 nm thick silicon nitride (Si_3N_4) spacer on 150 nm thick TiN mirror and the the top TiN NA is 70 nm thick. The top rectangular brick NA is 95 nm wide (W) and, 205 nm long (L) in both cases. Figure 4.3 (d, e) plots the simulated power efficiency to both *co-* and

cross-polarized components that are $1/4\,|(r_o - r_e)|^2$ and $1/4\,|(r_o + r_e)|^2$ respectively, for the two designs. A high (>40%) reflection efficiency is achieved in both cases which is comparable to the previously demonstrated Au based counterpart[212]. The larger optical losses of the TMNs are tackled through optimization of the nanoantenna design to arrive at this comparable efficiency and a much broader bandwidth (the full width at half maximum (FWHM) of *co-polarized* component) of operation. The ZrN and TiN based designs should therefore, exhibit a photonic SHE in the spectral window of ~0.9-1.6 μm (Figure 4.3 (d, e)).

With this optimized structure, a supercell was created from a linear arrangement of 6 meta-units. In the supercell, each meta-unit is rotated at an angle of |30°| relative to the neighboring one as shown in the schematic in Figure 4.4 (a, b). This provides a uniform phase gradient along the X-axis. This one dimensional phase gradient seen by the two circular polarized components of incident wave are opposite in sign, causing them to reflect in opposite directions. A periodic array of the supercell over a large area makes the final metasurface device. The device performance is estimated by simulating the periodic supercell array. The spatial electric field maps shown in Figure 4.4 (c, d) shows that the incident LCP and RCP components are anomalously reflected in two opposite angular directions. This angle of reflection measured in simulation is further verified by the well-known generalized Snell's law[17] as $\theta = \sin^{-1} m.\frac{\lambda}{P}$, where P is the supercell periodicity (1.5 μm in this case) and λ is the reflected wavelength and m is as before. Each frequency component is reflected at a different anomalous angle creating a spatially dispersed spectra of the co-polarized light. The supercell period was chosen to be 1.5 μm to keep the angular dispersion of the operating bandwidth (0.9-1.6 μm) at an angle greater than 38°, a limitation posed by the experimental measurement set up (see supporting information, section 2).

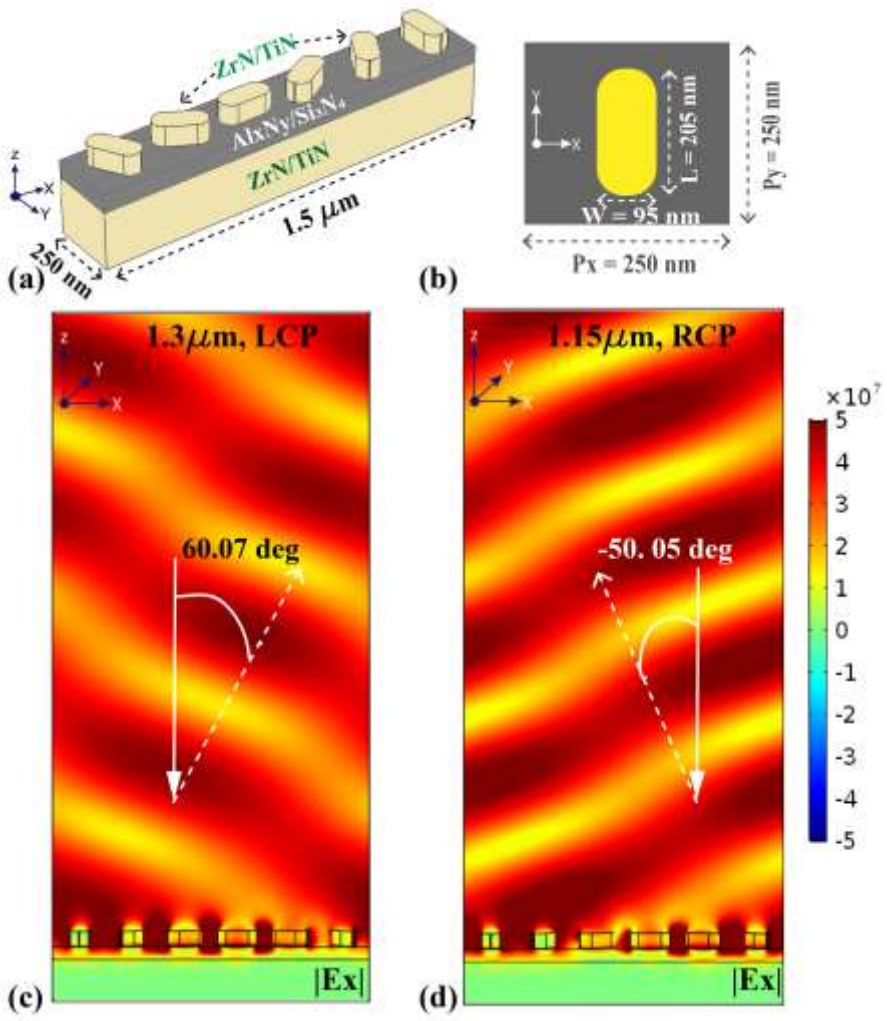

Figure 4.4 Schematic of (a) the complete supercell and (b) a single brick-shaped NA as in simulation. (c-d) Electric field (|Ex|) map of the simulated response of TiN-Si_3N_4-TiN based design showing electromagnetic wave anomalously reflected in opposite directions, at an angle of $\theta \sim 60^o$ for 1.3 μm LCP (c) and at $\theta \sim 130^o$ for 1.15 μm RCP (d) incident wave (colorbar indicates amplitude).

To fabricate the designed metasurfaces, first, the metal-dielectric-metal stack was created on crystalline MgO substrate using a bottom-up growth technique. This was followed by top-down electron beam lithography and dry halogen plasma etching to define the metallic NA elements (for details, see supporting information, section 1). Top down, cross-section, and tilted view of scanning electron microscope (SEM) images of a fabricated metasurface are shown in Figure 4.5 (a-c).

A variable angle spectroscopic ellipsometry (VASE) (Figure 4.6S) set up is used to experimentally measure the response of the fabricated metasurface. The set up employs a tunable monochromatic source, a polarizer, followed by a retarder device to generate circularly polarized wave. A rotating detector arm allows for collecting the anomalously reflected light as a function of angular dispersion. Experimentally measured angular dispersion from the two fabricated metasurface devices are plotted in Figure 4.5 (d, e). Photonic SHE is illustrated as the opposite spin components (LCP and RCP) of incident light are reflected in the mirror symmetric directions. Each color on the plots (Figure 4.5 (d, e)) represents a different frequency component and the peak positions are as obtained by the generalized Snell's law. As in spectrometers, this creates a spatial dispersion of the frequency spectrum. Our experimental set up restricts the collection of light reflected at angles $< 38^{o}$ (that corresponds to $\lambda < 0.94$ μm for supercell period of 1.5 μm). The reflected power efficiency reaches a maximum of ~28% at 1.1 μm for the TiN based device (~19% at 1.04 μm for the ZrN based one) and gradually decreases for both lower and higher frequencies as expected from the simulation results shown in Figure 4.3 (d, e).

Patterning films into nanoscale antenna geometry is known to increase effective optical losses of plasmonic metals owing to large scattering from the edges, and surface roughness resulting from chemically reactive high energy plasma etching processes. These factors adversely affect the device performance and reduce power efficiency of the fabricated metasurface[259]. Betterment of the optical properties of the unpatterned continuous films of TiN, ZrN and replacement of the chemically reactive high energy etching process-step with a lift-off type technique is expected to improve power efficiency further (see supporting information, section 3, Figure 4.8S).

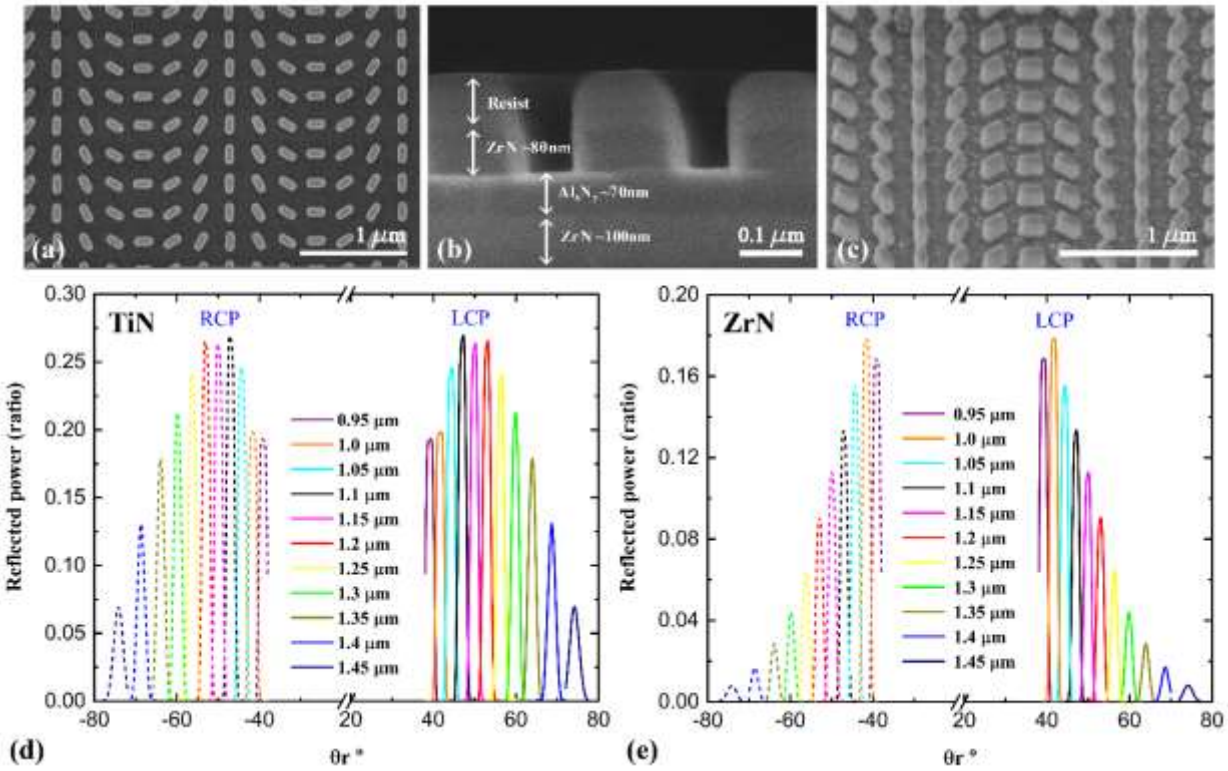

Figure 4.5 (a) Top-view, (b) cross-section, and (c) tilted (at 30o) scanning electron microscope (SEM) image of the fabricated metasurface. Image (a, b) are taken from a ZrN based and (c) from a TiN based fabricated sample with 1.5 μm supercell period. Experimentally measured reflected power collected as a function of reflection angle, from the fabricated (d) TiN and (e) ZrN based metasurfaces for different frequency incident beams with left or right circular polarization.

4.4 Conclusion

In this work, we designed, fabricated and characterized, two phase gradient metasurfaces utilizing refractory plasmonic metal nitrides- TiN and ZrN, that exhibit photonic spin Hall Effect by separating in reflection, the two opposite spin components of the incident light. The measured power efficiency of this first demonstration compares slightly lower to a previous Au based design[212] but offers a much broader bandwidth of operation (0.9-1.6 μm). Refractory TMNs have brought exciting opportunities to plasmonic devices with their high temperature and mechanical stability, in addition to the metal-like optical properties and compatibility with CMOS processing. Although, their advantages are many and the materials are deemed promising for a long time, there have been very few demonstrations of real devices involving transition metal nitrides. This first demonstration of phase gradient metasurfaces using transition metal nitrides aims to fill this gap by successful integration of the new materials (and their stacks with other materials) in established

device architectures. The processing techniques developed in this work can be translated to practical device demonstrations by utilizing low-cost, large-area nano-structuring techniques such as nanoimprint and conformal imprint lithography. We believe this work will play a key role in shaping the future of transition metal nitrides based plasmonics, as well as in assimilating the material class into the arena of compact, durable and cost effective flat optics.

4.5 APPENDIX Methods

Nitride thin film preparation:

TiN and ZrN films are grown using a DC magnetron sputtering process where Ti or Zr is sputtered off commercially available targets (Plasmaterials, 99.995%) in an argon (Ar) and nitrogen (N_2) based plasma (base pressure of 10^{-8} Torr) environment onto a clean substrate of choice at 850 ^oC. Various sputtering process parameters as well as substrates have been shown to affect the grown thin film properties and have been optimized to obtain the best achievable optical quality. Commercially available crystalline magnesium oxide (MgO) substrates were used for this study due to a close match of MgO lattice constant to that of titanium nitride (TiN)[260]. This leads to a preferential single crystalline growth of TiN film on MgO. This was confirmed experimentally in an earlier work[245]. For zirconium nitride (ZrN), same MgO substrate have been used for consistency of comparison, even though the lattice constants are different. As expected from earlier studies, the films have appearance close to Au films of similar thickness.

Fabrication:

In case of the ZrN based device design, all three layers (ZrN-Al_xN_y-ZrN) were deposited in a DC magnetron sputtering chamber. For the design using TiN, the samples were taken out of chamber after the first TiN growth and the dielectric Si_3N_4 layer was deposited using chemical vapor deposition (CVD) method. This was followed by sputtering of the top TiN.

Electron beam lithography followed by dry etching was used to fabricate the nanostructures. The samples TiN-Si_3N_4-TiN and ZrN-Al_xN_y-ZrN were cleaned with toluene, acetone, followed by IPA rinse to remove organic and other contaminations. First, a sacrificial layer of PMMA (950 A2) was coated followed by baking at 160^{o}C for 5 min. This layer helps remove the second resist layer coated on top. After cooling to ambient temperature, a second layer of electron beam resist 'HSQ' (hydrogen silsesquioxane, XR 1541, 6 wt% by Dow Corning Chemicals) was coated and cured at 120^{o}C for 3 min. Thickness of this resist layer was ~130 nm. After electron beam exposure, the resist was developed using tetra-methyl ammonium hydroxide (TMAH) (25% in H_2O) solution for 25 sec followed by 30 s rinse in DI water. At this stage, the intended metasurface pattern was transferred onto the resist layer.

In the first step of dry etching, the sacrificial PMMA layer was etched using O_2 plasma. Following that, an inductively coupled plasma of halogenated (BCl_3, and/or Cl_2) and Argon (Ar)

gas mixtures was used to etch the top metal layer. For TiN, 26 sccm Cl_2 flow rate, 0.6 Pa pressure, 150 Watt forward power, and 60 Watt bias power are used. ZrN is relatively a harder material. For ZrN, 850 Watt forward power, 60 Watt bias power, 0.8 Pa pressure, and a gas mixture of BCl_3 (30 sccm), Cl_2 (30 sccm), and Ar (10 sccm) are used. To maintain a high degree of anisotropy in the structure, a relatively large source power, low pressure and a small target bias power were used. Etching time varied depending on the film thickness. SEM images of the final structures are shown in Figure 4.5 (a-c).

Optical measurements:

For the optical measurements, the sample is mounted onto the rotatable stage of the VASE set – up Figure 4.6S. The monochromator source, together with a polarizer, and a retarder generate circularly polarized light. The incident angle is fixed at very close to normal (0.1^o). The anomalously reflected light is then detected by the rotating detector arm which scans the angles. Due to finite width of the incident and detector arms, there's a limitation of 38^o to the minimum reflection angle that can be measured. Hence all our experimentally measured spectra (shown in Figure 4.5 (d, e)) are depicted for angles 38^o and beyond. The analyzer in the detector arm helps in distinguishing polarization components of received light.

Simulations:

In the commercially available multiphysics tool COMSOL, the wave-optics module has been used to perform full wave finite element method simulations (frequency domain). Direct stationary "PARDISO" solver is chosen for the calculations. Periodic boundary condition was used. A scattering boundary excitation at normal incidence is used for the unit cell optimization. For supercell simulations, port excitation mode is used. Transmission, reflection and absorption are calculated using S-parameters and anomalous mode is detected using diffraction orders. Relevant geometry parameters are discussed in the main manuscript. Experimentally measured spectral dependence of complex dielectric permittivity values for TiN/ZrN on MgO (bottom layer), Aluminum nitride (Al_xN_y) and silicon nitride (Si_3N_4) (spacer layers) and TiN/ZrN on respective spacer layer (as presented in Figure 4.2 (a, b, and d) and Figure 4.7S) were input into the COMSOL model as well.

4.6 APPENDIX Supplementary Information

Section 1: Optical Measurements

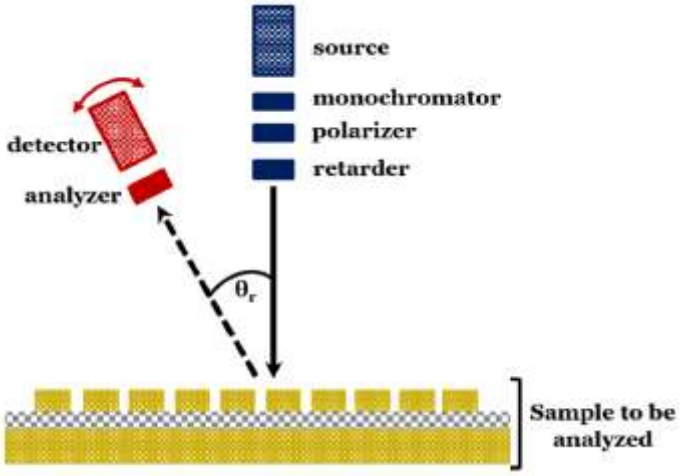

Figure 4.6S Schematic of Variable Angle Spectroscopic Ellipsometer (VASE) set up used to characterize the optical properties of the thin films as well as the optical response of the fabricated metasurface devices.

$$\boldsymbol{\varepsilon(\omega) = \varepsilon_\infty - \underbrace{\frac{\omega_p^2}{\omega(\omega + i\Gamma_p)}}_{Drude} + \underbrace{\frac{f_1}{\omega_1^2 - \omega^2 - i\omega\Gamma_1}}_{Lorentz\ 1} + \underbrace{\frac{f_2}{\omega_2^2 - \omega^2 - i\omega\Gamma_2}}_{Lorentz\ 2} + ..}$$

Equation 4.6S

Table 4.1S Optical properties model parameters as derived from ellipsometry measurements of ~200 nm thick films of TiN and ZrN grown on MgO

	Drude			***Lorentz 1***			***Lorentz 2***			***Lorentz 3***		
	ε_∞	ω_p^2 *(eV)*	Γ_p*(eV)*	f_1	ω_1 *(eV)*	Γ_1*(eV)*	f_2	ω_2 *(eV)*	Γ_2*(eV)*	f_3	ω_3 *(eV)*	Γ_3*(eV)*
TiN	3.419	55.81	0.197	42.42	4.161	0.661	1000.0	15.70	202.84	---	---	---
ZrN	3.323	48.67	0.133	7.942	0.738	1.693	1.101	2.775	0.850	30.52	4.829	0.788

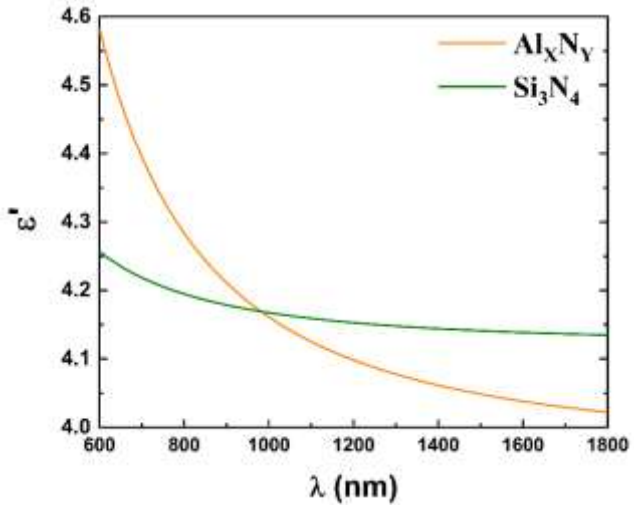

Figure 4.7S Experimentally measured real (ε') part of dielectric function of Al_xN_y (~70 nm) on ZrN and Si_3N_4 (~60 nm) on TiN film respectively. These measured dispersions are input into the COMSOL simulation model.

Section 2: Material Parameters and Power Efficiency

To elaborate on possibilities of improving the power efficiency, here, we compare the device performance with two different characteristics of the constituent material. In the Figure 4.8S (a) shown below, optical properties of TiN are compared as the thin films (70-80 nm) are grown on two different substrate materials (i.e. crystalline MgO [100 face] and CVD grown amorphous Si_xN_y). Crystalline MgO provides a closer match to the lattice constant of TiN as compared to amorphous Si_xN_y leading to largely different crystal structure and in turn optical properties of the two films. On amorphous substrate, the film assumes a more polycrystalline nature with smaller grain boundaries leading to reduced metallicity and increased losses. On the right, Figure 4.8S (b) shows the simulation results for the TiN meta-unit array (as in Figure 4.3) with the optical properties of the top TiN nanoantenna layer varied between the one as grown on crystalline MgO (dashed line) and as grown on amorphous Si_xN_y (solid line). Replacing the top TiN NA with a lattice matched, more metallic, and less lossy one (as on MgO) (dashed line) increases the reflected power efficiency by ~23% as compared to the current design (as on Si_xN_y) (solid line). This goes to show that the improvement of the quality of nitride can significantly enhance the device performance and make it comparable to the Au based design. This can be achieved by using a dielectric spacer that has a lattice constant close to that of the top metal nitride.

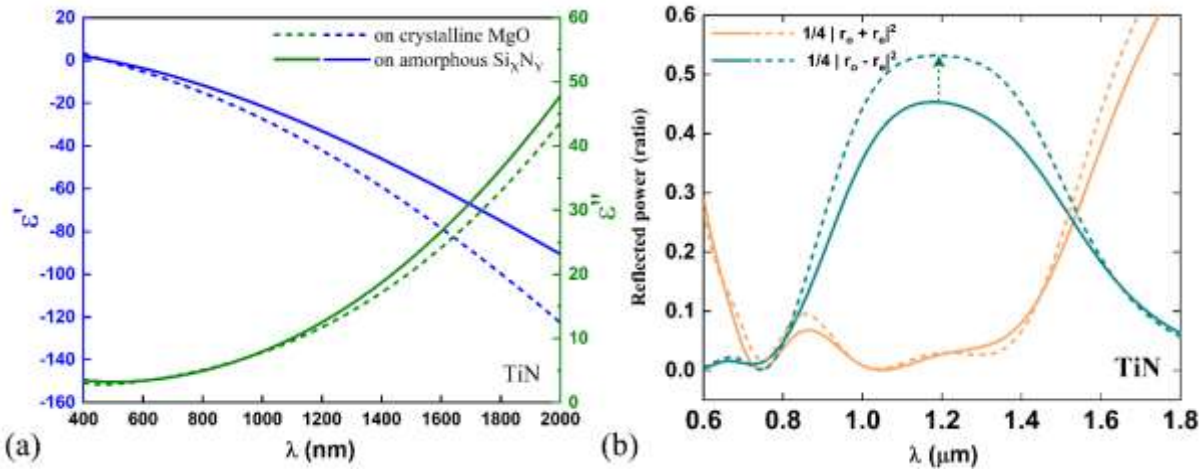

Figure 4.8S (a) Comparison of experimentally measured real (ε') (blue) and imaginary (ε") (green) parts of the complex dielectric function (ε) of TiN thin film grown on crystalline MgO (dashed) and on amorphous silicon nitride (solid). (b) Simulation results for TiN/Si_xN_y/TiN based meta-unit array showing reflected power output to the anomalous co-polarized component (indicated $1/4\,|(r_o - r_e)|^2$, green) and the normal cross-polarized one (indicated $1/4\,|(r_o + r_e)|^2$, orange) where the optical properties of the top TiN NA layer is varied between the two values shown in (a), the one as grown on crystalline MgO (dashed line) and as grown on amorphous Si_xN_y (solid line).

CHAPTER 5. REMOTE OPTICAL SENSING OF HIGH TEMPERATURES IN EXTREME ENVIRONMENTS WITH REFRACTORY METACAVITY

ABSTRACT

Utilizing the temperature-dependent optical properties of refractory transition metal nitride as well as refractory dielectric thin films, we design, fabricate and characterize a planar, nanophotonic metadevice for remote optical sensing of very high surface temperatures ranging up to 1200^{o}C. A hybrid plasmonic metasurface cavity design with refractory material components, namely titanium nitride (TiN) and silicon nitride (Si_3N_4), is implemented for the spectral window of 900 nm to 1400 nm. The temperature-variant optical properties of the constituent materials (TiN, Si_3N_4) enabled a metadevice with strong polarization-dependent resonant reflectance response. Large variations are measured in the temperature dependent reflectance spectra of the device that acts as the sensor read-out signal. This efficient, resonant, planar refractory sensor allows for scalability and easy deployment on hot surfaces under inspection. In addition, the device enables true remote all-optical measurement by keeping other ancillary systems outside of the hot ambient and therefore is especially relevant for applications in harsh environments.

5.1 Introduction

Consistent with the rapid progress of aerospace, automotive, and energy industries, the demand is on the rising for high-accuracy, repeatable, and durable temperature sensing techniques for temperatures above 700^{o}C. As an example, in jet-propulsion systems used by space research as well as the defense industry, high-temperature sensors are imperative for ensuring accurate design, maintaining operation, and monitoring safety[261]. In monitoring components in propulsion systems, the temperature sensors need to operate under 500^{o}C-1000^{o}C and maintain stable lifetime through 100,000 hours[262]. Despite the availability of many different high accuracy sensing systems (piezoelectric, capacitive, piezoresistive, etc.), their applicability to harsh environments is largely limited by the thermal drift effects, low durability and temperature constraints of the control systems to be co-mounted along with the sensor[263,264]. To this, optics-based sensing techniques allow large room for improvement. Fiber optic based sensors have the advantages of low EMI,

high accuracy, corrosion resistance, and high operating temperatures (>2000^{o}C in a sapphire-based fiber) and are now widely in use[265,266]. However, the multimode nature of the sapphire-based optical fiber distorts measurements by introducing additional modes into the fiber. Also, these measurements require special packaging to protect the mechanically fragile fiber and its tip. At very high temperatures, thermal expansion related mismatch between the packaging and the fiber introduces fault into the measurements[267–269]. The significant limitations of the state-of-the-art sensing systems necessitate the need for a robust and accurate high-temperature sensing mechanism, with the capability of remote operation that is congruent with chemically aggressive and harsh environmental conditions.

To address these challenges, in this work, a planar nanophotonic cavity with a metasurface based on refractory materials is designed, fabricated, and tested for high-temperature sensing. In optical frequencies, nanophotonics opens the door to a variety of means to manipulate light propagation characteristics[270]. Among these means, metasurfaces – a broad class of artificial planar optical elements – are widely known for achieving arbitrary control of light scattering parameters such as amplitude, phase, and polarization[12]. This flexible control is achieved through the collective scattering from an ensemble of nanoscale optical resonators, with uniquely designed spectral and polarization response, placed at the interface of two media[186]. The response of such a system depends largely on the optical properties of the constituent material components, and therefore, suitable material choices are often the most important element for realizing the desired functionality[216]. In the case of plasmonic systems, noble metals such as gold and silver are prolifically used due to their excellent metallic nature as well as low optical losses in the visible and near infrared (IR). However, due to their softness and malleability, low melting point, chemical reactivity, they are often unsuitable for applications requiring stable operation at elevated temperatures, upon external mechanical stress, or in chemically reactive ambient[70]. Also, the robustness of nanostructures operating at high temperatures becomes even more challenging due to the melting point depression effect that reduces damage threshold temperatures by a few hundred degrees compared to the bulk melting point[65,228,271]. Therefore, for the design of an optical sensing device aimed at temperatures above 700^{o}C, we turn to the refractory plasmonic materials such as the family of transition metal nitrides (TMN) (e.g., titanium nitride (TiN), zirconium nitride (ZrN), tantalum nitride (TaN))[70,71,248,272].

These refractory metals have gained great attraction in the past decades in plasmonics and nanophotonics research community[63,247,273,274]. In addition to their high mechanical durability and very high melting points (~3000^{o}C), these conductive ceramics exhibit strong similarity in their optical properties to the most popular noble metals (Au and Ag). The plasmonic properties and the material growth techniques of titanium nitride (TiN) have been rigorously investigated [72,74,228,234,237–241]. The plasma frequencies of TiN is in the visible range, but it typically exhibits larger optical losses compared to the commonly used noble metals[275]. The optical properties of the TMNs depend on many factors, including the lattice structure, crystal defects, surface roughness, grain sizes, stoichiometry, etc. As a result of different growth conditions during the thin film deposition, the optical properties of the metal nitrides vary within a large spectrum[233]. Beyond its elevated damage threshold temperature, non-stoichiometric TiN thin films also exhibit a strong temperature dependence to the complex dielectric permittivity in optical frequencies which has been shown in a previous work[245]. This dependence is utilized in the proposed metamaterial systems to design an optical response that varies with temperature and therefore allows for sensing.

In this work, a metal-insulator-metal (MIM) stacked type metamaterial geometry that supports photonic, plasmonic, and hybrid-resonant modes are employed to obtain frequency-dependent and polarization-selective spectral responses. The multi-layer stacked device geometry allows for easier operation in the reflection mode and is optimized through simulation to achieve strong resonance modes in the near-IR to enable higher sensitivity. In a typical design, the stack of ultra-thin films and nanostructured layers are subwavelength sized and comprises a total thickness of less than one micron. In addition to the nanoscale dimensions, the planar metamaterial device also has the benefit of scalable fabrication techniques and can be easily deployed onto the surfaces of systems operating in harsh environmental conditions, for example, the outer skin of fuel combustion chambers. The top interface of the metamaterial or metasurface is illuminated with a light source, either through free space or via an optical fiber, and the reflected signal can be detected using remote detectors. Therefore, allowing for a remote sensing technique wherein, the detector, analyzer, and other ancillary components can be located outside the harsh environment. The sensor system can be employed in applications including but not limited to aircraft and propulsion engines and engine parts, fuel cells, power plants, refineries, and drilling rigs.

5.2 Optical properties of constituent material platforms

In our metal-insulator-metal stacked geometry, the metal component is titanium nitride (TiN), and the dielectric one is silicon nitride (Si_3N_4). Si_3N_4 is chosen for its robustness at high-temperature operations (melting point 1900^{o}C) and also to avoid oxygen contamination into the adjacent TiN layers. Both TiN and Si_3N_4 layers are deposited at high temperatures (800^{o}C) using DC magnetron sputtering and low-pressure chemical vapor deposition techniques, respectively. A commercial variable angle spectroscopic ellipsometry (VASE) instrument is used to measure the optical response of the films, which are then fitted to an analytical model (Drude and Lorentz oscillators) to extract the complex dielectric permittivity, ε. The plasmonic behavior of TMNs is critically dependent on their fine crystal structure, which is largely affected by the growth conditions as well as the nature of the underlying layer. Single crystalline magnesium oxide is used as the bottom-most substrate as its lattice constant matches closely to that of TiN and therefore promotes an epitaxial, single crystalline growth of the TiN. When grown on top of a Si_3N_4 layer, the amorphous nature of the dielectric promotes a polycrystalline structure of the TiN with reduced metallicity and increased optical losses[275]. Therefore, we measure the temperature-dependent complex dielectric permittivity spectrum of each of the constituent material layers of the metamaterial device; namely, epitaxial TiN deposited on the MgO substrate, Si_3N_4, and polycrystalline TiN deposited on Si_3N_4. Among these, we have previously studied the temperature dependent optical properties of the TiN on MgO[245]. Our studies have shown that the change in optical properties in TiN thin films stems from the interplay of enhanced electron-phonon scattering and changing electron effective mass at elevated temperatures while preserving the mechanical structure. This results in a reversible variation and upon cooling down the original room temperature optical properties can be obtained[245].

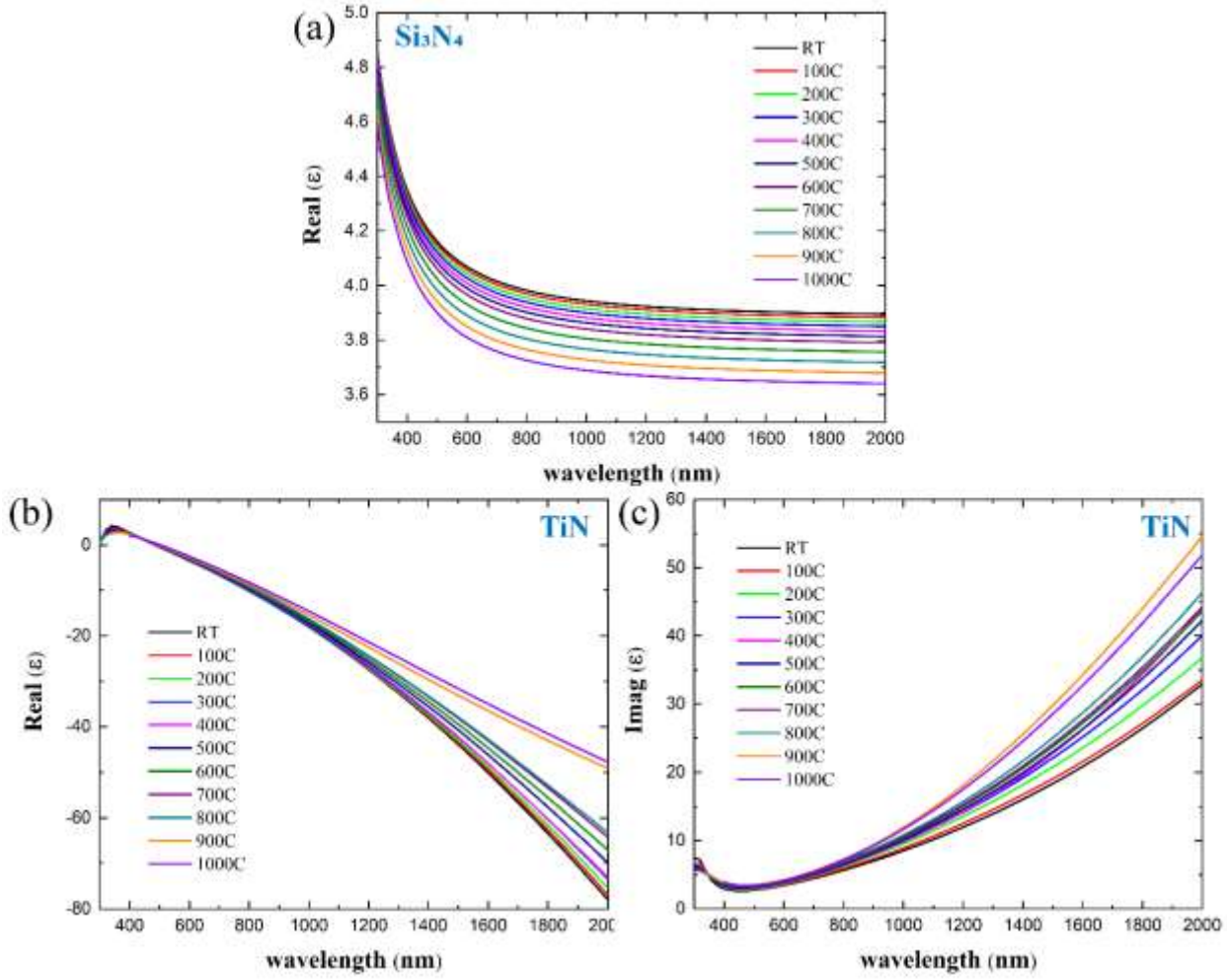

Figure 5.1 Experimentally measured temperature-dependent optical properties of thin films of constituent materials. The real part of complex dielectric permittivity of (a) Si_3N_4 thin film grown on Si, (b) TiN thin film grown on Si_3N_4, and (c) corresponding imaginary part of permittivity for TiN grown on Si_3N_4.

The temperature dependent changes in the complex dielectric permittivity function (ε) for a ~300 nm Si_3N_4 thin film deposited on Si substrate are measured for temperatures ranging from room temperature (RT) to 1000^{o}C with steps of 100^{o}C, and the results are summarized in Figure 5.1 (a). The measured raw data is fitted to a Cody-Lorentz (C-L) general oscillator model to extract the ε values. For the fitting, similar temperature dependence is measured for the Si substrate. A monotonic (linear) decrease in the real part of the permittivity is observed with increasing temperature. In NIR, in the wavelength window of 1000nm - 2000 nm, the magnitude of real (ε) is reduced by ~7.7% when the temperature is increased from RT to 1000^{o}C. We believe this

variation results from the temperature dependence of the effective band-gap. The effective band-gap extracted from the C-L oscillator model shows a monotonic decrease with increasing temperature that is summarized in Table 5.1S. On the other hand, the optical band-gap of the LPCVD grown Si_3N_4 is >2.5eV and therefore exhibits negligibly small optical losses (imaginary part of the ε) in the spectral range of interest (400-2000 nm). The temperature dependent variance of the imaginary part of the ε is negligible as well and therefore, are not shown. Similarly, temperature-dependent ε values are measured for a TiN thin film grown on top of a ~300 nm thick Si_3N_4 film (on Si substrate) for the same temperature range (Figure 5.1 (b, c)). Following a similar trend as was previously observed for the epitaxial TiN[245], both real and imaginary parts of the ε for this polycrystalline TiN film exhibit significant variation from ambient condition values with increasing temperature. The real part shows a monotonic decrease in magnitude whereas the imaginary part experiences a monotonic increase with rising temperature. In addition, the relative difference among the dispersion characteristics increases at longer wavelengths (Figure 5.1 (b, c)). This reduction in metallicity and increase in optical losses can be attributed to an increase in the Drude broadening term resulting from increasing electron-phonon interactions and changing electron effective mass with the increase in temperature. For more details on the optical measurement and data extraction methods, see supplementary information. These measured optical properties of all constituent layers are incorporated into our numerical simulations based on the finite-difference time-domain (FDTD) method to achieve an optimized geometry of the metamaterial sensor device.

5.3 Design and Demonstration

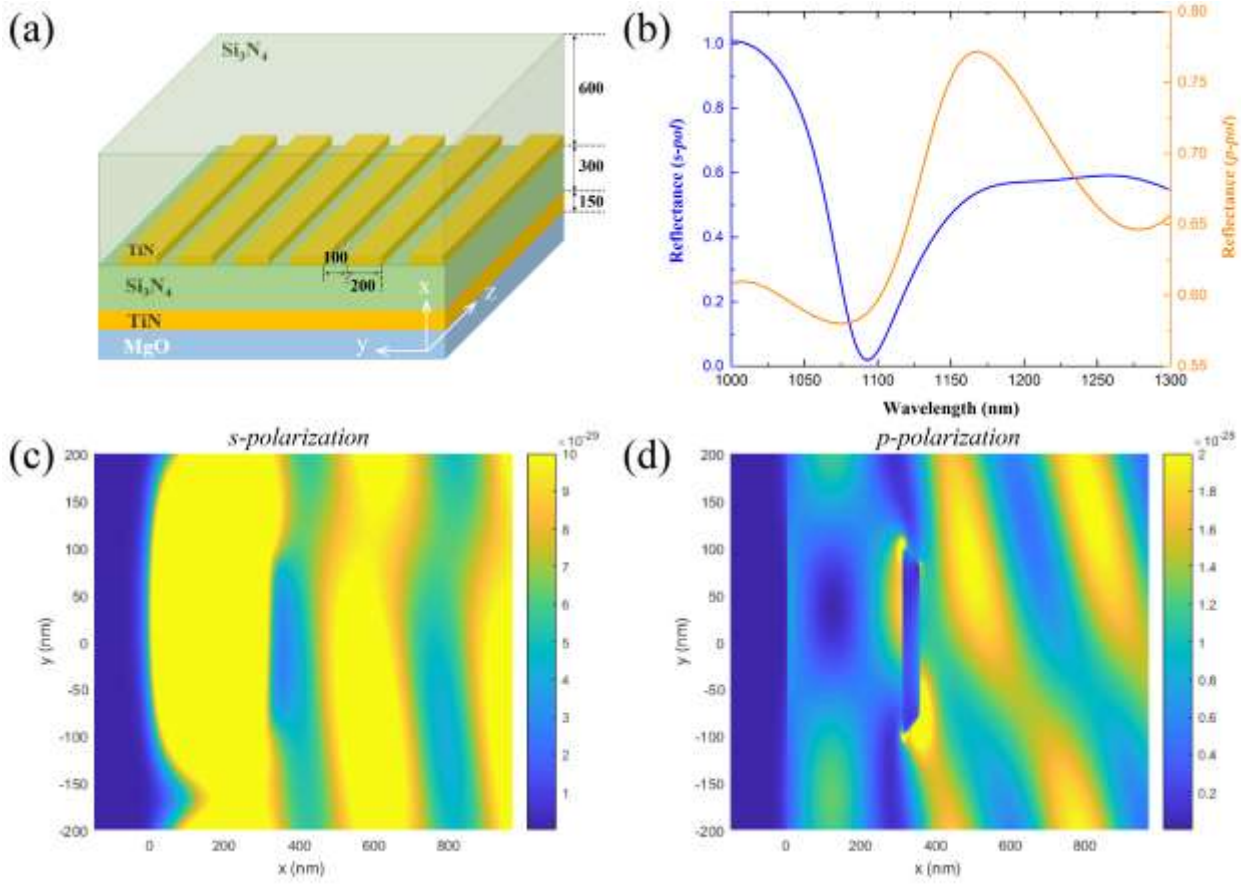

Figure 5.2 (a) Schematic of the proposed hybrid plasmonic metasurface-cavity structure (all dimensions are shown in nanometers unit); (b) simulated reflectance spectra for two orthogonal polarizations at 40^o angle of incidence; E-field maps in the cross-section of the structure for the resonant mode (c) at 1080 nm for *s-polarized* (TE) incidence (with the predominant photonic nature of the mode) and (d) at 1280 nm for *p-polarized* (TM) incidence (a coupled plasmonic-cavity mode).

Among several approaches to leverage these significant temperature-dependent intrinsic materials characteristic through metamaterials and metasurfaces designs, we explore a hybrid plasmonic metasurface cavity approach. This design aims to create polarization-dependent resonance spectra in reflectance spanning the near-IR window. With increasing temperature, the optical properties of the constituent materials show a gradual variation, which in turn varies the resonant optical response of the device to be quantified as the sensor read-out signal. To improve the sensitivity and accuracy of the sensing signal we consider a hybrid plasmonic metasurface cavity device design operating at a large angle of incidence (40^o). Through this design, we aim to

create strong polarization-dependent resonating modes in reflection the near-IR spectral window (900 nm to 1400 nm). Operating at resonance conditions allow us to enhance the sensitivity of the device to the change in temperature. The optical properties of the constituent materials show a larger temperature-dependent change in the near-IR. Therefore, choosing this spectral window allow us to amplify the relative change in the device response with temperature. To this, using specific polarization dependent response lets us improve the fidelity of the measured signal with better distinction to the un-polarized background emission. The background blackbody radiation follows a strong angular dependence scaling as a factor of cosine of the angle. Utilizing this dependence to our advantage, the device is designed to operate at a high angle of incidence (40^o) hence reducing the contribution of the background emission on the measured reflectance data. Maximum angle of operation is limited by the experimental measurement set up (for details, see Supplementary Information).

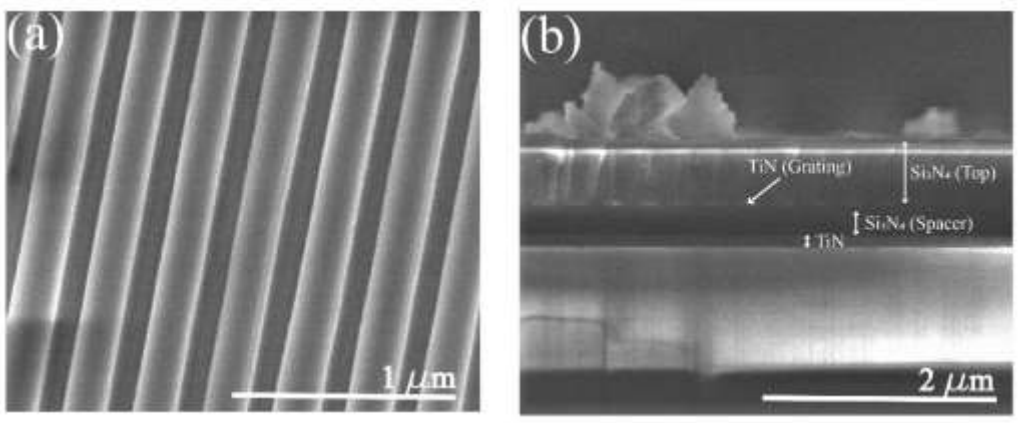

Figure 5.3 Scanning electron microscope image of (a) the top view of the fabricated TiN grating structure and (b) the cross-section view of a fully fabricated device indicating different layers as pointed

Figure 5.2 (a) depicts a schematic of the proposed metacavity. The geometry is optimized using FDTD simulations to obtain two strong resonances at different spectral locations for two orthogonal linearly polarized plane wave excitations at an incidence angle of 40^o. A single-period plasmonic grating made of the plasmonic TiN is placed on a bilayer stack of TiN (~150 nm) and Si_3N_4 (~300 nm). Another thick Si_3N_4 (~600 nm) layer deposited on top the grating acts as an additional cladding for the TiN grating to prevent it from degradation in oxidizing environments

and to form additional photonic cavity resonating modes. The structural dimensions are optimized through iterative simulations to obtain two distinct resonances at different frequencies upon two orthogonal polarizations (*s*- and *p*-). The final optimized dimensions are indicated in Figure 5.2 (a).

Figure 5.2 (b) shows the simulated reflectance spectra for the optimized geometry. For *s-polarized* incident light, a Fabry-Perot cavity type resonating mode (at 1080 nm) is excited in the structure (see the cross-section electric field $|E_{norm}|$ map in Figure 5.2 (c)). Whereas for the *p-polarized* excitation, a surface plasmon polariton mode is excited in the TiN grating structure that couples with the photonic modes in the adjacent Si_3N_4 layers to create a hybridized plasmonic cavity resonance at 1280 nm. The cross-section *E*-field mapped in Figure 5.2 (d) indicates the nature of this hybridization inside the structure. Upon introducing the temperature-dependent optical properties of the constituent materials, in this optimized device design, we observe significant variation in the reflectance spectra for two orthogonal polarized incidences throughout the whole spectral window.

A prototype device is fabricated to validate the performance of the optimized design (for details, see Methods). First, a bottom-up stack of TiN (150nm)-Si_3N_4 (300 nm)-TiN (50 nm) is created on the crystalline MgO substrate. Then the top TiN layer is patterned into grating structures using an electron-beam lithography technique followed by reactive ion etching of the TiN and removal of the residual resist. A top view SEM image of the fabricated device at this step is shown in Figure 5.3 (a). After this, as the last step, a thick (600 nm) Si_3N_4 film was deposited onto the patterned sample. An SEM image of the cross-section of a fully-fabricated device is shown in Figure 5.3 (b) indicating different layers of TiN, Si_3N_4, and the buried TiN gratings.

Experimental characterization of the fabricated device has been carried out using an in-home custom set-up that modifies the standard VASE ellipsometer for measuring reflectance at elevated temperatures. The device was heated using a commercially available heating cell (from *Linkam* Scientific) which is integrated into the VASE set-up (for more information on the set-up, see Supplementary Information section 1). As expected from simulations, the measured reflectance spectrum at RT shows a strong polarization-dependent response with the two different resonance modes appearing at ~1100 nm and at ~ 1280 nm for *s*- and *p*- polarized incidence, respectively. Few features such as the FWHM and the reflection amplitude of the two resonances vary in the experiment from simulation which can be attributed to the imperfections from the device

fabrication as well as the measurement set-up. The device is then heated at steps of 100^{o}C, and reflectance data are collected using the VASE. Figure 5.3Figure 5.4 (a, b) summarizes the temperature-dependent variation of the device response for *s*- and *p*- polarized light at 40^{o}-angle of incidence (measured from normal). Between RT and 700^{o}C, large variations are observed throughout the entire spectral window but further amplified around the resonances. The relative variation of the response is distributed – 1100 to 1200 nm for *s-polarized* incidence and 1050 – 1300nm for *p-polarized* incidence allowing for rather broad spectral windows of operation for the device. The variation measured over the broad window also increases the fidelity of the device signal. A ~ 30% relative change in the reflection amplitude can be measured within at ~1150 nm for both polarizations. However, the background radiation from the heating element in our experimental set-up starts to interfere with the optical signal in this IR spectral window of 900-1400 nm. At the temperature of 800^{o}C and above, the heating element starts glowing brightly and the emitted radiation (wavelength dependent, follows from Wien's displacement law) has a finite contribution at measurement spectral window[276]. This radiation saturates the photodetector on our VASE set-up and therefore hinders collection of reflection data beyond 800^{o}C. That saturation limits the experimental reflectance measurements only up to the temperature of 700^{o}C. However, based on the material properties and earlier measurements of the temperature dependence, we expect the device response to follow the trend and to operate reliably up to temperatures of 1200^{o}C. The repeatability of the device response is tested as well. The RT response of the device is measured before starting heating and after multiple cycles of heating to 1000^{o}C followed by cooling to RT. When compared, the reflectance spectra match almost exactly for the entire spectral window of operation indicating that no structural or material related degradation of the device accumulates through multiple heating and cooling cycles (shown in Figure 5.4 (c)).

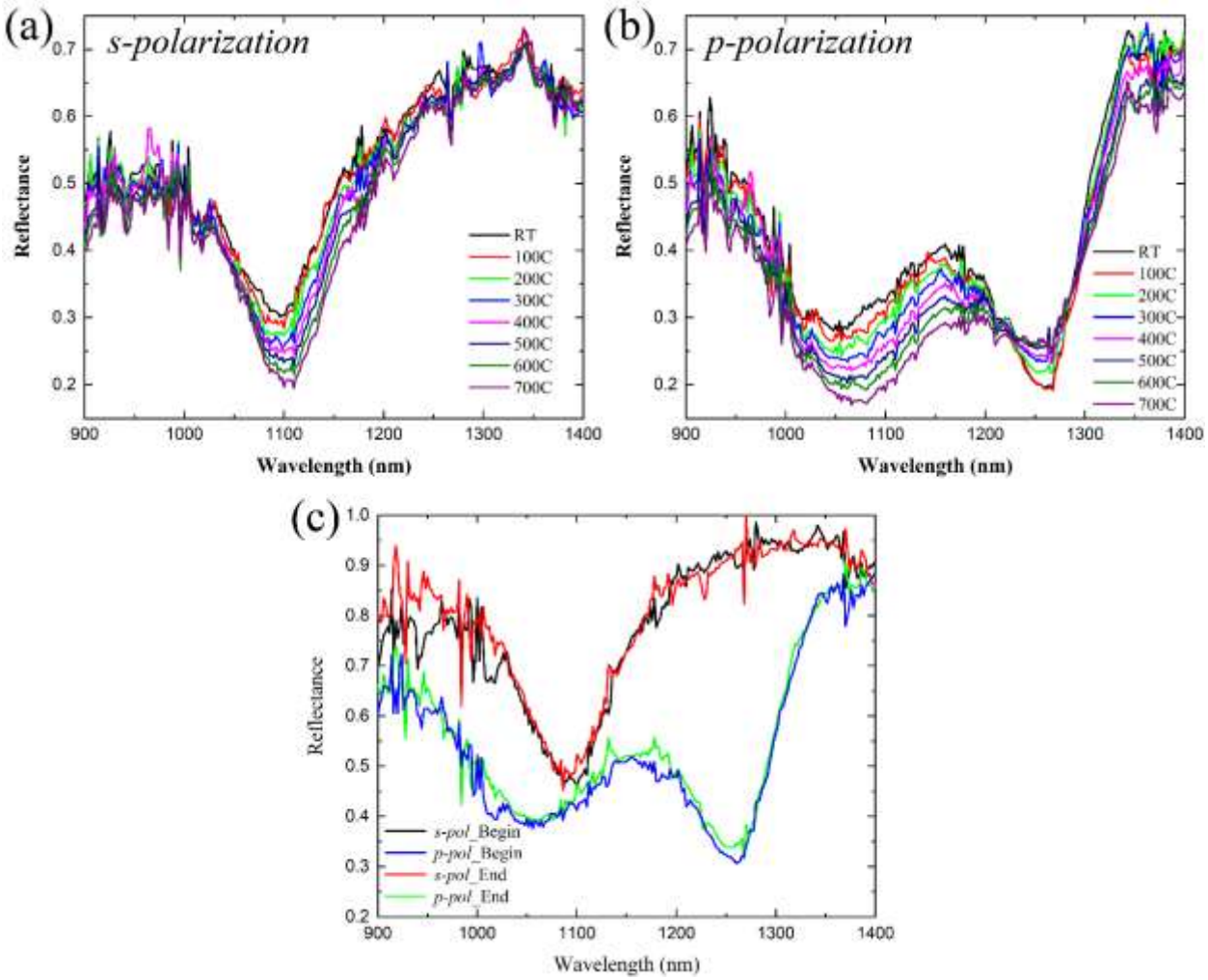

Figure 5.4 The temperature dependent reflectance spectra experimentally measured with the fabricated device heated for temperatures ranging from RT to 1000^{o}C with increments of 100^{o}C at an incidence angle of 40^{o} for the two orthogonal polarizations (a) *s*- and (b) *p*- respectively, (c) comparison of reflectance spectra measured at RT on the same device before starting heating (indicated as *s-pol*_Begin, *p-pol*_Begin) (shown in (a, b)) with the spectra measured on the same device after 2 heating cycles (of RT→ 1000^{o}C→ RT) (indicated as *s-pol*_End, *p-pol*_End) for both orthogonal polarized incidence.

5.4 Conclusion

In this work, we have studied a high-temperature sensing system with resonant optical metamaterials that can survive temperatures as high as 1200^{o}C. We have designed, fabricated and characterized a resonant, nanophotonic metamaterial device with a broad operating spectral window in the near-IR (wavelength range of 900nm to 1400nm). The device design utilizes the temperature-dependent variation of optical properties of the constituent refractory material

components. The changing material properties lead to variation in the resonant optical response of the device that is amplified at resonance conditions and is measured via a relatively straightforward reflectance measurement technique. The hybrid plasmonic metasurface cavity device was designed, fabricated and experimentally characterized in the NIR wavelength window of 900-1400 nm, demonstrating a promising route for remote sensing of high temperatures at harsh ambient conditions. Temperatures can be read out via measuring the relative change in the reflectance spectrum experienced by the device at elevated temperatures. This remote, optical temperature sensing technique is valuable, especially at high-temperature ranges (500^{o}C-1200^{o}C) and extreme environment conditions where other traditional sensing methods such as thermocouples and resistive temperature detectors start to fail. As the size of the collected sensor data increases, more efficient ways of extracting information through advanced signal processing algorithms should be employed to further improve the fidelity and accuracy.

5.5 APPENDIX Methods

Nitride thin film preparation:

TiN films are grown using a DC magnetron sputtering process where Ti is sputtered off commercially available targets (Plasmaterials, 99.995%) in an argon (Ar) and nitrogen (N_2) based plasma (base pressure of 10^{-8} Torr) environment onto a clean substrate of choice at 800^{o}C. Various sputtering process parameters as well as substrates have been shown to affect the grown thin film properties and have been optimized to obtain the best achievable optical quality. Commercially available crystalline magnesium oxide (MgO) substrates are used for this study due to a close match of MgO lattice constant to that of titanium nitride (TiN)[260]. The lattice match leads to a preferential single crystalline growth of TiN film on MgO, as has been confirmed experimentally in an earlier work[245]. Si_3N_4 films are deposited in a tube furnace (ProTemp) using low-pressure chemical vapor deposition (LPCVD) technique at 800^{o}C using silane (SiH_4) and ammonia (NH_3) gas chemistry. The films are Si-rich and amorphous.

Fabrication:

For realizing the hybrid plasmonic metasurface geometry (Figure 5.2 (a)), first, the thin film stack of TiN-Si_3N_4-TiN is created. At this stage, electron beam lithography and dry reactive ion etching techniques are utilized to fabricate the grating structure. The sample with TiN-Si_3N_4-TiN stack is

cleaned with toluene, acetone, followed by IPA rinse to remove organic and other contaminations. Following this, a sacrificial layer of PMMA (950 A2) is coated followed by baking at 160^{o}C for 5 min. This layer is needed to facilitate easy removal of the second resist layer coated on top of this one. After cooling the PMMA coated sample to ambient temperature, a second layer of electron beam resist 'HSQ' (hydrogen sislesquioxane XR-1541 (6 wt%) by Dow Corning Chemicals) is coated and baked at 120^{o}C for 3 min. The thickness of this resist layer is ~130 nm. After electron beam exposure, the HSQ resist is developed using tetra-methyl ammonium hydroxide (TMAH) (25% in H_2O) solution for 25 sec followed by 30 s rinse in DI water. At this stage, the intended metasurface pattern is transferred onto the resist layer. Then using reactive ion etching (RIE) technique, the sacrificial PMMA layer was etched using O_2 plasma. Following that, an inductively coupled plasma of chlorine (Cl_2) and Argon (Ar) gas mixtures was used to etch the top metal layer. For TiN, 26 sccm Cl_2 flow rate, 0.6 Pa pressure, 150 Watt forward power, and 60 Watt bias power are used. SEM images of the structures are shown in Figure 5.3 (a, b). After etching, the HSQ resist layer was removed using a 3 sec dip into buffered oxide etch (BOE) solution followed by DI water rinse. The underlying PMMA layer was removed in Remover PG (or NMP) solution kept at 85^{o}C followed by a solvent cleaning in acetone and IPA. The cleaned sample was then loaded onto the LPCVD tube furnace to deposit the top Si_3N_4 layer. A cross-section SEM image of the final fabricated sample is shown in Figure 5.3 (b).

Optical Characterization:

For the optical measurements, the sample is mounted onto the rotatable stage of the VASE set – up. The monochromator source, together with a polarizer, and a retarder generate polarized light. The analyzer in the detector arm helps in distinguishing polarization components of received light. For more details on the optical measurement at high temperatures, see supplementary information.

Simulation:

The device geometries are simulated and optimized with the finite-difference time-domain (FDTD) method using the commercially available software Lumerical FDTD. Relevant geometry parameters are discussed in the main manuscript. Experimentally measured spectral dependence of complex dielectric permittivity values for TiN on MgO (bottom layer), silicon nitride (Si_3N_4)

(spacer and top cladding layers) and TiN on spacer layer (as presented in Figure 5.1) were input into the FDTD model as well and fitted using Lumerical's multi-coefficient model (MCM).

5.6 APPENDIX Supplementary Information

Section 1: High temperature optical measurements

The sample under inspection was mounted onto a heating cell (commercially available from Linkam instruments, TS1500). The cell is equipped with a ceramic heating cup with embedded electrical heating coil and is externally controlled through a temperature controller assembly. The cell was then mounted on the sample loading stage of a commercial variable angle spectroscopic ellipsometry set up (from J. A. Wollam). The assembly is shown in Figure 5.5S. The heating cell is then connected to a vacuum pump and the sample was heated under vacuum. An external water line cools the quartz window in front to minimize thermal expansion effect, especially at high temperatures. The temperature was increased with a step of 100^{o}C and we waited 10 minutes after the desired temperature was reached for stabilization of temperature. At temperatures above 800^{o}C, the ceramic heating element glows with bright red radiation which introduces additional noise as well as saturates the Si photodetector on the VASE. To work around this problem, an additional external pinhole aperture was placed in front of the detector arm of the VASE set up **(**Figure 5.5S).

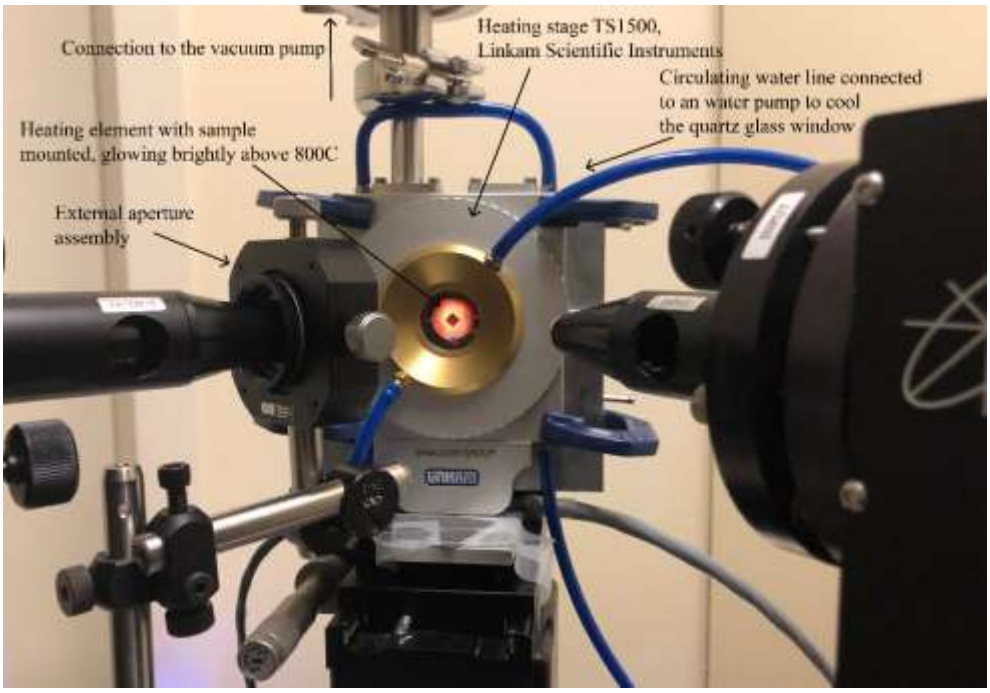

Figure 5.5S Photo of the real-life optical measurement set-up integrated with the heating stage

Section 2: Temperature dependent optical properties of Si_3N_4

Table 5.1S Variation of the ellipsometry C-L Oscillator model parameters with increasing temperature for Si_3N_4

T	Amp	E_n	B_r	E_g	E_p	E_t	E_u
23	56.64076	7.761036	0.457359	5.562586	2.967356	1.246741	0.587698
300	48.76215	7.709287	0.084777	5.333728	2.967356	1.246741	0.587698
500	47.57953	7.672107	1.00E-06	5.305233	2.967356	1.246741	0.587698
600	47.26444	7.647879	1.00E-06	5.292529	2.967356	1.246741	0.587698
700	46.89055	7.62065	1.00E-06	5.284816	2.967356	1.246741	0.587698
800	46.4615	7.604193	1.00E-06	5.2859	2.967356	1.246741	0.587698
900	46.19414	7.579885	1.00E-06	5.287852	2.967356	1.246741	0.587698

Section 3: Simulated temperature dependent response of the device

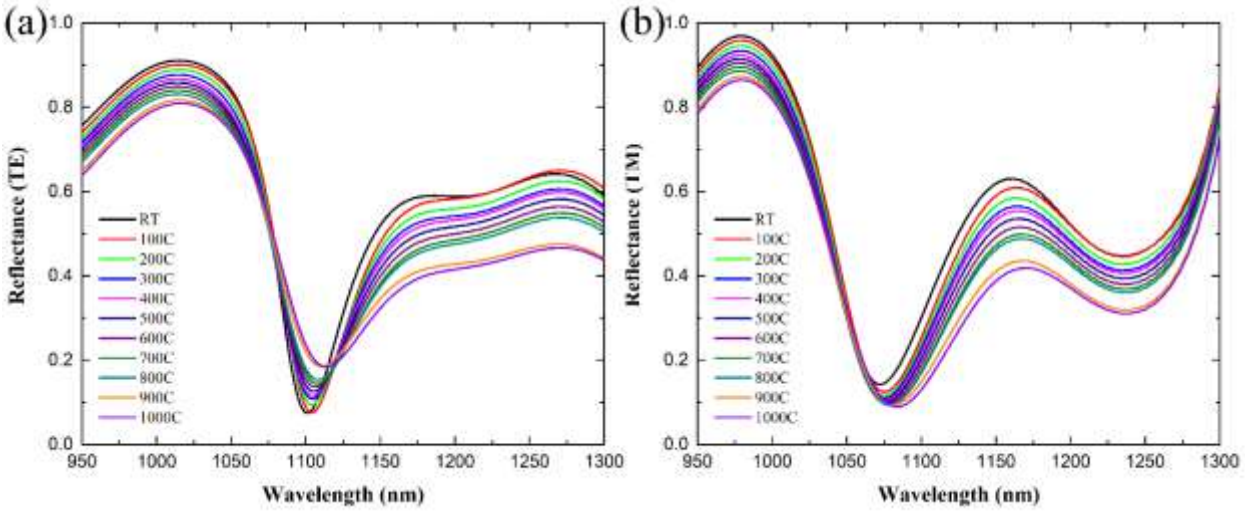

Figure 5.6S Temperature dependence of the device reflectance response for (a) TE and (b) TM polarized incidence, estimated in FDTD simulation utilizing the measured temperature dependent optical properties of the constituent layers

CHAPTER 6. HIGH Q-FACTOR ALL-DIELECTRIC METASURFACE BASED ON BOUND STATES IN THE CONTINUUM

ABSTRACT

We propose a realization of bound states in the continuum (BICs) occurring at visible optical frequencies with an all dielectric TiO_2 based metasurface device. Resonances with theoretically-infinite quality-factors can be achieved in the BIC regime and with up to a few thousand in the near-BIC.

6.1 Introduction

Metasurfaces have recently received a growing interest due to their unprecedented ability to control light using their ultrathin nanostructured subwavelength profile. Metasurfaces now find a wide variety of applications due to their versatile functionalities and more straightforward fabrication, compared to metamaterials. However, their spectral response is generally known to be broad, which hinders their applicability to devices requiring sharp spectral features. Some attempts to realize high-quality factors (Q) metasurfaces have been already reported[277,278]. The basic idea behind these realizations is to engineer the interference of two different resonances so that a Fano-type resonant mode is excited at a desired wavelength. This approach usually results in a relatively complex unit cell design[277,278].

Bound states in the continuum (BICs) were first proposed in quantum mechanics. Later, they were recognized as a general wave phenomenon that can be identified in other waves [279,280]. Realizing BIC with electromagnetic waves promise infinite Q-factors (theoretically), as then the waves are entirely decoupled from the radiation and thus are perfectly localized. BICs in photonic systems was first demonstrated in 2008 [281]. According to the Fredreich and Weightrer theory, when two resonances experience an overlap with each other while a control parameter is being continuously changed, the two channels interfere, resulting in an avoided crossing of their spectra. Typically, at a given value of the continuous parameter, one of the channels vanishes entirely and hence becomes a BIC with an infinite quality (Q) factor[282]. This effect is known as the collapse of the Fano resonance, which is a typical signature of a BIC. Although that is true that BIC states

only appear in systems with at least one dimension going to infinity, traces of these states could still be observed even in finite systems[279,283].

In this work, we introduce a metasurface design that can support very sharp resonances due to bound states in the continuum (BICs). Very high Q-factors can be achieved at or near the BIC regime with a much simpler design than coupled resonators approaches. A new design allows for downsizing the systems exhibiting BIC and for broadening their area of application. Also, the proposed design has resonances in the visible range and is polarization independent which is a unique advantage over the previously reported high-Q dielectric metasurfaces[279,284–286]. We believe that this approach will enable and augment many applications areas, e.g., sensors, spectral filters, nano-lasers, and many others by making use of such sharp resonances in a planar geometry.

6.2 Design

We make our metasurface of titanium oxide (TiO_2) nanocylinder resonators of height *h* and radius *r* arranged in a square periodic array on top of a silica substrate, as shown in the schematic of Fig. 1(a). A layer of thickness *t* with a refractive index matched to the refractive index of the substrate covers the entire structure. While different mechanisms for achieving BIC have been reported [5], in our metasurface, the interference between two resonant channels, one due to the resonance of a single nanocylinder resonator (Mie resonance) and the other due to the resonance state of the in-plane scattered light (Rayleigh scattering) creates the BIC. Figure 1(b) depicts the transmittance and reflectance spectra of the metasurface obtained from full-wave time-domain modeling. The reflectance spectra of the metasurface as a function of the nanocylinder radius indicates a complete collapse of the resonance at a radius about 99 nm (Fig. 1(b)). This effect is a signature of the BIC formation. At near-BIC regime, the field is not entirely confined. Hence, the system exhibits limited *Q*-factors. However, since BIC is a dark state, a near-BIC can be coupled directly from the air.

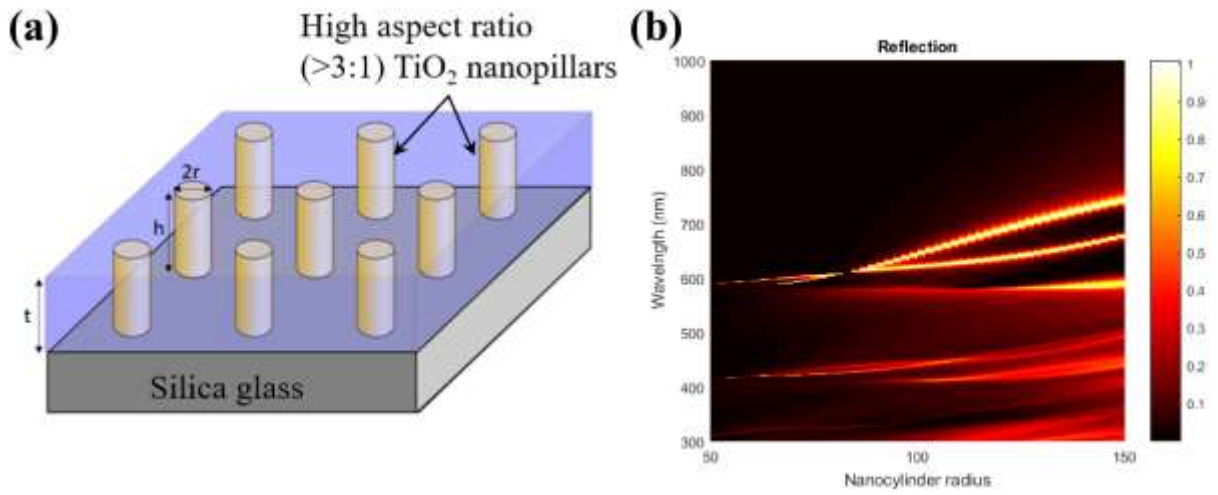

Figure 6.1 The results of FDTD simulations showing the sharp spectral resonances. (a) Metasurface design used to achieve BICs. TiO_2 nanocylinders are arranged in a square array with a period of 400 nm; (b) the scattering cross-section of a single resonator as a function of varying cylinder radii and wavelength as indicated. Colors indicate the amplitude of reflection.

6.3 Fabrication of high aspect-ratio dielectric nanostructures

Fabrication of the high aspect ratio TiO_2 nanocylinder structure require a uniquely different approach. Commonly, typical nanostructures are either created through a bottom up lift-off technique or a top down etching method. However, in most cases for high aspect ratio structures, lift-off technique starts to fail as commonly used material deposition techniques are unable to fill up uniformly, narrow trench like regions. On the other hand, for well-studied semiconductors such as crystalline silicon, or III-V materials, various dry etching techniques are well established and can be used to create tall and narrow (high aspect ratio) nano structures. However, the process becomes complicated when considering amorphous dielectrics like titanium dioxide (TiO_2) in this case. Halogenated plasma at high power is utilized for etching TiO_2, which in turn leads to poor selectivity to the mask and issues of non-uniform etching with roughened side-walls, mask-erosion are predominant. Therefore, the need for an alternative fabrication method.

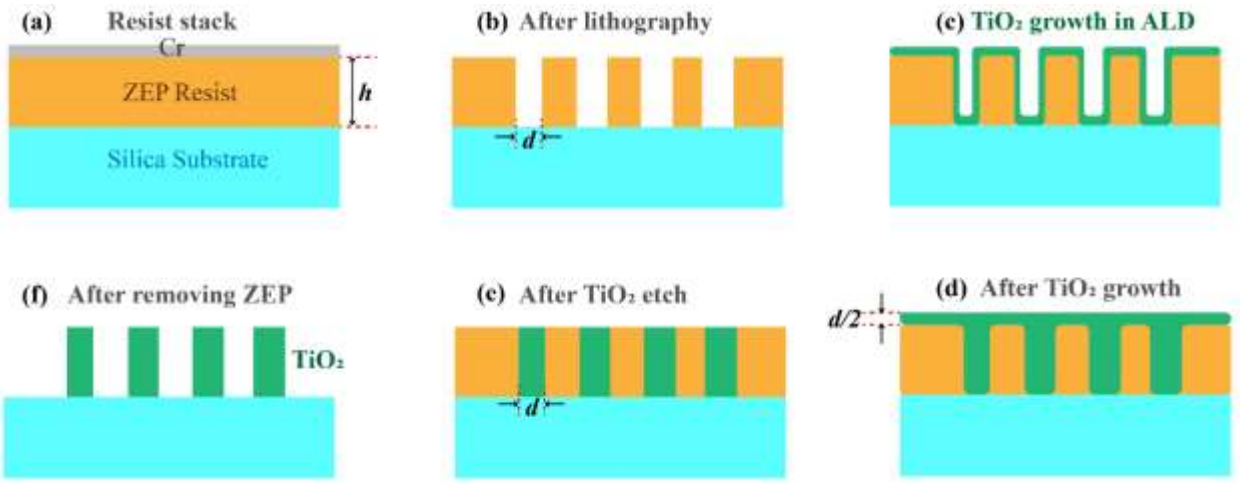

Figure 6.2 Schematic indicating different steps of the fabrication process flow sequentially from (a) through (f)

In our method, first the pattern was created on the silica substrate using a positive-tone resist (in this case ZEP 520A) using electron beam lithography. For this first the silica glass substrates (commercially available optical quality glass from PG&O) are cleaned in solvent (toluene, acetone, IPA) followed by a dehydration bake at 160^{o}C for 2-5min. At this stage, ZEP 520A electron-beam resist (commercially available from ZEON Chemicals) is spin coated onto the dry substrate and cured at 180^{o}C for 3min (Figure 6.2 (a)). The thickness of the resist should match the desired nanocylinder height. The spin process conditions are varied according to the spin-sheet to arrive at the desired thickness denoted as *h*. Before exposing the resist to electron-beam, a very thin (~5 nm) layer of Cr metal is deposited onto the resist coated substrate using e-beam deposition technique to avoid charging related writing discrepancies on dielectric substrate (Figure 6.2 (a)). Following the deposition, the sample is immediately loaded onto the load lock of the electron beam lithography (EBL) instrument to prevent further oxidation of the Cr thin film. After electron beam exposure, first Cr layer is etched away using Cr-16 chromium etchant solution and followed by a DI rinse. Next, the resist was developed in ZDMAC developer for 90 seconds and rinsed in IPA. Some un-developed residual resist may remain at the bottom of the narrow cylinder holes which are then cleaned off by ashing the resist in a barrel etcher in O2 plasma (at 100W, 1.2T) for 1 min. This may lead to some reduction of the resist thickness from top down etching as well as increase in diameter of the cylinders. Initial resist thickness and written diameter

of the cylinders can be adjusted to account for this step. At this point the sample should have an array of cylindrical holes in the resist (Figure 6.2 (b)).

Next, the sample is loaded onto an atomic layer deposition (ALD) tool for growth of the TiO_2. ALD allows for uniform and highly conformal, layer by layer growth and therefore ensures completely coverage of the all the holes (Figure 6.2 (c)). The TiO_2 thickness is decided by the maximum diameter of the cylinders (*d*) on the sample. Due to conformal growth from all sides thickness of *d/2* would be enough to fill the cylinders (Figure 6.2 (d)). However, we keep a margin of growing an additional 10-15 nm. In order to ensure stability of the polymer based resist, the ALD operating temperature is kept much below the resist curing temperature, in this case at an 120^{o}C. A low growth rate of 0.6 nm/cycle is achieved in this low temperature process. In addition, other process parameters such as precursor and water pulse times, purge times, pressure etc. are also optimized to arrive at reasonably good optical quality of the grown TiO_2 film. At this stage, TiO_2 covers not only the cylinder holes but also the top surface of the resist. To planarize the top surface and also to expose the resist layer from top, at this step, the excess TiO_2 cover is etched away using a plasma RIE technique. A combination of BCl_3, Cl_2 and Ar gas chemistry is used at 650W RF power, 80W bias power and 0.8T pressure (Figure 6.2 (e)).

The remaining resist matrix can then be removed in NMP (N-Methyl Pyrolidine, aka Remover PG) heated at 120^{o}C followed by rinsing the sample in acetone and IPA. This concludes the fabrication of the high aspect ratio (Figure 6.2 (f)).

6.4 Experimental Results

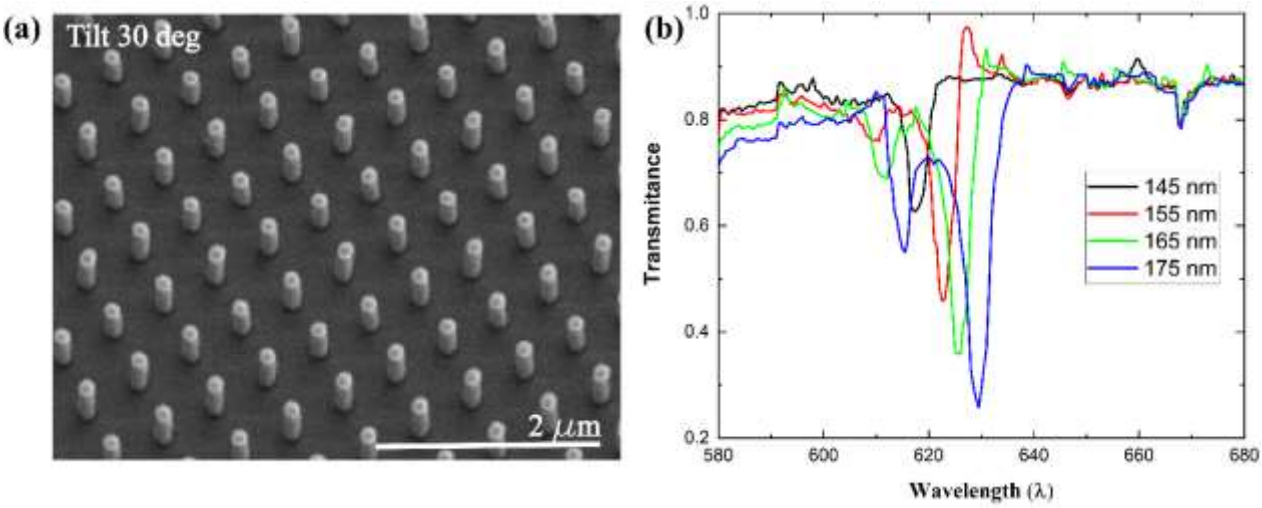

Figure 6.3 (a) An scanning electron microscope of the fabricated metasurface (after resist removal) taken at a tilt of 30°, (b) the measured transmission spectra (at normal incidence) from the metasurface (with resist cover) with different diameters of the TiO_2 nanocylinders as indicated.

The fabricated devices are first characterized by measuring the transmission spectra at normal incidence for both (TE and TM polarizations). These transmission measurements were performed using a commercially available spectroscopic ellipsometry set-up after the TiO_2 etching but before the removal of resist. The resist polymer has a refractive index of 1.54 and therefore fulfils the index matching condition to the substrate. The measured transmission spectra capture the sharp resonance peaks and also matched beautifully the trend observed in numerical simulation. With increasing diameter of the cylinders the resonance splits into two arms as seen in Figure 6.1 (b) for radii range of 60 -100 nm. The sharp resonances with FWHM of the order of 5nm (for diameter 175 nm) are signatures of the near BIC states.

6.5 Conclusion

In this work, we have experimentally demonstrated the formation of BIC in visible optical frequencies in an all dielectric based metasurface device. High aspect ratio TiO_2 nanostructure array is created using a unique fabrication method and the devices are characterized for different geometries as well. The device also exhibits exquisite physical processes including the formation of localized states with infinite lifetimes manifested into sharp and narrow resonances, and strong

coupling of Fano and Mie type resonating modes. This first demonstration of a metasurface BIC at visible spectral window would be highly suitable for applications in sensing, low threshold lasing, and high efficiency nonlinear optics.

REFERENCES

(1) Linden, S.; Enkrich, C.; Wegener, M.; Zhou, J.; Koschny, T.; Soukoulis, C. M. Controlling Electromagnetic Fields. *Science (80-.).* **2004**, *306* (5700), 1351–1353. https://doi.org/10.1126/science.1125907.

(2) Veselago, V. G. THE ELECTRODYNAMICS OF SUBSTANCES WITH SIMULTANEOUSLY NEGATIVE VALUES OF ϵ AND μ. *Sov. Phys. Uspekhi* **1968**, *10* (4), 509–514. https://doi.org/10.1070/PU1968v010n04ABEH003699.

(3) Soukoulis, C. M.; Wegener, M. Optical Metamaterials--More Bulky and Less Lossy. *Science (80-.).* **2010**, *330* (6011), 1633–1634. https://doi.org/10.1126/science.1198858.

(4) Shalaev, V. M.; Cai, W.; Chettiar, U. K.; Yuan, H.-K.; Sarychev, A. K.; Drachev, V. P.; Kildishev, A. V. Negative Index of Refraction in Optical Metamaterials. *Opt. Lett.* **2005**, *30* (24), 3356. https://doi.org/10.1364/OL.30.003356.

(5) Shelby, R. A.; Smith, D. R.; Schultz, S. Experimental Verification of a Negative Index of Refraction. *Science* **2001**, *292* (5514), 77–79. https://doi.org/10.1126/science.1058847.

(6) Zhang, S.; Fan, W.; Panoiu, N. C.; Malloy, K. J.; Osgood, R. M.; Brueck, S. R. J. Experimental Demonstration of Near-Infrared Negative-Index Metamaterials. *Phys. Rev. Lett.* **2005**, *95* (13), 137404. https://doi.org/10.1103/PhysRevLett.95.137404.

(7) Pendry, J. B. Negative Refraction Makes a Perfect Lens. *Phys. Rev. Lett.* **2000**, *85* (18), 3966–3969. https://doi.org/10.1103/PhysRevLett.85.3966.

(8) Schurig, D.; Mock, J. J.; Justice, B. J.; Cummer, S. A.; Pendry, J. B.; Starr, A. F.; Smith, D. R. Metamaterial Electromagnetic Cloak at Microwave Frequencies. *Science* **2006**, *314* (5801), 977–980. https://doi.org/10.1126/science.1133628.

(9) Cai, W.; Chettiar, U. K.; Kildishev, A. V.; Shalaev, V. M. Optical Cloaking with Metamaterials. *Nat. Photonics* **2007**, *1* (4), 224–227. https://doi.org/10.1038/nphoton.2007.28.

(10) Genov, D. A.; Zhang, S.; Zhang, X. Mimicking Celestial Mechanics in Metamaterials. *Nat. Phys.* **2009**, *5* (9), 687–692. https://doi.org/10.1038/nphys1338.

(11) Narimanov, E. E.; Kildishev, A. V. Optical Black Hole: Broadband Omnidirectional Light Absorber. *Appl. Phys. Lett.* **2009**, *95* (4), 041106. https://doi.org/10.1063/1.3184594.

(12) Mello, O. L.; Li, Y.; Camayd-Munoz, P.; Chia, C.; Huang, I.-C.; Lončar, M.; Mazur, E.; Mazur, E. Strongly Extended Superradiance in Diamond Metamaterials. In *Conference on Lasers and Electro-Optics*; OSA: Washington, D.C., 2017; p JTu5A.26. https://doi.org/10.1364/CLEO_AT.2017.JTu5A.26.

(13) Vlasova, D. D.; Kalachev, A. A. Optical Superradiance on Cooperative Transitions in Metamaterials. *Bull. Russ. Acad. Sci. Phys.* **2012**, *76* (3), 256–259. https://doi.org/10.3103/S1062873812030409.

(14) Jacob, Z.; Kim, J.-Y.; Naik, G. V.; Boltasseva, A.; Narimanov, E. E.; Shalaev, V. M. Engineering Photonic Density of States Using Metamaterials. *Appl. Phys. B* **2010**, *100* (1), 215–218. https://doi.org/10.1007/s00340-010-4096-5.

(15) Poddubny, A.; Iorsh, I.; Belov, P.; Kivshar, Y. Hyperbolic Metamaterials. *Nat. Photonics* **2013**, *7* (12), 948–957. https://doi.org/10.1038/nphoton.2013.243.

(16) Drachev, V. P.; Podolskiy, V. A.; Kildishev, A. V. Hyperbolic Metamaterials: New Physics behind a Classical Problem. *Opt. Express* **2013**, *21* (12), 15048. https://doi.org/10.1364/OE.21.015048.

(17) Yu, N.; Genevet, P.; Kats, M. A.; Aieta, F.; Tetienne, J.-P.; Capasso, F.; Gaburro, Z. Light Propagation with Phase Discontinuities: Generalized Laws of Reflection and Refraction. *Science (80-.).* **2011**, *334* (6054), 333–337. https://doi.org/10.1126/science.1210713.

(18) Maier, S. A. *Plasmonics: Fundamentals and Applications*; Springer US: Boston, MA, 2007. https://doi.org/10.1007/0-387-37825-1.

(19) Gramotnev, D. K.; Bozhevolnyi, S. I. Plasmonics beyond the Diffraction Limit. *Nat Phot.* **2010**, *4* (2), 83–91. https://doi.org/10.1038/nphoton.2009.282.

(20) Schuller, J. A.; Barnard, E. S.; Cai, W.; Jun, Y. C.; White, J. S.; Brongersma, M. L. Plasmonics for Extreme Light Concentration and Manipulation. *Nat Mater* **2010**, *9* (3), 193–204.

(21) González, A. L.; Noguez, C.; Beránek, J.; Barnard, A. S. Size, Shape, Stability, and Color of Plasmonic Silver Nanoparticles. *J. Phys. Chem. C* **2014**, *118* (17), 9128–9136. https://doi.org/10.1021/jp5018168.

(22) Sepúlveda, B.; Alaverdyan, Y.; Alegret, 3# J; Käll, M.; Johansson, P. Shape Effects in the Localized Surface Plasmon Resonance of Single Nanoholes in Thin Metal Films. *Nat. Phys. J. Phys. Chem. C J. Phys. Chem. B J. Phys. Chem. B Phys. Rev. E Math. Methods Phys. P. B. Johnson R. W. Christy Phys. Rev. B* **2007**, *79* (23), 1267–1290.

(23) Visser, H. J. *Array and Phased Array Antenna Basics*; John Wiley & Sons, Ltd: Chichester, UK, 2005. https://doi.org/10.1002/0470871199.

(24) Munk, B. A. *Frequency Selective Surfaces*; John Wiley & Sons, Inc.: Hoboken, NJ, USA, 2000. https://doi.org/10.1002/0471723770.

(25) Ryan, C. G. M.; Chaharmir, M. R.; Shaker, J.; Bray, J. R.; Antar, Y. M. M.; Ittipiboon, A. A Wideband Transmitarray Using Dual-Resonant Double Square Rings. *IEEE Trans. Antennas Propag.* **2010**, *58* (5), 1486–1493. https://doi.org/10.1109/TAP.2010.2044356.

(26) Sazegar, M.; Zheng, Y.; Kohler, C.; Maune, H.; Nikfalazar, M.; Binder, J. R.; Jakoby, R. Beam Steering Transmitarray Using Tunable Frequency Selective Surface With Integrated Ferroelectric Varactors. *IEEE Trans. Antennas Propag.* **2012**, *60* (12), 5690–5699. https://doi.org/10.1109/TAP.2012.2213057.

(27) Pozar, D. M.; Targonski, S. D.; Syrigos, H. D. Design of Millimeter Wave Microstrip Reflectarrays. *IEEE Trans. Antennas Propag.* **1997**, *45* (2), 287–296. https://doi.org/10.1109/8.560348.

(28) Costa, F.; Monorchio, A.; Manara, G. Analysis and Design of Ultra Thin Electromagnetic Absorbers Comprising Resistively Loaded High Impedance Surfaces. *IEEE Trans. Antennas Propag.* **2010**, *58* (5), 1551–1558. https://doi.org/10.1109/TAP.2010.2044329.

(29) Sun, S.; Yang, K.; Wang, C.; Juan, T.; Chen, W. T.; Liao, C. Y.; He, Q.; Xiao, S.; Kung, W.; Guo, G.; et al. High-Efficiency Broadband Anomalous Reflection by Gradient Meta-Surfaces. *Nano Lett.* **2012**, *12* (12), 6223–6229. https://doi.org/10.1021/nl3032668.

(30) Zhao, Y.; Alù, A. Manipulating Light Polarization with Ultrathin Plasmonic Metasurfaces. *Phys. Rev. B - Condens. Matter Mater. Phys.* **2011**, *84*, 1–6. https://doi.org/10.1103/PhysRevB.84.205428.

(31) Ni, X.; Emani, N. K.; Kildishev, a. V.; Boltasseva, A.; Shalaev, V. M. Broadband Light Bending with Plasmonic Nanoantennas. *Science (80-.).* **2012**, *335* (6067), 427–427. https://doi.org/10.1126/science.1214686.

(32) Xu, T.; Du, C.; Wang, C.; Luo, X. Subwavelength Imaging by Metallic Slab Lens with Nanoslits. *Appl. Phys. Lett.* **2007**, *91* (20), 201501. https://doi.org/10.1063/1.2811711.

(33) Ni, X.; Ishii, S.; Kildishev, A. V; Shalaev, V. M. Ultra-Thin, Planar, Babinet-Inverted Plasmonic Metalenses. *Light Sci. Appl.* **2013**, *2* (4), e72. https://doi.org/10.1038/lsa.2013.28.

(34) Aieta, F.; Genevet, P.; Kats, M. A.; Yu, N.; Blanchard, R.; Gaburro, Z.; Capasso, F. Aberration-Free Ultrathin Flat Lenses and Axicons at Telecom Wavelengths Based on Plasmonic Metasurfaces. *Nano Lett.* **2012**, *12* (9), 4932–4936. https://doi.org/10.1021/nl302516v.

(35) Khorasaninejad, M.; Chen, W. T.; Devlin, R. C.; Oh, J.; Zhu, A. Y.; Capasso, F. Metalenses at Visible Wavelengths: Diffraction-Limited Focusing and Subwavelength Resolution Imaging. *Science (80-.).* **2016**, *352* (6290), 1190–1194. https://doi.org/10.1126/science.aaf6644.

(36) Ding, F.; Wang, Z.; He, S.; Shalaev, V. M.; Kildishev, A. V. Broadband High-Efficiency Half-Wave Plate: A Supercell-Based Plasmonic Metasurface Approach. *ACS Nano* **2015**, *9* (4), 4111–4119. https://doi.org/10.1021/acsnano.5b00218.

(37) Pors, A.; Bozhevolnyi, S. I. Efficient and Broadband Quarter-Wave Plates by Gap-Plasmon Resonators. *Opt. Express* **2013**, *21* (3), 2942. https://doi.org/10.1364/OE.21.002942.

(38) Yu, N.; Aieta, F.; Genevet, P.; Kats, M. A.; Gaburro, Z.; Capasso, F. A Broadband, Background-Free Quarter-Wave Plate Based on Plasmonic Metasurfaces. *Nano Lett.* **2012**, *12* (12), 6328–6333. https://doi.org/10.1021/nl303445u.

(39) Chen, W. T.; Yang, K. Y.; Wang, C. M.; Huang, Y. W.; Sun, G.; Chiang, I. Da; Liao, C. Y.; Hsu, W. L.; Lin, H. T.; Sun, S.; et al. High-Efficiency Broadband Meta-Hologram with Polarization-Controlled Dual Images. *Nano Lett.* **2014**, *14* (1), 225–230. https://doi.org/10.1021/nl403811d.

(40) Wen, D.; Yue, F.; Li, G.; Zheng, G.; Chan, K.; Chen, S.; Chen, M.; Li, K. F.; Wong, P. W. H.; Cheah, K. W.; et al. Helicity Multiplexed Broadband Metasurface Holograms. *Nat. Commun.* **2015**, *6*, 8241. https://doi.org/10.1038/ncomms9241.

(41) Huang, L.; Chen, X.; Mühlenbernd, H.; Zhang, H.; Chen, S.; Bai, B.; Tan, Q.; Jin, G.; Cheah, K.-W.; Qiu, C.-W.; et al. Three-Dimensional Optical Holography Using a Plasmonic Metasurface. *Nat. Commun.* **2013**, *4* (1), 2808. https://doi.org/10.1038/ncomms3808.

(42) Li, X.; Chen, L.; Li, Y.; Zhang, X.; Pu, M.; Zhao, Z.; Ma, X.; Wang, Y.; Hong, M.; Luo, X. Multicolor 3D Meta-Holography by Broadband Plasmonic Modulation. *Sci. Adv.* **2016**, *2* (11), e1601102–e1601102. https://doi.org/10.1126/sciadv.1601102.

(43) Li, Z.; Palacios, E.; Butun, S.; Aydin, K. Visible-Frequency Metasurfaces for Broadband Anomalous Reflection and High-Efficiency Spectrum Splitting. *Nano Lett.* **2015**, *15* (3), 1615–1621. https://doi.org/10.1021/nl5041572.

(44) Yang, Y.; Wang, W.; Moitra, P.; Kravchenko, I. I.; Briggs, D. P.; Valentine, J. Dielectric Meta-Reflectarray for Broadband Linear Polarization Conversion and Optical Vortex Generation. *Nano Lett.* **2014**, *14* (3), 1394–1399. https://doi.org/10.1021/nl4044482.

(45) Kim, J.; Choudhury, S.; DeVault, C.; Zhao, Y.; Kildishev, A. V.; Shalaev, V. M.; Alù, A.; Boltasseva, A. Controlling the Polarization State of Light with Plasmonic Metal Oxide Metasurface. *ACS Nano* **2016**, *10* (10), 9326–9333. https://doi.org/10.1021/acsnano.6b03937.

(46) Khurgin, J. B. How to Deal with the Loss in Plasmonics and Metamaterials. *Nat Nano* **2015**, *10* (1), 2–6.

(47) Ding, F.; Dai, J.; Chen, Y.; Zhu, J.; Jin, Y.; Bozhevolnyi, S. I. Broadband Near-Infrared Metamaterial Absorbers Utilizing Highly Lossy Metals. *Sci. Rep.* **2016**, *6* (1), 39445. https://doi.org/10.1038/srep39445.

(48) Guler, U.; Ndukaife, J. C.; Naik, G. V; Nnanna, A. G. A.; Kildishev, A. V; Shalaev, V. M.; Boltasseva, A. Local Heating with Lithographically Fabricated Plasmonic Titanium Nitride Nanoparticles. *Nano Lett.* **2013**, *13* (12), 6078–6083. https://doi.org/10.1021/nl4033457.

(49) Khurgin, J. B.; Boltasseva, A. Reflecting upon the Losses in Plasmonics and Metamaterials. *MRS Bull.* **2012**, *37* (08), 768–779. https://doi.org/10.1557/mrs.2012.173.

(50) Gomez-Diaz, J. S.; Lee, J.; Tymchenko, M.; Belkin, M. A.; Alu, A. Giant Nonlinear Processes in Plasmonic Metasurfaces. In *2015 IEEE International Symposium on Antennas and Propagation & USNC/URSI National Radio Science Meeting*; IEEE, 2015; pp 1084–1085. https://doi.org/10.1109/APS.2015.7304930.

(51) Kruk, S.; Weismann, M.; Bykov, A. Y.; Mamonov, E. A.; Kolmychek, I. A.; Murzina, T.; Panoiu, N. C.; Neshev, D. N.; Kivshar, Y. S. Enhanced Magnetic Second-Harmonic Generation from Resonant Metasurfaces. *ACS Photonics* **2015**, *2* (8), 1007–1012. https://doi.org/10.1021/acsphotonics.5b00215.

(52) Mamonov, E.; Kolmychek, I.; Maydykovsky, A.; Murzina, T. Second Harmonic Generation in Planar Chiral Nanostructures. *Bull. Russ. Acad. Sci.* **2013**, *77* (1).

(53) Chandrasekar, R.; Emani, N. K.; Lagutchev, A.; Shalaev, V. M.; Ciracì, C.; Smith, D. R.; Kildishev, A. V. Second Harmonic Generation with Plasmonic Metasurfaces: Direct Comparison of Electric and Magnetic Resonances. *Opt. Mater. Express* **2015**, *5* (11), 2682. https://doi.org/10.1364/OME.5.002682.

(54) Panchenko, E.; Cadusch, J. J.; James, T. D.; Roberts, A. Plasmonic Metasurface-Enabled Differential Photodetectors for Broadband Optical Polarization Characterization. *ACS Photonics* **2016**, *3* (10), 1833–1839. https://doi.org/10.1021/acsphotonics.6b00342.

(55) Fang, J.; Wang, D.; DeVault, C. T.; Chung, T.-F.; Chen, Y. P.; Boltasseva, A.; Shalaev, V. M.; Kildishev, A. V. Enhanced Graphene Photodetector with Fractal Metasurface. *Nano Lett.* **2017**, *17* (1), 57–62. https://doi.org/10.1021/acs.nanolett.6b03202.

(56) Yokogawa, S.; Burgos, S. P.; Atwater, H. A. Plasmonic Color Filters for CMOS Image Sensor Applications. *Nano Lett.* **2012**, *12* (8), 4349–4354. https://doi.org/10.1021/nl302110z.

(57) Roberts, A. S.; Pors, A.; Albrektsen, O.; Bozhevolnyi, S. I. Subwavelength Plasmonic Color Printing Protected for Ambient Use. *Nano Lett.* **2014**, *14* (2), 783–787. https://doi.org/10.1021/nl404129n.

(58) Luk, T. S.; Campione, S.; Kim, I.; Feng, S.; Jun, Y. C.; Liu, S.; Wright, J. B.; Brener, I.; Catrysse, P. B.; Fan, S.; et al. Directional Perfect Absorption Using Deep Subwavelength Low-Permittivity Films. *Phys. Rev. B* **2014**, *90* (8), 085411. https://doi.org/10.1103/PhysRevB.90.085411.

(59) Aydin, K.; Ferry, V. E.; Briggs, R. M.; Atwater, H. A. Broadband Polarization-Independent Resonant Light Absorption Using Ultrathin Plasmonic Super Absorbers. *Nat. Commun.* **2011**, *2*, 517. https://doi.org/10.1038/ncomms1528.

(60) Jiang, Z. H.; Yun, S.; Toor, F.; Werner, D. H.; Mayer, T. S. Conformal Dual-Band Near-Perfectly Absorbing Mid-Infrared Metamaterial Coating. *ACS Nano* **2011**, *5* (6), 4641–4647. https://doi.org/10.1021/nn2004603.

(61) Argyropoulos, C.; Le, K. Q.; Mattiucci, N.; D'Aguanno, G.; Alù, A. Broadband Absorbers and Selective Emitters Based on Plasmonic Brewster Metasurfaces. *Phys. Rev. B* **2013**, *87* (20), 205112. https://doi.org/10.1103/PhysRevB.87.205112.

(62) Naldoni, A.; Guler, U.; Wang, Z.; Marelli, M.; Malara, F.; Meng, X.; Besteiro, L. V.; Govorov, A. O.; Kildishev, A. V.; Boltasseva, A.; et al. Broadband Hot-Electron Collection for Solar Water Splitting with Plasmonic Titanium Nitride. *Adv. Opt. Mater.* **2017**, *5* (15), 1601031. https://doi.org/10.1002/adom.201601031.

(63) Guler, U.; Shalaev, V. M.; Boltasseva, A. Nanoparticle Plasmonics: Going Practical with Transition Metal Nitrides. **2015**, *18* (4), 227–237. https://doi.org/10.1016/j.mattod.2014.10.039.

(64) Zhou, N.; Xu, X.; Hammack, A. T.; Stipe, B. C.; Gao, K.; Scholz, W.; Gage, E. C. Plasmonic Near-Field Transducer for Heat-Assisted Magnetic Recording. *Nanophotonics* **2014**, *3* (3), 141–155. https://doi.org/10.1515/nanoph-2014-0001.

(65) Reddy, H.; Guler, U.; Chaudhuri, K.; Dutta, A.; Kildishev, A. V.; Shalaev, V. M.; Boltasseva, A. Temperature-Dependent Optical Properties of Single Crystalline and Polycrystalline Silver Thin Films. *ACS Photonics* **2017**, *4* (5), 1083–1091. https://doi.org/10.1021/acsphotonics.6b00886.

(66) Reddy, H.; Guler, U.; Kildishev, A. V.; Boltasseva, A.; Shalaev, V. M. Temperature-Dependent Optical Properties of Gold Thin Films. *Opt. Mater. Express* **2016**, *6* (9), 2776. https://doi.org/10.1364/OME.6.002776.

(67) Li, W.; Guler, U.; Kinsey, N.; Naik, G. V.; Boltasseva, A.; Guan, J.; Shalaev, V. M.; Kildishev, A. V. Refractory Plasmonics with Titanium Nitride: Broadband Metamaterial Absorber. *Adv. Mater.* **2014**, *26* (47), 7959–7965. https://doi.org/10.1002/adma.201401874.

(68) Huang, Y.; Wai, H.; Lee, H.; Sokhoyan, R. Gate-Tunable Conducting Oxide Metasurfaces. **2015**, 1–13.

(69) Ndukaife, J. C.; Kildishev, A. V; Nnanna, A. G. A.; Shalaev, V. M.; Wereley, S. T.; Boltasseva, A. Long-Range and Rapid Transport of Individual Nano-Objects by a Hybrid Electrothermoplasmonic Nanotweezer. *Nat Nano* **2016**, *11* (1), 53–59.

(70) Naik, G. V.; Shalaev, V. M.; Boltasseva, A. Alternative Plasmonic Materials: Beyond Gold and Silver. *Adv. Mater.* **2013**, *25* (24), 3264–3294. https://doi.org/10.1002/adma.201205076.

(71) Guler, U.; Boltasseva, A.; Shalaev, V. M. Refractory Plasmonics. *Science (80-.).* **2014**, *344* (6181), 263–264. https://doi.org/10.1126/science.1252722.

(72) Naik, G. V.; Kim, J.; Boltasseva, A. Oxides and Nitrides as Alternative Plasmonic Materials in the Optical Range. *Opt. Mater. Express* **2011**, *1* (6), 1090–1099. https://doi.org/10.1103/PhysRevLett.107.133901.

(73) Kim, J.; Naik, G. V.; Gavrilenko, A. V.; Dondapati, K.; Gavrilenko, V. I.; Prokes, S. M.; Glembocki, O. J.; Shalaev, V. M.; Boltasseva, A. Optical Properties of Gallium-Doped Zinc Oxide-a Low-Loss Plasmonic Material: First-Principles Theory and Experiment. *Phys. Rev. X* **2014**, *3* (4), 1–9. https://doi.org/10.1103/PhysRevX.3.041037.

(74) Wang, Y.; Capretti, A.; Dal Negro, L. Wide Tuning of the Optical and Structural Properties of Alternative Plasmonic Materials. *Opt. Mater. Express* **2015**, *5* (11), 2415. https://doi.org/10.1364/OME.5.002415.

(75) Kinsey, N.; DeVault, C.; Kim, J.; Ferrera, M.; Shalaev, V. M.; Boltasseva, A. Epsilon-near-Zero Al-Doped ZnO for Ultrafast Switching at Telecom Wavelengths. *Optica* **2015**, *2* (7), 616–622. https://doi.org/10.1364/OPTICA.2.000616.

(76) Park, J.; Kang, J.-H.; Liu, X.; Brongersma, M. L. Electrically Tunable Epsilon-Near-Zero (ENZ) Metafilm Absorbers. *Sci. Rep.* **2015**, *5* (Mim), 15754. https://doi.org/10.1038/srep15754.

(77) Naguib, M.; Mochalin, V. N.; Barsoum, M. W.; Gogotsi, Y. 25th Anniversary Article: MXenes: A New Family of Two-Dimensional Materials. *Adv. Mater.* **2014**, *26* (7), 992–1005. https://doi.org/10.1002/adma.201304138.

(78) Alhabeb, M.; Maleski, K.; Anasori, B.; Lelyukh, P.; Clark, L.; Sin, S.; Gogotsi, Y. Guidelines for Synthesis and Processing of Two-Dimensional Titanium Carbide (Ti 3 C 2 T x MXene). *Chem. Mater.* **2017**, *29* (18), 7633–7644. https://doi.org/10.1021/acs.chemmater.7b02847.

(79) Dillon, A. D.; Ghidiu, M. J.; Krick, A. L.; Griggs, J.; May, S. J.; Gogotsi, Y.; Barsoum, M. W.; Fafarman, A. T. Highly Conductive Optical Quality Solution-Processed Films of 2D Titanium Carbide. *Adv. Funct. Mater.* **2016**, *26* (23), 4162–4168. https://doi.org/10.1002/adfm.201600357.

(80) Lukatskaya, M. R.; Mashtalir, O.; Ren, C. E.; Dall'Agnese, Y.; Rozier, P.; Taberna, P. L.; Naguib, M.; Simon, P.; Barsoum, M. W.; Gogotsi, Y. Cation Intercalation and High Volumetric Capacitance of Two-Dimensional Titanium Carbide. *Science (80-.).* **2013**, *341* (6153), 1502–1505. https://doi.org/10.1126/science.1241488.

(81) Yin, X.; Ye, Z.; Rho, J.; Wang, Y.; Zhang, X. Photonic Spin Hall Effect at Metasurfaces. *Science (80-.).* **2013**, *339* (6126), 1405–1407. https://doi.org/10.1126/science.1231758.

(82) Novoselov, K. S.; Jiang, D.; Schedin, F.; Booth, T. J.; Khotkevich, V. V; Morozov, S. V; Geim, A. K. Two-Dimensional Atomic Crystals. *Proc. Natl. Acad. Sci. U. S. A.* **2005**, *102* (30), 10451–10453. https://doi.org/10.1073/pnas.0502848102.

(83) Manzeli, S.; Ovchinnikov, D.; Pasquier, D.; Yazyev, O. V.; Kis, A. 2D Transition Metal Dichalcogenides. *Nat. Rev. Mater.* **2017**, *2* (8), 17033. https://doi.org/10.1038/natrevmats.2017.33.

(84) Xia, F.; Wang, H.; Jia, Y. Rediscovering Black Phosphorus as an Anisotropic Layered Material for Optoelectronics and Electronics. *Nat. Commun.* **2014**, *5*, 4458. https://doi.org/10.1038/ncomms5458.

(85) Koppens, F. H. L.; Chang, D. E.; García de Abajo, F. J. Graphene Plasmonics: A Platform for Strong Light-Matter Interactions. *Nano Lett.* **2011**, *11* (8), 3370–3377. https://doi.org/10.1021/nl201771h.

(86) Fiori, G.; Bonaccorso, F.; Iannaccone, G.; Palacios, T.; Neumaier, D.; Seabaugh, A.; Banerjee, S. K.; Colombo, L. Electronics Based on Two-Dimensional Materials. *Nat. Nanotechnol.* **2014**, *9* (10), 768–779. https://doi.org/10.1038/nnano.2014.207.

(87) Xia, F.; Wang, H.; Xiao, D.; Dubey, M.; Ramasubramaniam, A. Two-Dimensional Material Nanophotonics. *Nat Phot.* **2014**, *8* (12), 899–907. https://doi.org/10.1038/nphoton.2014.271.

(88) Geim, A. K.; Novoselov, K. S. The Rise of Graphene. *Nat. Mater.* **2007**, *6* (3), 183–191. https://doi.org/10.1038/nmat1849.

(89) Wallace, P. R. The Band Theory of Graphite. *Phys. Rev.* **1947**, *71* (9), 622–634. https://doi.org/10.1103/PhysRev.71.622.

(90) Fei, Z.; Rodin, A. S.; Andreev, G. O.; Bao, W.; McLeod, A. S.; Wagner, M.; Zhang, L. M.; Zhao, Z.; Thiemens, M.; Dominguez, G.; et al. Gate-Tuning of Graphene Plasmons Revealed by Infrared Nano-Imaging. *Nature* **2012**, *487* (7405), 1–9. https://doi.org/10.1038/nature11253.

(91) Pirruccio, G.; Martín Moreno, L.; Lozano, G.; Gómez Rivas, J. Coherent and Broadband Enhanced Optical Absorption in Graphene. *ACS Nano* **2013**, *7* (6), 4810–4817. https://doi.org/10.1021/nn4012253.

(92) Sun, Z.; Hasan, T.; Torrisi, F.; Popa, D.; Privitera, G.; Wang, F.; Bonaccorso, F.; Basko, D. M.; Ferrari, A. C. Graphene Mode-Locked Ultrafast Laser. *ACS Nano* **2010**, *4* (2), 803–810. https://doi.org/10.1021/nn901703e.

(93) Kim, Y. D.; Kim, H.; Cho, Y.; Ryoo, J. H.; Park, C.-H.; Kim, P.; Kim, Y. S.; Lee, S.; Li, Y.; Park, S.-N.; et al. Bright Visible Light Emission from Graphene. *Nat. Nanotechnol.* **2015**, *10* (8), 676–681. https://doi.org/10.1038/nnano.2015.118.

(94) Lui, C. H.; Mak, K. F.; Shan, J.; Heinz, T. F. Ultrafast Photoluminescence from Graphene. *Phys. Rev. Lett.* **2010**, *105* (12), 127404. https://doi.org/10.1103/PhysRevLett.105.127404.

(95) Nair, R. R.; Blake, P.; Grigorenko, A. N.; Novoselov, K. S.; Booth, T. J.; Stauber, T.; Peres, N. M. R.; Geim, A. K. Fine Structure Constant Defines Visual Transparency of Graphene. *Science (80-.).* **2008**, *320* (5881), 1308–1308. https://doi.org/10.1126/science.1156965.

(96) Blake, P.; Hill, E. W.; Castro Neto, A. H.; Novoselov, K. S.; Jiang, D.; Yang, R.; Booth, T. J.; Geim, A. K. Making Graphene Visible. *Appl. Phys. Lett.* **2007**, *91* (6), 063124. https://doi.org/10.1063/1.2768624.

(97) Xiao, D.; Liu, G.-B.; Feng, W.; Xu, X.; Yao, W. Coupled Spin and Valley Physics in Monolayers of MoS2 and Other Group-VI Dichalcogenides. *Phys. Rev. Lett.* **2012**, *108* (19), 196802. https://doi.org/10.1103/PhysRevLett.108.196802.

(98) Yu, H.; Liu, G.-B.; Gong, P.; Xu, X.; Yao, W. Dirac Cones and Dirac Saddle Points of Bright Excitons in Monolayer Transition Metal Dichalcogenides. *Nat. Commun.* **2014**, *5* (May), 3876. https://doi.org/10.1038/ncomms4876.

(99) Berkelbach, T. C.; Hybertsen, M. S.; Reichman, D. R. Theory of Neutral and Charged Excitons in Monolayer Transition Metal Dichalcogenides. *Phys. Rev. B* **2013**, *88* (4), 045318. https://doi.org/10.1103/PhysRevB.88.045318.

(100) Rodin, A. S.; Carvalho, A.; Castro Neto, A. H. Excitons in Anisotropic Two-Dimensional Semiconducting Crystals. *Phys. Rev. B* **2014**, *90* (7), 1–7. https://doi.org/10.1103/PhysRevB.90.075429.

(101) Mak, K. F.; He, K.; Shan, J.; Heinz, T. F. Control of Valley Polarization in Monolayer MoS2 by Optical Helicity. *Nat. Nanotechnol.* **2012**, *7* (8), 494–498. https://doi.org/10.1038/nnano.2012.96.

(102) Clark, D. J.; Senthilkumar, V.; Le, C. T.; Weerawarne, D. L.; Shim, B.; Jang, J. I.; Shim, J. H.; Cho, J.; Sim, Y.; Seong, M.-J.; et al. Strong Optical Nonlinearity of CVD-Grown MoS2 Monolayer as Probed by Wavelength-Dependent Second-Harmonic Generation. *Phys. Rev. B* **2014**, *90* (12), 121409. https://doi.org/10.1103/PhysRevB.90.121409.

(103) Wang, R.; Chien, H. C.; Kumar, J.; Kumar, N.; Chiu, H. Y.; Zhao, H. Third-Harmonic Generation in Ultrathin Films of MoS2. *ACS Appl. Mater. Interfaces* **2014**, *6*, 314–318. https://doi.org/10.1021/am4042542.

(104) Zhang, H.; Lu, S. B.; Zheng, J.; Du, J.; Wen, S. C.; Tang, D. Y.; Loh, K. P. Molybdenum Disulfide (MoS_2) as a Broadband Saturable Absorber for Ultra-Fast Photonics. *Opt. Express* **2014**, *22* (6), 7249. https://doi.org/10.1364/OE.22.007249.

(105) Lagoudakis, K. G.; Wouters, M.; Richard, M.; Baas, A.; Carusotto, I.; André, R.; Dang, L. S.; Deveaud-Plédran, B. Quantized Vortices in an Exciton–Polariton Condensate. *Nat. Phys.* **2008**, *4* (9), 706–710. https://doi.org/10.1038/nphys1051.

(106) Ye, Y.; Wong, Z. J.; Lu, X.; Ni, X.; Zhu, H.; Chen, X.; Wang, Y.; Zhang, X. Monolayer Excitonic Laser. *Nat. Photonics* **2015**, *9* (11), 733–737. https://doi.org/10.1038/nphoton.2015.197.

(107) Ye, Y.; Dou, X.; Ding, K.; Chen, Y.; Jiang, D.; Yang, F.; Sun, B. Single Photon Emission from Deep-Level Defects in Monolayer WS e 2. *Phys. Rev. B* **2017**, *95* (24), 245313. https://doi.org/10.1103/PhysRevB.95.245313.

(108) Ling, X.; Wang, H.; Huang, S.; Xia, F.; Dresselhaus, M. S. The Renaissance of Black Phosphorus. *Proc. Natl. Acad. Sci.* **2015**, *112* (15), 201416581. https://doi.org/10.1073/pnas.1416581112.

(109) Venuthurumilli, P. K.; Ye, P. D.; Xu, X. Plasmonic Resonance Enhanced Polarization-Sensitive Photodetection by Black Phosphorus in Near Infrared. *ACS Nano* **2018**, *12* (5), 4861–4867. https://doi.org/10.1021/acsnano.8b01660.

(110) Low, T.; Rodin, a S.; Carvalho, A.; Jiang, Y.; Wang, H.; Xia, F.; Neto, a H. C. Tunable Optical Properties of Multilayers Black Phosphorus. *arXiv* **2014**, *075434*, 1–5. https://doi.org/10.1103/PhysRevB.90.075434.

(111) Tran, V.; Soklaski, R.; Liang, Y.; Yang, L. Layer-Controlled Band Gap and Anisotropic Excitons in Few-Layer Black Phosphorus. *Phys. Rev. B - Condens. Matter Mater. Phys.* **2014**, *89* (23), 1–6. https://doi.org/10.1103/PhysRevB.89.235319.

(112) Qiao, J.; Kong, X.; Hu, Z.-X.; Yang, F.; Ji, W. High-Mobility Transport Anisotropy and Linear Dichroism in Few-Layer Black Phosphorus. *Nat. Commun.* **2014**, *5*, 4475. https://doi.org/10.1038/ncomms5475.

(113) Mao, N.; Tang, J.; Xie, L.; Wu, J.; Han, B.; Lin, J.; Deng, S.; Ji, W.; Xu, H.; Liu, K.; et al. Optical Anisotropy of Black Phosphorus in the Visible Regime. *J. Am. Chem. Soc.* **2016**, *138* (1), 300–305. https://doi.org/10.1021/jacs.5b10685.

(114) Luo, Z.; Maassen, J.; Deng, Y.; Du, Y.; Garrelts, R. P.; Lundstrom, M. S.; Ye, P. D.; Xu, X. Anisotropic In-Plane Thermal Conductivity Observed in Few-Layer Black Phosphorus. *Nat. Commun.* **2015**, *6* (1), 1–32. https://doi.org/10.1038/ncomms9572.

(115) Low, T.; Rold, R.; Wang, H.; Xia, F.; Avouris, P.; Mart, L. Plasmons and Screening in Monolayer and Multilayer Black Phosphorus. *Phys. Rev. Lett.* **2014**, *67* (12), 3–7. https://doi.org/10.1103/PhysRevLett.113.106802.

(116) Chen, Y.; Jiang, G.; Chen, S.; Guo, Z.; Yu, X.; Zhao, C.; Zhang, H.; Bao, Q.; Wen, S.; Tang, D.; et al. Mechanically Exfoliated Black Phosphorus as a New Saturable Absorber for Both Q-Switching and Mode-Locking Laser Operation. *Opt. Express* **2015**, *23* (10), 12823. https://doi.org/10.1364/OE.23.012823.

(117) Wang, L. L. and Y. W. and X. Ultrafast Pulse Generation with Black Phosphorus Solution Saturable Absorber. *Laser Phys.* **2017**, *27* (8), 85104.

(118) Sotor, J.; Sobon, G.; Macherzynski, W.; Paletko, P.; Abramski, K. M. Black Phosphorus Saturable Absorber for Ultrashort Pulse Generation. *Appl. Phys. Lett.* **2015**, *107* (5), 051108. https://doi.org/10.1063/1.4927673.

(119) Naguib, M. Chapter 4: Two-Dimensional Transition Metal Carbides and Carbonitrides. In *Nanomaterials handbook*; Gogotsi, Y., Ed.; Taylor & Francis, CRC Press: Boca Raton, 2017; pp 83–102.

(120) Naguib, M.; Gogotsi, Y. Synthesis of Two-Dimensional Materials by Selective Extraction. *Acc. Chem. Res.* **2015**, *48* (1), 128–135. https://doi.org/10.1021/ar500346b.

(121) Halim, J.; Lukatskaya, M. R.; Cook, K. M.; Lu, J.; Smith, C. R.; Näslund, L.-Å.; May, S. J.; Hultman, L.; Gogotsi, Y.; Eklund, P.; et al. Transparent Conductive Two-Dimensional Titanium Carbide Epitaxial Thin Films. *Chem. Mater.* **2014**, *26* (7), 2374–2381. https://doi.org/10.1021/cm500641a.

(122) Kajiyama, S.; Szabova, L.; Sodeyama, K.; Iinuma, H.; Morita, R.; Gotoh, K.; Tateyama, Y.; Okubo, M.; Yamada, A. Sodium-Ion Intercalation Mechanism in MXene Nanosheets. *ACS Nano* **2016**, *10* (3), 3334–3341. https://doi.org/10.1021/acsnano.5b06958.

(123) Lukatskaya, M. R.; Kota, S.; Lin, Z.; Zhao, M.-Q.; Shpigel, N.; Levi, M. D.; Halim, J.; Taberna, P.-L.; Barsoum, M. W.; Simon, P.; et al. Ultra-High-Rate Pseudocapacitive Energy Storage in Two-Dimensional Transition Metal Carbides. *Nat. Energy* **2017**, *2* (8), 17105. https://doi.org/10.1038/nenergy.2017.105.

(124) Tian, Y.; Yang, C.; Que, W.; Liu, X.; Yin, X.; Kong, L. B. Flexible and Free-Standing 2D Titanium Carbide Film Decorated with Manganese Oxide Nanoparticles as a High Volumetric Capacity Electrode for Supercapacitor. *J. Power Sources* **2017**, *359*, 332–339. https://doi.org/10.1016/j.jpowsour.2017.05.081.

(125) Yang, C.; Que, W.; Yin, X.; Tian, Y.; Yang, Y.; Que, M. Improved Capacitance of Nitrogen-Doped Delaminated Two-Dimensional Titanium Carbide by Urea-Assisted Synthesis. *Electrochim. Acta* **2017**, *225*, 416–424. https://doi.org/10.1016/j.electacta.2016.12.173.

(126) Shahzad, F.; Alhabeb, M.; Hatter, C. B.; Anasori, B.; Man Hong, S.; Koo, C. M.; Gogotsi, Y. Electromagnetic Interference Shielding with 2D Transition Metal Carbides (MXenes). *Science (80-.).* **2016**, *353* (6304), 1137–1140. https://doi.org/10.1126/science.aag2421.

(127) Geunchang, C.; Faisal, S.; Young- Mi, B.; Min, J. Y.; Hyunchul, P.; Mohamed, A.; Babak, A.; Dai- Sik, K.; Min, K. C.; Yury, G.; et al. Enhanced Terahertz Shielding of MXenes with Nano- Metamaterials. *Adv. Opt. Mater.* **2018**, *6* (5), 1701076. https://doi.org/10.1002/adom.201701076.

(128) Li, R.; Zhang, L.; Shi, L.; Wang, P. MXene Ti 3 C 2 : An Effective 2D Light-to-Heat Conversion Material. *ACS Nano* **2017**, *11* (4), 3752–3759. https://doi.org/10.1021/acsnano.6b08415.

(129) Jhon, Y. M. I.; Koo, J.; Anasori, B.; Seo, M.; Lee, J. H.; Gogotsi, Y.; Jhon, Y. M. I. Metallic MXene Saturable Absorber for Femtosecond Mode-Locked Lasers. *Adv. Mater.* **2017**, *29* (40), 1702496. https://doi.org/10.1002/adma.201702496.

(130) Satheeshkumar, E.; Makaryan, T.; Melikyan, A.; Minassian, H.; Gogotsi, Y.; Yoshimura, M. One-Step Solution Processing of Ag, Au and Pd@MXene Hybrids for SERS. *Sci. Rep.* **2016**, *6* (1), 32049. https://doi.org/10.1038/srep32049.

(131) Sarycheva, A.; Makaryan, T.; Maleski, K.; Satheeshkumar, E.; Melikyan, A.; Minassian, H.; Yoshimura, M.; Gogotsi, Y. Two-Dimensional Titanium Carbide (MXene) as Surface-Enhanced Raman Scattering Substrate. *J. Phys. Chem. C* **2017**, *121* (36), 19983–19988. https://doi.org/10.1021/acs.jpcc.7b08180.

(132) Chaudhuri, K.; Alhabeb, M.; Wang, Z.; Shalaev, V. M.; Gogotsi, Y.; Boltasseva, A. Highly Broadband Absorber Using Plasmonic Titanium Carbide (MXene). *ACS Photonics* **2018**, *5* (3), 1115–1122. https://doi.org/10.1021/acsphotonics.7b01439.

(133) Dong, Y.; Chertopalov, S.; Maleski, K.; Anasori, B.; Hu, L.; Bhattacharya, S.; Rao, A. M.; Gogotsi, Y.; Mochalin, V. N.; Podila, R. Saturable Absorption in 2D Ti 3 C 2 MXene Thin Films for Passive Photonic Diodes. *Adv. Mater.* **2018**, *30* (10), 1705714. https://doi.org/10.1002/adma.201705714.

(134) Khazaei, M.; Ranjbar, A.; Arai, M.; Sasaki, T.; Yunoki, S. Electronic Properties and Applications of MXenes: A Theoretical Review. *J. Mater. Chem. C* **2017**, *5* (10), 2488–2503. https://doi.org/10.1039/C7TC00140A.

(135) Lashgari, H.; Abolhassani, M. R.; Boochani, A.; Elahi, S. M.; Khodadadi, J. Electronic and Optical Properties of 2D Graphene-like Compounds Titanium Carbides and Nitrides: DFT Calculations. *Solid State Commun.* **2014**, *195*, 61–69. https://doi.org/10.1016/j.ssc.2014.06.008.

(136) Ambrosch-Draxl, C.; Sofo, J. O. Linear Optical Properties of Solids within the Full-Potential Linearized Augmented Planewave Method. *Comput. Phys. Commun.* **2006**, *175* (1), 1–14. https://doi.org/https://doi.org/10.1016/j.cpc.2006.03.005.

(137) Ren, X.; Rinke, P.; Joas, C.; Scheffler, M. Random-Phase Approximation and Its Applications in Computational Chemistry and Materials Science. *J. Mater. Sci.* **2012**, *47* (21), 7447–7471. https://doi.org/10.1007/s10853-012-6570-4.

(138) Fox, M. *Optical Properties of Solids*; Oxford University Press: Oxford, 2001. https://doi.org/10.1007/978-1-4757-5714-9_9.

(139) Wooten, F. *Optical Properties of Solids*; Academic Press: New York and London, 1972.

(140) Naguib, M.; Mashtalir, O.; Carle, J.; Presser, V.; Lu, J.; Hultman, L.; Gogotsi, Y.; Barsoum, M. W. Two-Dimensional Transition Metal Carbides. *ACS Nano* **2012**, *6* (2), 1322–1331. https://doi.org/10.1021/nn204153h.

(141) Zhang, X.; Ma, Z.; Zhao, X.; Tang, Q.; Zhou, Z. Computational Studies on Structural and Electronic Properties of Functionalized MXene Monolayers and Nanotubes. *J. Mater. Chem. A* **2015**, *3* (9), 4960–4966. https://doi.org/10.1039/C4TA06557C.

(142) Naguib, M.; Kurtoglu, M.; Presser, V.; Lu, J.; Niu, J.; Heon, M.; Hultman, L.; Gogotsi, Y.; Barsoum, M. W. Two-Dimensional Nanocrystals Produced by Exfoliation of Ti3AlC2. *Adv. Mater.* **2011**, *23* (37), 4248–4253. https://doi.org/10.1002/adma.201102306.

(143) Berdiyorov, G. R. Optical Properties of Functionalized Ti 3 C 2 T 2 (T = F, O, OH) MXene: First-Principles Calculations. *AIP Adv.* **2016**, *6* (5), 055105. https://doi.org/10.1063/1.4948799.

(144) Harrison, W. A. *Solid State Theory*; McGrawHill, 1970.

(145) Hantanasirisakul, K.; Zhao, M.-Q.; Urbankowski, P.; Halim, J.; Anasori, B.; Kota, S.; Ren, C. E.; Barsoum, M. W.; Gogotsi, Y. Fabrication of Ti3C2Tx MXene Transparent Thin Films with Tunable Optoelectronic Properties. *Adv. Electron. Mater.* **2016**, *2* (6), 1600050. https://doi.org/10.1002/aelm.201600050.

(146) Lin, H.; Wang, X.; Yu, L.; Chen, Y.; Shi, J. Two-Dimensional Ultrathin MXene Ceramic Nanosheets for Photothermal Conversion. *Nano Lett.* **2017**, *17* (1), 384–391. https://doi.org/10.1021/acs.nanolett.6b04339.

(147) Lin, H.; Wang, Y.; Gao, S.; Chen, Y.; Shi, J. Theranostic 2D Tantalum Carbide (MXene). *Adv. Mater.* **2018**, *30* (4), 1703284. https://doi.org/10.1002/adma.201703284.

(148) Jiang, X.; Liu, S.; Liang, W.; Luo, S.; He, Z.; Ge, Y.; Wang, H.; Cao, R.; Zhang, F.; Wen, Q.; et al. Broadband Nonlinear Photonics in Few-Layer MXene Ti 3 C 2 T x (T = F, O, or OH). *Laser Photon. Rev.* **2018**, *12* (2), 1700229. https://doi.org/10.1002/lpor.201700229.

(149) Maier, S. a.; Atwater, H. a. Plasmonics: Localization and Guiding of Electromagnetic Energy in Metal/Dielectric Structures. *J. Appl. Phys.* **2005**, *98* (1), 011101. https://doi.org/10.1063/1.1951057.

(150) Mauchamp, V.; Bugnet, M.; Bellido, E. P.; Botton, G. a.; Moreau, P.; Magne, D.; Naguib, M.; Cabioc'h, T.; Barsoum, M. W. Enhanced and Tunable Surface Plasmons in Two-Dimensional Ti3C2 Stacks: Electronic Structure versus Boundary Effects. *Phys. Rev. B* **2014**, *89* (23), 235428. https://doi.org/10.1103/PhysRevB.89.235428.

(151) Kumar, A.; Ahluwalia, P. K. K. Tunable Dielectric Response of Transition Metals Dichalcogenides MX2 (M=Mo, W; X=S, Se, Te): Effect of Quantum Confinement. *Phys. B Condens. Matter* **2012**, *407* (24), 4627–4634. https://doi.org/10.1016/j.physb.2012.08.034.

(152) Boersch, H.; Geiger, J.; Imbusch, A.; Niedrig, N. High Resolution Investigation of the Energy Losses of 30 KeV Electrons in Aluminum Foils of Various Thicknesses. *Phys. Lett.* **1966**, *22* (2), 146–147. https://doi.org/10.1016/0031-9163(66)90551-8.

(153) Rast, L.; Sullivan, T. J.; Tewary, V. K. Stratified Graphene/Noble Metal Systems for Low-Loss Plasmonics Applications. *Phys. Rev. B* **2013**, *87* (4), 045428. https://doi.org/10.1103/PhysRevB.87.045428.

(154) Boyd, R. W. *Nonlinear Optics*, 3rd ed.; Academic Press, 2008.

(155) Huang, X.; Jain, P. K.; El-Sayed, I. H.; El-Sayed, M. A. Plasmonic Photothermal Therapy (PPTT) Using Gold Nanoparticles. *Lasers Med. Sci.* **2008**, *23* (3), 217–228. https://doi.org/10.1007/s10103-007-0470-x.

(156) Robinson, J. T.; Tabakman, S. M.; Liang, Y.; Wang, H.; Sanchez Casalongue, H.; Vinh, D.; Dai, H. Ultrasmall Reduced Graphene Oxide with High Near-Infrared Absorbance for Photothermal Therapy. *J. Am. Chem. Soc.* **2011**, *133* (17), 6825–6831. https://doi.org/10.1021/ja2010175.

(157) Akhavan, O.; Ghaderi, E. Graphene Nanomesh Promises Extremely Efficient In Vivo Photothermal Therapy. *Small* **2013**, *9* (21), 3593–3601. https://doi.org/10.1002/smll.201203106.

(158) Liu, T.; Wang, C.; Gu, X.; Gong, H.; Cheng, L.; Shi, X.; Feng, L.; Sun, B.; Liu, Z. Drug Delivery with PEGylated MoS 2 Nano-Sheets for Combined Photothermal and Chemotherapy of Cancer. *Adv. Mater.* **2014**, *26* (21), 3433–3440. https://doi.org/10.1002/adma.201305256.

(159) Cheng, L.; Liu, J.; Gu, X.; Gong, H.; Shi, X.; Liu, T.; Wang, C.; Wang, X.; Liu, G.; Xing, H.; et al. PEGylated WS 2 Nanosheets as a Multifunctional Theranostic Agent for in Vivo Dual-Modal CT/Photoacoustic Imaging Guided Photothermal Therapy. *Adv. Mater.* **2014**, *26* (12), 1886–1893. https://doi.org/10.1002/adma.201304497.

(160) Lin, H.; Gao, S.; Dai, C.; Chen, Y.; Shi, J. A Two-Dimensional Biodegradable Niobium Carbide (MXene) for Photothermal Tumor Eradication in NIR-I and NIR-II Biowindows. *J. Am. Chem. Soc.* **2017**, *139* (45), 16235–16247. https://doi.org/10.1021/jacs.7b07818.

(161) Lipatov, A.; Alhabeb, M.; Lukatskaya, M. R.; Boson, A.; Gogotsi, Y.; Sinitskii, A. Effect of Synthesis on Quality, Electronic Properties and Environmental Stability of Individual Monolayer Ti 3 C 2 MXene Flakes. *Adv. Electron. Mater.* **2016**, *2* (12), 1600255. https://doi.org/10.1002/aelm.201600255.

(162) Marini, A.; García de Abajo, F. J. Graphene-Based Active Random Metamaterials for Cavity-Free Lasing. *Phys. Rev. Lett.* **2016**, *116* (21), 217401. https://doi.org/10.1103/PhysRevLett.116.217401.

(163) Wang, Z.; Meng, X.; Chaudhuri, K.; Alhabeb, M.; Kim, Y. L. Y. L.; Shalaev, V. M. V. M.; Gogotsi, Y.; Boltasseva, A.; Azzam, S. I.; Kildishev, A. V.; et al. Active Metamaterials Based on Monolayer Titanium Carbide MXene for Random Lasing. In *Conference on Lasers and Electro-Optics*; OSA: Washington, D.C., 2017; p FTu4G.7. https://doi.org/10.1364/CLEO_QELS.2017.FTu4G.7.

(164) Verslegers, L.; Catrysse, P. B.; Yu, Z.; White, J. S.; Barnard, E. S.; Brongersma, M. L.; Fan, S. Planar Lenses Based on Nanoscale Slit Arrays in a Metallic Film. *Nano Lett.* **2009**, *9* (1), 235–238. https://doi.org/10.1021/nl802830y.

(165) Willets, K. A.; Van Duyne, R. P. Localized Surface Plasmon Resonance Spectroscopy and Sensing. *Annu. Rev. Phys. Chem.* **2007**, *58* (1), 267–297. https://doi.org/10.1146/annurev.physchem.58.032806.104607.

(166) Berini, P. Surface Plasmon Photodetectors and Their Applications. *Laser Photon. Rev.* **2014**, *8* (2), 197–220. https://doi.org/10.1002/lpor.201300019.

(167) Zheludev, N. I.; Prosvirnin, S. L.; Papasimakis, N.; Fedotov, V. A. Lasing Spaser. *Nat. Photonics* **2008**, *2* (6), 351–354. https://doi.org/10.1038/nphoton.2008.82.

(168) Meng, X.; Liu, J.; Kildishev, A. V.; Shalaev, V. M. Highly Directional Spaser Array for the Red Wavelength Region. *Laser Photonics Rev.* **2014**, *8* (6), 896–903. https://doi.org/10.1002/lpor.201400056.

(169) Baffou, G.; Quidant, R. Thermo-Plasmonics: Using Metallic Nanostructures as Nano-Sources of Heat. *Laser Photon. Rev.* **2013**, *7* (2), 171–187. https://doi.org/10.1002/lpor.201200003.

(170) Coppens, Z. J.; Li, W.; Walker, D. G.; Valentine, J. G. Probing and Controlling Photothermal Heat Generation in Plasmonic Nanostructures. *Nano Lett.* **2013**, *13* (3), 1023–1028. https://doi.org/10.1021/nl304208s.

(171) Mubeen, S.; Lee, J.; Lee, W.; Singh, N.; Stucky, G. D.; Moskovits, M. On the Plasmonic Photovoltaic. *ACS Nano* **2014**, *8* (6), 6066–6073. https://doi.org/10.1021/nn501379r.

(172) Pan, Y.; Tagliabue, G.; Eghlidi, H.; Höller, C.; Dröscher, S.; Hong, G.; Poulikakos, D. A Rapid Response Thin-Film Plasmonic-Thermoelectric Light Detector. *Sci. Rep.* **2016**, *6* (1), 37564. https://doi.org/10.1038/srep37564.

(173) Naldoni, A.; Riboni, F.; Guler, U.; Boltasseva, A.; Shalaev, V. M.; Kildishev, A. V. Solar-Powered Plasmon-Enhanced Heterogeneous Catalysis. *Nanophotonics* **2016**, *5* (1), 112. https://doi.org/10.1515/nanoph-2016-0018.

(174) Watts, C. M.; Liu, X.; Padilla, W. J. Metamaterial Electromagnetic Wave Absorbers. *Adv. Mater.* **2012**, *24* (23), 98–120. https://doi.org/10.1002/adma.201200674.

(175) Cheng, C.-W.; Abbas, M. N.; Chiu, C.-W.; Lai, K.-T.; Shih, M.-H.; Chang, Y.-C. Wide-Angle Polarization Independent Infrared Broadband Absorbers Based on Metallic Multi-Sized Disk Arrays. *Opt. Express* **2012**, *20* (9), 10376–10381. https://doi.org/10.1364/OE.20.010376.

(176) Hao, J.; Wang, J.; Liu, X.; Padilla, W. J.; Zhou, L.; Qiu, M. High Performance Optical Absorber Based on a Plasmonic Metamaterial. *Appl. Phys. Lett.* **2010**, *96* (25), 251104. https://doi.org/10.1063/1.3442904.

(177) Chirumamilla, M.; Chirumamilla, A.; Yang, Y.; Roberts, A. S. A. S.; Kristensen, P. K. P. K.; Chaudhuri, K.; Boltasseva, A.; Sutherland, D. S. D. S.; Bozhevolnyi, S. I. S. I.; Pedersen, K. Large-Area Ultrabroadband Absorber for Solar Thermophotovoltaics Based on 3D Titanium Nitride Nanopillars. *Adv. Opt. Mater.* **2017**, *5* (22), 1700552. https://doi.org/10.1002/adom.201700552.

(178) Li, H.; Wang, L.; Zhai, X. Tunable Graphene-Based Mid-Infrared Plasmonic Wide-Angle Narrowband Perfect Absorber. *Sci. Rep.* **2016**, *6* (1), 36651. https://doi.org/10.1038/srep36651.

(179) Long, Y.; Shen, L.; Xu, H.; Deng, H.; Li, Y. Achieving Ultranarrow Graphene Perfect Absorbers by Exciting Guided-Mode Resonance of One-Dimensional Photonic Crystals. *Sci. Rep.* **2016**, *6* (1), 32312. https://doi.org/10.1038/srep32312.

(180) Wu, K.; Zhang, X.; Wang, J.; Li, X.; Chen, J. WS2 as a Saturable Absorber for Ultrafast Photonic Applications of Mode-Locked and Q-Switched Lasers. *Opt. Express* **2015**, *23* (9), 11453. https://doi.org/10.1364/OE.23.011453.

(181) Lu, S. B.; Miao, L. L.; Guo, Z. N.; Qi, X.; Zhao, C. J.; Zhang, H.; Wen, S. C.; Tang, D. Y.; Fan, D. Y. Broadband Nonlinear Optical Response in Multi-Layer Black Phosphorus: An Emerging Infrared and Mid-Infrared Optical Material. *Opt. Express* **2015**, *23* (9), 11183. https://doi.org/10.1364/OE.23.011183.

(182) Cai, W.; Shalaev, V. *Optical Metamaterials*; Springer: New York, 2010. https://doi.org/10.1007/978-1-4419-1151-3.

(183) Ding, F.; Jin, Y.; Li, B.; Cheng, H.; Mo, L.; He, S. Ultrabroadband Strong Light Absorption Based on Thin Multilayered Metamaterials. *Laser Photon. Rev.* **2014**, *8* (6), 946–953. https://doi.org/10.1002/lpor.201400157.

(184) Halim, J.; Kota, S.; Lukatskaya, M. R.; Naguib, M.; Zhao, M.-Q.; Moon, E. J.; Pitock, J.; Nanda, J.; May, S. J.; Gogotsi, Y.; et al. Synthesis and Characterization of 2D Molybdenum Carbide (MXene). *Adv. Funct. Mater.* **2016**, *26* (18), 3118–3127. https://doi.org/10.1002/adfm.201505328.

(185) Anasori, B.; Lukatskaya, M. R.; Gogotsi, Y. 2D Metal Carbides and Nitrides (MXenes) for Energy Storage. *Nat. Rev. Mater.* **2017**, *2* (2), 16098. https://doi.org/10.1038/natrevmats.2016.98.

(186) Kildishev, A. V.; Boltasseva, A.; Shalaev, V. M. Planar Photonics with Metasurfaces. *Science (80-.).* **2013**, *339* (6125), 1232009–1232009. https://doi.org/10.1126/science.1232009.

(187) Hong Ng, V. M.; Huang, H.; Zhou, K.; Lee, P. S.; Que, W.; Xu, J. Z.; Kong, L. B. Recent Progress in Layered Transition Metal Carbides and/or Nitrides (MXenes) and Their Composites: Synthesis and Applications. *J. Mater. Chem. A* **2017**, *5* (7), 3039–3068. https://doi.org/10.1039/C6TA06772G.

(188) Hope, M. A.; Forse, A. C.; Griffith, K. J.; Lukatskaya, M. R.; Ghidiu, M.; Gogotsi, Y.; Grey, C. P. NMR Reveals the Surface Functionalisation of Ti 3 C 2 MXene. *Phys. Chem. Chem. Phys.* **2016**, *18* (7), 5099–5102. https://doi.org/10.1039/C6CP00330C.

(189) Wang, H.-W.; Naguib, M.; Page, K.; Wesolowski, D. J.; Gogotsi, Y. Resolving the Structure of Ti 3 C 2 T x MXenes through Multilevel Structural Modeling of the Atomic Pair Distribution Function. *Chem. Mater.* **2016**, *28* (1), 349–359. https://doi.org/10.1021/acs.chemmater.5b04250.

(190) Han, M.; Yin, X.; Wu, H.; Hou, Z.; Song, C.; Li, X.; Zhang, L.; Cheng, L. Ti 3 C 2 MXenes with Modified Surface for High-Performance Electromagnetic Absorption and Shielding in the X-Band. *ACS Appl. Mater. Interfaces* **2016**, *8* (32), 21011–21019. https://doi.org/10.1021/acsami.6b06455.

(191) Liu, J.; Zhang, H.-B.; Sun, R.; Liu, Y.; Liu, Z.; Zhou, A.; Yu, Z.-Z. Hydrophobic, Flexible, and Lightweight MXene Foams for High-Performance Electromagnetic-Interference Shielding. *Adv. Mater.* **2017**, *29* (38), 1702367. https://doi.org/10.1002/adma.201702367.

(192) Ren, C. E.; Hatzell, K. B.; Alhabeb, M.; Ling, Z.; Mahmoud, K. A.; Gogotsi, Y. Charge- and Size-Selective Ion Sieving Through Ti3C2Tx MXene Membranes. *J. Phys. Chem. Lett.* **2015**, *6* (20), 4026–4031. https://doi.org/10.1021/acs.jpclett.5b01895.

(193) Romer, F. M.; Wiedwald, U.; Strusch, T.; Halim, J.; Mayerberger, E.; Barsoum, M. W.; Farle, M. Controlling the Conductivity of Ti3C2 MXenes by Inductively Coupled Oxygen and Hydrogen Plasma Treatment and Humidity. *RSC Adv.* **2017**, *7* (22), 13097–13103. https://doi.org/10.1039/C6RA27505B.

(194) Miranda, A.; Halim, J.; Barsoum, M. W.; Lorke, A. Electronic Properties of Freestanding Ti 3 C 2 T x MXene Monolayers. *Appl. Phys. Lett.* **2016**, *108* (3), 033102. https://doi.org/10.1063/1.4939971.

(195) Pors, A.; Albrektsen, O.; Radko, I. P.; Bozhevolnyi, S. I. Gap Plasmon-Based Metasurfaces for Total Control of Reflected Light. *Sci. Rep.* **2013**, *3*, 2155. https://doi.org/10.1038/srep02155.

(196) Jung, J.; Søndergaard, T.; Bozhevolnyi, S. I. Gap Plasmon-Polariton Nanoresonators: Scattering Enhancement and Launching of Surface Plasmon Polaritons. *Phys. Rev. B* **2009**, *79* (3), 035401. https://doi.org/10.1103/PhysRevB.79.035401.

(197) Bozhevolnyi, S. I.; Søndergaard, T. General Properties of Slow-Plasmon Resonant Nanostructures: Nano-Antennas and Resonators. *Opt. Express* **2007**, *15* (17), 10869–10877. https://doi.org/10.1364/OE.15.010869.

(198) Oulton, R. F.; Sorger, V. J.; Genov, D. A.; Pile, D. F. P.; Zhang, X. A Hybrid Plasmonic Waveguide for Subwavelength Confinement and Long-Range Propagation. *Nat. Photonics* **2008**, *2* (8), 496–500. https://doi.org/10.1038/nphoton.2008.131.

(199) Anker, J. N.; Hall, W. P.; Lyandres, O.; Shah, N. C.; Zhao, J.; Van Duyne, R. P. Biosensing with Plasmonic Nanosensors. *Nat. Mater.* **2008**, *7* (6), 442–453. https://doi.org/10.1038/nmat2162.

(200) Joy, N. A.; Nandasiri, M. I.; Rogers, P. H.; Jiang, W.; Varga, T.; Kuchibhatla, S. V. N. T.; Thevuthasan, S.; Carpenter, M. A. Selective Plasmonic Gas Sensing: H2, NO2, and CO Spectral Discrimination by a Single Au-CeO2 Nanocomposite Film. *Anal. Chem.* **2012**, *84* (11), 5025–5034. https://doi.org/10.1021/ac3006846.

(201) Yu, N.; Capasso, F. Flat Optics with Designer Metasurfaces. *Nat. Mater.* **2014**, *13* (2), 139–150. https://doi.org/10.1038/nmat3839.

(202) Chen, H.-T.; Taylor, A. J.; Yu, N. A Review of Metasurfaces: Physics and Applications. *Reports Prog. Phys.* **2016**, *79* (7), 076401. https://doi.org/10.1088/0034-4885/79/7/076401.

(203) Chang, S.; Guo, X.; Ni, X. Optical Metasurfaces: Progress and Applications. *Annu. Rev. Mater. Res.* **2018**, *48* (1), 279–302. https://doi.org/10.1146/annurev-matsci-070616-124220.

(204) Arbabi, E.; Arbabi, A.; Kamali, S. M.; Horie, Y.; Faraji-Dana, M.; Faraon, A. MEMS-Tunable Dielectric Metasurface Lens. *Nat. Commun.* **2018**, *9* (1), 812. https://doi.org/10.1038/s41467-018-03155-6.

(205) Chen, X.; Huang, L.; Mühlenbernd, H.; Li, G.; Bai, B.; Tan, Q.; Jin, G.; Qiu, C.-W.; Zhang, S.; Zentgraf, T. Dual-Polarity Plasmonic Metalens for Visible Light. *Nat. Commun.* **2012**, *3* (1), 1198. https://doi.org/10.1038/ncomms2207.

(206) Zheng, G.; Mühlenbernd, H.; Kenney, M.; Li, G.; Zentgraf, T.; Zhang, S. Metasurface Holograms Reaching 80% Efficiency. *Nat. Nanotechnol.* **2015**, *10* (4), 308–312. https://doi.org/10.1038/nnano.2015.2.

(207) Wan, W.; Gao, J.; Yang, X. Full-Color Plasmonic Metasurface Holograms. *ACS Nano* **2016**, *10* (12), 10671–10680. https://doi.org/10.1021/acsnano.6b05453.

(208) Tahir, A. A.; Schulz, S. A.; De Leon, I.; Boyd, R. W. Design Principles for Wave Plate Metasurfaces Using Plasmonic L-Shaped Nanoantennas. *J. Opt.* **2017**, *19* (3), 035001. https://doi.org/10.1088/2040-8986/aa5648.

(209) Liu, Z.; Li, Z.; Liu, Z.; Cheng, H.; Liu, W.; Tang, C.; Gu, C.; Li, J.; Chen, H.-T.; Chen, S.; et al. Single-Layer Plasmonic Metasurface Half-Wave Plates with Wavelength-Independent Polarization Conversion Angle. *ACS Photonics* **2017**, *4* (8), 2061–2069. https://doi.org/10.1021/acsphotonics.7b00491.

(210) Zhu, A. Y.; Chen, W.-T.; Khorasaninejad, M.; Oh, J.; Zaidi, A.; Mishra, I.; Devlin, R. C.; Capasso, F. Ultra-Compact Visible Chiral Spectrometer with Meta-Lenses. *APL Photonics* **2017**, *2* (3), 036103. https://doi.org/10.1063/1.4974259.

(211) Colomban, P. The Use of Metal Nanoparticles to Produce Yellow, Red and Iridescent Colour, from Bronze Age to Present Times in Lustre Pottery and Glass: Solid State Chemistry, Spectroscopy and Nanostructure. *J. Nano Res.* **2009**, *8*, 109–132. https://doi.org/10.4028/www.scientific.net/JNanoR.8.109.

(212) Shaltout, A.; Liu, J.; Kildishev, A.; Shalaev, V. Photonic Spin Hall Effect in Gap–Plasmon Metasurfaces for on-Chip Chiroptical Spectroscopy. *Optica* **2015**, *2* (10), 860. https://doi.org/10.1364/OPTICA.2.000860.

(213) Maguid, E.; Yulevich, I.; Veksler, D.; Kleiner, V.; Brongersma, M. L.; Hasman, E. Photonic Spin-Controlled Multifunctional Shared-Aperture Antenna Array. *Science* **2016**, *352* (6290), 1202–1206. https://doi.org/10.1126/science.aaf3417.

(214) Shaltout, A.; Liu, J.; Shalaev, V. M.; Kildishev, A. V. Optically Active Metasurface with Non-Chiral Plasmonic Nanoantennas. *Nano Lett.* **2014**, *14* (8), 4426–4431. https://doi.org/10.1021/nl501396d.

(215) Bomzon, Z.; Kleiner, V.; Hasman, E. Pancharatnam–Berry Phase in Space-Variant Polarization-State Manipulations with Subwavelength Gratings. *Opt. Lett.* **2001**, *26* (18), 1424. https://doi.org/10.1364/OL.26.001424.

(216) Choudhury, S. M.; Wang, D.; Chaudhuri, K.; DeVault, C.; Kildishev, A. V.; Boltasseva, A.; Shalaev, V. M. Material Platforms for Optical Metasurfaces. *Nanophotonics* **2018**, *7* (6), 959–987. https://doi.org/10.1515/nanoph-2017-0130.

(217) Wu, C.; Khanikaev, A. B.; Adato, R.; Arju, N.; Yanik, A. A.; Altug, H.; Shvets, G. Fano-Resonant Asymmetric Metamaterials for Ultrasensitive Spectroscopy and Identification of Molecular Monolayers. *Nat. Mater.* **2012**, *11* (1), 69–75. https://doi.org/10.1038/nmat3161.

(218) Jiang, L.; Zeng, S.; Ouyang, Q.; Dinh, X.-Q.; Coquet, P.; Qu, J.; He, S.; Yong, K.-T. Graphene-TMDC-Graphene Hybrid Plasmonic Metasurface for Enhanced Biosensing: A Theoretical Analysis. *Phys. status solidi* **2017**, *214* (12), 1700563. https://doi.org/10.1002/pssa.201700563.

(219) Fan, J.-R.; Zhu, J.; Wu, W.-G.; Huang, Y. Plasmonic Metasurfaces Based on Nanopin-Cavity Resonator for Quantitative Colorimetric Ricin Sensing. *Small* **2017**, *13* (1), 1601710. https://doi.org/10.1002/smll.201601710.

(220) Costantini, D.; Lefebvre, A.; Coutrot, A.-L.; Moldovan-Doyen, I.; Hugonin, J.-P.; Boutami, S.; Marquier, F.; Benisty, H.; Greffet, J.-J. Plasmonic Metasurface for Directional and Frequency-Selective Thermal Emission. *Phys. Rev. Appl.* **2015**, *4* (1), 014023. https://doi.org/10.1103/PhysRevApplied.4.014023.

(221) Cui, T.-J.; Liu, S.; Li, L.-L. Information Entropy of Coding Metasurface. *Light Sci. Appl.* **2016**, *5* (11), e16172–e16172. https://doi.org/10.1038/lsa.2016.172.

(222) Kamali, S. M.; Arbabi, E.; Arbabi, A.; Horie, Y.; Faraji-Dana, M.; Faraon, A. Angle-Multiplexed Metasurfaces: Encoding Independent Wavefronts in a Single Metasurface under Different Illumination Angles. *Phys. Rev. X* **2017**, *7* (4), 41056.

(223) Walter, F.; Li, G.; Meier, C.; Zhang, S.; Zentgraf, T. Ultrathin Nonlinear Metasurface for Optical Image Encoding. *Nano Lett.* **2017**, *17* (5), 3171–3175. https://doi.org/10.1021/acs.nanolett.7b00676.

(224) West, P.; Ishii, S.; Naik, G. V; Emani, N.; Boltasseva, A. *Identifying Low-Loss Plasmonic Materials*; 2010. https://doi.org/10.1117/2.1201009.003167.

(225) Jahani, S.; Jacob, Z. All-Dielectric Metamaterials. *Nat. Nanotechnol.* **2016**, *11* (1), 23–36. https://doi.org/10.1038/nnano.2015.304.

(226) Decker, M.; Staude, I.; Falkner, M.; Dominguez, J.; Neshev, D. N.; Brener, I.; Pertsch, T.; Kivshar, Y. S. High-Efficiency Dielectric Huygens' Surfaces. *Adv. Opt. Mater.* **2015**, *3* (6), 813–820. https://doi.org/10.1002/adom.201400584.

(227) Nielsen, M. G.; Bozhevolnyi, S. I. Gap Plasmon-Based Metasurfaces: Fundamentals and Applications; Engheta, N., Noginov, M. A., Zheludev, N. I., Eds.; 2014; Vol. 9160, p 916006. https://doi.org/10.1117/12.2060532.

(228) West, P. R.; Ishii, S.; Naik, G. V.; Emani, N. K.; Shalaev, V. M.; Boltasseva, A. Searching for Better Plasmonic Materials. *Laser Photon. Rev.* **2010**, *4* (6), 795–808. https://doi.org/10.1002/lpor.200900055.

(229) Doering, R.; Nishi, Y. *Handbook of Semiconductor Manufacturing Technology*, Second.; CRC Press, 2007.

(230) Franey, J. P.; Kammlott, G. W.; Graedel, T. E. The Corrosion of Silver by Atmospheric Sulfurous Gases. *Corros. Sci.* **1985**, *25* (2), 133–143. https://doi.org/10.1016/0010-938X(85)90104-0.

(231) Shah, D.; Reddy, H.; Kinsey, N.; Shalaev, V. M.; Boltasseva, A. Optical Properties of Plasmonic Ultrathin TiN Films. *Adv. Opt. Mater.* **2017**, *5* (13), 1700065. https://doi.org/10.1002/adom.201700065.

(232) Kinsey, N.; Ferrera, M.; Naik, G. V.; Babicheva, V. E.; Shalaev, V. M.; Boltasseva, A. Experimental Demonstration of Titanium Nitride Plasmonic Interconnects. *Opt. Express* **2014**, *22* (10), 12238. https://doi.org/10.1364/OE.22.012238.

(233) Patsalas, P.; Kalfagiannis, N.; Kassavetis, S.; Abadias, G.; Bellas, D. V.; Lekka, C.; Lidorikis, E. Conductive Nitrides: Growth Principles, Optical and Electronic Properties, and Their Perspectives in Photonics and Plasmonics. *Mater. Sci. Eng. R Reports* **2018**, *123*, 1–55. https://doi.org/10.1016/j.mser.2017.11.001.

(234) Patsalas, P.; Logothetidis, S. Interface Properties and Structural Evolution of TiN/Si and TiN/GaN Heterostructures. *J. Appl. Phys.* **2003**, *93* (2), 989–998. https://doi.org/10.1063/1.1531812.

(235) Liu, Y.; Matsukawa, T.; Endo, K.; Masahara, M.; Ishii, K.; O'uchi, S. i.; Yamauchi, H.; Tsukada, J.; Ishikawa, Y.; Suzuki, E. Advanced FinFET CMOS Technology: TiN-Gate, Fin-Height Control and Asymmetric Gate Insulator Thickness 4T-FinFETs. In *2006 International Electron Devices Meeting*; 2006; pp 1–4. https://doi.org/10.1109/IEDM.2006.346953.

(236) Garcia, A. S.; Diniz, J. A.; Swart, J. W.; Lima, L. P. B.; Santos, M. V. P. dos. Formation and Characterization of Tin Layers for Metal Gate Electrodes of CMOS Capacitors. In *2014 International Caribbean Conference on Devices, Circuits and Systems (ICCDCS)*; 2014; pp 1–6. https://doi.org/10.1109/ICCDCS.2014.7016171.

(237) Reinholdt, A.; Pecenka, R.; Pinchuk, A.; Runte, S.; Stepanov, A. L.; Weirich, T. E.; Kreibig, U. Structural, Compositional, Optical and Colorimetric Characterization of TiN-Nanoparticles. *Eur. Phys. J. D* **2004**, *31* (1), 69–76. https://doi.org/10.1140/epjd/e2004-00129-8.

(238) Briggs, J. A.; Naik, G. V; Petach, T. A.; Baum, B. K.; Goldhaber-Gordon, D.; Dionne, J. A. Fully CMOS-Compatible Titanium Nitride Nanoantennas. *Appl. Phys. Lett.* **2016**, *108* (5), 051110. https://doi.org/10.1063/1.4941413.

(239) Yu, I.-S.; Cheng, H.-E.; Chang, C.-C.; Lin, Y.-W.; Chen, H.-T.; Wang, Y.-C.; Yang, Z.-P. Substrate-Insensitive Atomic Layer Deposition of Plasmonic Titanium Nitride Films. *Opt. Mater. Express* **2017**, *7* (3), 777. https://doi.org/10.1364/OME.7.000777.

(240) Sugavaneshwar, R. P.; Ishii, S.; Dao, T. D.; Ohi, A.; Nabatame, T.; Nagao, T. Fabrication of Highly Metallic TiN Films by Pulsed Laser Deposition Method for Plasmonic Applications. *ACS Photonics* **2018**, *5* (3), 814–819. https://doi.org/10.1021/acsphotonics.7b00942.

(241) Lalisse, A.; Tessier, G.; Plain, J.; Baffou, G. Plasmonic Efficiencies of Nanoparticles Made of Metal Nitrides (TiN, ZrN) Compared with Gold. *Sci. Rep.* **2016**, *6* (1), 38647. https://doi.org/10.1038/srep38647.

(242) Kinsey, N.; Syed, A. A.; Courtwright, D.; DeVault, C.; Bonner, C. E.; Gavrilenko, V. I.; Shalaev, V. M.; Hagan, D. J.; Van Stryland, E. W.; Boltasseva, A. Effective Third-Order Nonlinearities in Metallic Refractory Titanium Nitride Thin Films. *Opt. Mater. Express* **2015**, *5* (11), 2395. https://doi.org/10.1364/OME.5.002395.

(243) Capretti, A.; Wang, Y.; Engheta, N.; Dal Negro, L. Comparative Study of Second-Harmonic Generation from Epsilon-Near-Zero Indium Tin Oxide and Titanium Nitride Nanolayers Excited in the Near-Infrared Spectral Range. *ACS Photonics* **2015**, *2* (11), 1584–1591. https://doi.org/10.1021/acsphotonics.5b00355.

(244) Gui, L.; Bagheri, S.; Strohfeldt, N.; Hentschel, M.; Zgrabik, C. M.; Metzger, B.; Linnenbank, H.; Hu, E. L.; Giessen, H. Nonlinear Refractory Plasmonics with Titanium Nitride Nanoantennas. *Nano Lett.* **2016**, *16* (9), 5708–5713. https://doi.org/10.1021/acs.nanolett.6b02376.

(245) Reddy, H.; Guler, U.; Kudyshev, Z.; Kildishev, A. V; Shalaev, V. M.; Boltasseva, A. Temperature-Dependent Optical Properties of Plasmonic Titanium Nitride Thin Films. *ACS Photonics* **2017**, *4* (6), 1413–1420. https://doi.org/10.1021/acsphotonics.7b00127.

(246) Bouillard, J.-S. G.; Dickson, W.; O'Connor, D. P.; Wurtz, G. A.; Zayats, A. V. Low-Temperature Plasmonics of Metallic Nanostructures. *Nano Lett.* **2012**, *12* (3), 1561–1565. https://doi.org/10.1021/nl204420s.

(247) Ishii, S.; Sugavaneshwar, R. P.; Nagao, T. Titanium Nitride Nanoparticles as Plasmonic Solar Heat Transducers. *J. Phys. Chem. C* **2016**, *120* (4), 2343–2348. https://doi.org/10.1021/acs.jpcc.5b09604.

(248) Naik, G. V; Schroeder, J. L.; Ni, X.; Kildishev, A. V; Sands, T. D.; Boltasseva, A. Titanium Nitride as a Plasmonic Material for Visible and Near-Infrared Wavelengths. *Opt. Mater. Express* **2012**, *2* (4), 478. https://doi.org/10.1364/OME.2.000478.

(249) Zgrabik, C. M.; Hu, E. L. Optimization of Sputtered Titanium Nitride as a Tunable Metal for Plasmonic Applications. *Opt. Mater. Express* **2015**, *5* (12), 2786. https://doi.org/10.1364/OME.5.002786.

(250) Hu, J.; Ren, X.; Reed, A. N.; Reese, T.; Rhee, D.; Howe, B.; Lauhon, L. J.; Urbas, A. M.; Odom, T. W. Evolutionary Design and Prototyping of Single Crystalline Titanium Nitride Lattice Optics. *ACS Photonics* **2017**, *4* (3), 606–612. https://doi.org/10.1021/acsphotonics.6b00955.

(251) Lee, W.; A., W. B. Protein Secondary Structure Analyses from Circular Dichroism Spectroscopy: Methods and Reference Databases . *Biopolymers* **2007**, *89* (5), 392–400. https://doi.org/10.1002/bip.20853.

(252) Freedman, T. B.; Cao, X.; Dukor, R. K.; Nafie, L. A. Absolute Configuration Determination of Chiral Molecules in the Solution State Using Vibrational Circular Dichroism. *Chirality* **2003**, *15*, 743–758.

(253) Tsankov, D.; Eggimann, T.; Wieser, H. Alternative Design for Improved FT-IR/VCD Capabilities. *Appl. Spectrosc.* **1995**, *49* (1), 132–138.

(254) Liu, Y.; Ke, Y.; Wen, S.; Luo, H. Photonic Spin Hall Effect in Metasurfaces: A Brief Review. *Nanophotonics* **2017**, *6* (1), 51–70. https://doi.org/10.1515/nanoph-2015-0155.

(255) Shitrit, N.; Yulevich, I.; Maguid, E.; Ozeri, D.; Veksler, D.; Kleiner, V.; Hasman, E. Spin-Optical Metamaterial Route to Spin-Controlled Photonics. *Science (80-.).* **2013**, *340* (6133), 724–726. https://doi.org/10.1126/science.1234892.

(256) Jones, R. C. A New Calculus for the Treatment of Optical Systems. IV. *J. Opt. Soc. Am.* **1942**, *32* (1), 486–494.

(257) Bomzon, Z.; Biener, G.; Kleiner, V.; Hasman, E. Space-Variant Pancharatnam–Berry Phase Optical Elements with Computer-Generated Subwavelength Gratings. *Opt. Lett.* **2002**, *27* (13), 1141. https://doi.org/10.1364/OL.27.001141.

(258) Berry, M. V. The Adiabatic Phase and Pancharatnam's Phase for Polarized Light. *J. Mod. Opt.* **1987**, *34* (11), 1401–1407. https://doi.org/10.1080/09500348714551321.

(259) Shen, P.-T.; Sivan, Y.; Lin, C.-W.; Liu, H.-L.; Chang, C.-W.; Chu, S.-W. Temperature- and Roughness- Dependent Permittivity of Annealed/Unannealed Gold Films. *Opt. Express* **2016**, *24* (17), 19254. https://doi.org/10.1364/OE.24.019254.

(260) Makise, K.; Sun, R.; Terai, H.; Wang, Z. Fabrication and Characterization of Epitaxial TiN-Based Josephson Junctions for Superconducting Circuit Applications. *IEEE Trans. Appl. Supercond.* **2015**, *25* (3), 1–4. https://doi.org/10.1109/TASC.2014.2364214.

(261) Hunter, G. W.; Wrbanek, J. D.; Okojie, R. S.; Neudeck, P. G.; Fralick, G. C.; Chen, L.; Xu, J.; Beheim, G. M. Development and Application of High-Temperature Sensors and Electronics for Propulsion Applications; Korman, V., Ed.; International Society for Optics and Photonics, 2006; Vol. 6222, p 622209. https://doi.org/10.1117/12.668458.

(262) Turner, R. C.; Fuierer, P. A.; Newnham, R. E.; Shrout, T. R. Materials for High Temperature Acoustic and Vibration Sensors: A Review. *Appl. Acoust.* **1994**, *41* (4), 299–324. https://doi.org/10.1016/0003-682X(94)90091-4.

(263) Jiang, X.; Kim, K.; Zhang, S.; Johnson, J.; Salazar, G.; Jiang, X.; Kim, K.; Zhang, S.; Johnson, J.; Salazar, G. High-Temperature Piezoelectric Sensing. *Sensors* **2013**, *14* (1), 144–169. https://doi.org/10.3390/s140100144.

(264) Knobloch, A.; Ahmad, F.; Sexton, D.; Vernooy, D.; Knobloch, A. J.; Ahmad, F. R.; Sexton, D. W.; Vernooy, D. W. Remote Driven and Read MEMS Sensors for Harsh Environments. *Sensors* **2013**, *13* (10), 14175–14188. https://doi.org/10.3390/s131014175.

(265) Wang, J.; Dong, B.; Lally, E.; Gong, J.; Han, M.; Wang, A. Multiplexed High Temperature Sensing with Sapphire Fiber Air Gap-Based Extrinsic Fabry–Perot Interferometers. *Opt. Lett.* **2010**, *35* (5), 619. https://doi.org/10.1364/OL.35.000619.

(266) Huang, J.; Wang, T.; Hua, L.; Fan, J.; Xiao, H.; Luo, M.; Huang, J.; Wang, T.; Hua, L.; Fan, J.; et al. A Coaxial Cable Fabry-Perot Interferometer for Sensing Applications. *Sensors* **2013**, *13* (11), 15252–15260. https://doi.org/10.3390/s131115252.

(267) Riza, N. A.; Sheikh, M.; Perez, F. Hybrid Wireless-Wired Optical Sensor for Extreme Temperature Measurement in Next Generation Energy Efficient Gas Turbines. *J. Eng. Gas Turbines Power* **2010**, *132* (5), 051601. https://doi.org/10.1115/1.3204509.

(268) Nguyen, L. V.; Hwang, D.; Moon, S.; Moon, D. S.; Chung, Y. High Temperature Fiber Sensor with High Sensitivity Based on Core Diameter Mismatch. *Opt. Express* **2008**, *16* (15), 11369. https://doi.org/10.1364/OE.16.011369.

(269) Barrera, D.; Finazzi, V.; Villatoro, J.; Sales, S.; Pruneri, V. Packaged Optical Sensors Based on Regenerated Fiber Bragg Gratings for High Temperature Applications. *IEEE Sens. J.* **2012**, *12* (1), 107–112. https://doi.org/10.1109/JSEN.2011.2122254.

(270) Shalaev, V. M.; Kawata, S. *Nanophotonics with Surface Plasmons*; Elsevier, 2007.

(271) Reddy, H.; Guler, U.; Chaudhuri, K.; Dutta, A.; Kildishev, A. V.; Shalaev, V. M.; Boltasseva, A. Temperature-Dependent Optical Properties of Single Crystalline and Polycrystalline Silver Thin Films. *ACS Photonics* **2017**, *4* (5). https://doi.org/10.1021/acsphotonics.6b00886.

(272) Guler, U.; Kildishev, A. V; Boltasseva, A.; Shalaev, V. M. Plasmonics on the Slope of Enlightenment: The Role of Transition Metal Nitrides. *Faraday Discuss.* **2015**, *178*, 71–86. https://doi.org/10.1039/C4FD00208C.

(273) Saha, B.; Naik, G. V.; Saber, S.; Akatay, C.; Stach, E. A.; Shalaev, V. M.; Boltasseva, A.; Sands, T. D. TiN/(Al,Sc)N Metal/Dielectric Superlattices and Multilayers as Hyperbolic Metamaterials in the Visible Spectral Range. *Phys. Rev. B* **2014**, *90* (12), 125420. https://doi.org/10.1103/PhysRevB.90.125420.

(274) Naik, G. V; Saha, B.; Liu, J.; Saber, S. M.; Stach, E. A.; Irudayaraj, J. M. K.; Sands, T. D.; Shalaev, V. M.; Boltasseva, A. Epitaxial Superlattices with Titanium Nitride as a Plasmonic Component for Optical Hyperbolic Metamaterials. *Proc. Natl. Acad. Sci.* **2014**, *111* (21), 7546–7551. https://doi.org/10.1073/pnas.1319446111.

(275) Chaudhuri, K.; Shaltout, A.; Shah, D.; Guler, U.; Dutta, A.; Shalaev, V. M.; Boltasseva, A. Photonic Spin Hall Effect in Robust Phase Gradient Metasurfaces Utilizing Transition Metal Nitrides. *ACS Photonics* **2019**, *6* (1), 99–106. https://doi.org/10.1021/acsphotonics.8b00943.

(276) Riedl J, M. *Optical Design Fundamentals for Infrared Systems*, Second Edi.; SPIE Press Book, 2001.

(277) Yang, Y.; Kravchenko, I. I.; Briggs, D. P.; Valentine, J. All-Dielectric Metasurface Analogue of Electromagnetically Induced Transparency. *Nat. Commun.* **2014**, *5*, 5753. https://doi.org/10.1038/ncomms6753.

(278) Campione, S.; Liu, S.; Basilio, L. I.; Warne, L. K.; Langston, W. L.; Luk, T. S.; Wendt, J. R.; Reno, J. L.; Keeler, G. A.; Brener, I.; et al. Broken Symmetry Dielectric Resonators for High Quality Factor Fano Metasurfaces. *ACS Photonics* **2016**, *3* (12), 2362–2367. https://doi.org/10.1021/acsphotonics.6b00556.

(279) Hsu, C. W.; Zhen, B.; Lee, J.; Chua, S.-L.; Johnson, S. G.; Joannopoulos, J. D.; Soljačić, M. Observation of Trapped Light within the Radiation Continuum. *Nature* **2013**, *499* (7457), 188–191. https://doi.org/10.1038/nature12289.

(280) Friedrich, H.; Wintgen, D. *Interfering Resonances and Bound States in the Continuum DECEMBER 1985*; Vol. 32.

(281) Marinica, D. C.; Borisov, A. G.; Shabanov, S. V. Bound States in the Continuum in Photonics. *Phys. Rev. Lett.* **2008**, *100* (18), 183902. https://doi.org/10.1103/PhysRevLett.100.183902.

(282) Azzam, S. I.; Shalaev, V. M.; Boltasseva, A.; Kildishev, A. V. Formation of Bound States in the Continuum in Hybrid Plasmonic-Photonic Systems. *Phys. Rev. Lett.* **2018**, *121* (25), 253901. https://doi.org/10.1103/PhysRevLett.121.253901.

(283) Hsu, C. W.; Zhen, B.; Stone, A. D.; Joannopoulos, J. D.; Soljačić, M. Bound States in the Continuum. *Nat. Rev. Mater.* **2016**, *1* (9), 16048. https://doi.org/10.1038/natrevmats.2016.48.

(284) Rybin, M. V.; Koshelev, K. L.; Sadrieva, Z. F.; Samusev, K. B.; Bogdanov, A. A.; Limonov, M. F.; Kivshar, Y. S. High- Q Supercavity Modes in Subwavelength Dielectric Resonators. *Phys. Rev. Lett.* **2017**, *119* (24), 243901. https://doi.org/10.1103/PhysRevLett.119.243901.

(285) Kodigala, A.; Lepetit, T.; Gu, Q.; Bahari, B.; Fainman, Y.; Kanté, B. Lasing Action from Photonic Bound States in Continuum. *Nature* **2017**, *541* (7636), 196–199. https://doi.org/10.1038/nature20799.

(286) Krasnok, A.; Alú, A. Embedded Scattering Eigenstates Using Resonant Metasurfaces. *J. Opt.* **2018**, *20* (6), 064002. https://doi.org/10.1088/2040-8986/aac1d6.

VITA

Krishnakali Chaudhuri received her bachelor's degree (B. Tech.) in Electronics and Communications Engineering from MCKV Institute of Engineering, West Bengal University of Technology, India in 2009. She received her master's in technology (M. Tech.) degree in Electrical Engineering from the Indian Institute of Technology Bombay, India in 2013 from the research group of Professor Saurabh V. Lodha where she worked on developing germanium-based CMOS logic devices. She is currently a doctoral degree (Ph. D.) candidate in the research group of Professor Alexandra Boltasseva in the School of Electrical and Computer Engineering at Purdue University, West Lafayette, Indiana. Her current research focuses on nanophotonics and plasmonics. Goal of her research is to create a wholesome solution for the maturation of plasmonic metasurfaces from laboratory to industry scale, real life applications through successful utilization and integration of various, alternative and emerging material platforms into development of efficient, practically-realizable, functional devices.

LIST OF PUBLICATIONS (JOURNALS, BOOK CHAPTER, PATENT)

1. **Krishnakali Chaudhuri**, Mohamed Alhabeb, Zhuoxian Wang, Vladimir M. Shalaev, Yury Gogotsi, and Alexandra Boltasseva, Highly Broadband Absorber Using Plasmonic Titanium Carbide (MXene). *ACS Photonics* **2018**, *5* (3), 1115–1122.

2. **Krishnakali Chaudhuri**, Amr M. Shaltout, Urcan Guler, Deesha Shah, Aveek Dutta, Vladimir M. Shalaev, and Alexandra Boltasseva, Photonic Spin Hall Effect in Robust Phase Gradient Metasurfaces Utilizing Transition Metal Nitrides. *ACS Photonics* **2019**, *6* (1), 99–106.

3. **Krishnakali Chaudhuri,** Zhuoxian Wang, Mohamed Alhabeb, Kathleen Maleski, Yury Gogotsi, Vladimir M. Shalaev, Alexandra Boltasseva, Chapter 4.4- Optical Properties of MXenes in 2D Metal Carbides and Nitrides (MXenes): Structures, Properties and Applications (*in Press*)

4. **Krishnakali Chaudhuri***, Urcan Guler*, Shaimaa I. Azzam, Harsha Reddy, Alexander Kildishev, Vladimir M. Shalaev, Alexandra Boltasseva, Naophotonic Metamaterials Based Surface Temperature Sensor for Extreme Environments, (*In Preparation*)

5. Clayton T. DeVault, Vladimir A. Zenin, Anders Pors, **Krishnakali Chaudhuri**, Jongbum Kim, Alexandra Boltasseva, Vladimir M. Shalaev, and Sergey. I. Bozhevolnyi, Suppression of Near-Field Coupling in Plasmonic Antennas on Epsilon-near-Zero Substrates. *Optica* **2018**, *5* (12), 1557.

6. Sajid M. Choudhary, Di Wang, **Krishnakali Chaudhuri**, Clayton T. DeVault, Alexander V. Kildishev, Alexandra Boltasseva, and Vladimir M. Shalaev, Material Platforms for Optical Metasurfaces. *Nanophotonics* **2018**, *7* (6), 959–987.

7. Harsha Reddy, Urcan Guler, **Krishnakali Chaudhuri**, Aveek Dutta, Alexander V. Kildishev, Vladimir M. Shalaev, and Alexandra Boltasseva, Temperature-Dependent Optical Properties of Single Crystalline and Polycrystalline Silver Thin Films. *ACS Photonics* **2017**, *4* (5), 1083–1091.

8. Manohar Chirumamilla, Anisha Chirumamilla, Yuanqing Yang, Alexander S. Roberts, Peter K. Kristensen, **Krishnakali Chaudhuri**, Alexandra Boltasseva, Duncan S. Sutherland, Sergey. I. Bozhevolnyi, and Kjeld PedersenLarge-Area Ultrabroadband Absorber for Solar Thermophotovoltaics Based on 3D Titanium Nitride Nanopillars. *Adv. Opt. Mater*. **2017**, *5* (22), 1700552.

9. Alexander. V. Kildishev, Urcan Guler, **Krishnakali Chaudhuri**, Shaimaa I. Azzam, Ernesto Marinero-Caceres, Harsha Reddy, Alexnadra Boltasseva, Vladimir M. Shalaev, Metamaterial Device and Method of Making the Save, *US Patent App*. *0329115A1*, 2018

10. Zhuoxian Wang, Shaimaa I Azzam, Xiangeng Meng, Mohamed Alhabeb, **Krishnakali Chaudhuri,** Kathleen Maleski, Young L. Kim, Alexander V. Kildishev, Vladimir M.

Shalaev, Yury Gogotsi, and Alexandra Boltasseva, Active Metamaterials Based on Monolayer Titanium Carbide MXene for Random Lasing, (*In Preparation*)

11. Piyush Bhatt, **Krishnakali Chaudhuri**, Shraddha Kothari, Aneesh Nainani, Saurabh Lodha, Germanium Oxynitride Gate Interlayer Dielectric Formed on Ge (100) Using Decoupled Plasma Nitridation. *Appl. Phys. Lett.* **2013**, *103* (17), 172107.

SELECTED CONFERENCE PUBLICATIONS

1. **Krishnakali Chaudhuri**, Mohamed Alhabeb, Zhuoxian Wang, Vladimir M. Shalaev, Yury Gogotsi, Alexandra Boltasseva, Plasmonic resonances in nanostructured MXene: Highly broadband absorber, *2017 Conference on Lasers and Electro-Optics (CLEO)*

2. Urcan Guler, **Krishnakali Chaudhuri**, Shaimaa I. Azzam, Harsha Reddy, Alexander V. Kildishev, Vladimir M. Shalaev, Alexandra Boltasseva, High Temperature Sensing with Refractory Plasmonic Metasurfaces, *2018 12th International Congress on Artificial Materials for Novel Wave Phenomena (Metamaterials)*

3. Zhuoxian Wang, **Krishnakali Chaudhuri**, Mohamed Alhabeb, Xiangeng Meng, Shaimaa I Azzam, Alexander Kildishev, Young L Kim, Vladimir M Shalaev, Yury Gogotsi, Alexandra Boltasseva, MXenes for Plasmonic and Metamaterial Devices, *2018 Conference on Lasers and Electro-Optics (CLEO)*

4. **Krishnakali Chaudhuri**, Amr M. Shaltout, Urcan Guler, Vladimir M. Shalaev, Alexandra Boltasseva, "High efficiency phase gradient metasurface using refractory plasmonic zirconium nitride", *2016 Conference on Lasers and Electro-Optics (CLEO)*

5. **Krishnakali Chaudhuri**, Zhuoxian Wang, Mohamed Alhabeb, Xiangeng Meng, Shaimaa I. Azzam, Alexander V. Kildishev, Vladimir M. Shalaev, Yury Gogotsi, and Alexandra Boltasseva, MXenes for applications in nanophotonics, *Material Research Society Fall meeting, 2017*

6. **Krishnakali Chaudhuri**, Mohamed Alhabeb, Zhouxian Wang, Vladimir M. Shalaev, Yury Gogotsi, Alexandra Boltasseva, Plasmonic MXene for broadband absorber, *SPIE Optics and Photonics, 2017*

7. Zhouxiab Wang, Deesha Shah, **Krishnakali Chaudhuri**, Alessandra Catellani, Mohamed Alhabeb, Harsha Reddy, Xiangeng Meng, Shaimaa I. Azzam, Nathaniel Kinsey, Alexander V. Kildishev, Young L. Kim, Vladimir M. Shalaev, Arrigo Calzolari, Yury Gogotsi, Alexandra Boltasseva, Emerging materials for tailorable nanophotonic devices, *2018 12th International Congress on Artificial Materials for Novel Wave Phenomena (Metamaterials)*

8. Harsha Reddy, Urcan Guler, **Krishnakali Chaudhuri**, Aveek Dutta, Alexander V Kildishev, Vladimir M Shalaev, Alexandra Boltasseva, Temperature induced deviations to the optical responses of plasmonic materials, *2017 Conference on Lasers and Electro-Optics (CLEO)*

9. Deesha Shah, **Krishnakali Chaudhuri**, Zhuoxian Wang, Alessandra Catellani, Mohamed Alhabeb, Harsha Reddy, Xiangeng Meng, Shaimaa Azzam, Nathaniel Kinsey, Alexander Kildishev, Young Kim, Vladimir Shalaev, Arrigo Calzolari, Yuri Gogotsi, Alexandra Boltasseva, New materials and approaches for tailorable nanophotonics (Conference Presentation), *Smart Photonic and Optoelectronic Integrated Circuits XXI 2019*

10. Aveek Dutta, Clayton DeVault, **Krishnakali Chaudhuri**, Soham Saha, Deesha Shah, Harsha Reddy, Urcan Guler, Alberto Naldoni, Vladimir M. Shalaev, and Alexandra Boltasseva, "Oxides and nitrides for nanophotonics and energy application", *2017 Conference on Lasers and Electro-Optics (CLEO)*

11. Clayton DeVault, Vladimir Zenin, Anders Pors, Jongbum Kim, **Krishnakali Chaudhuri**, Sergey I. Bozhevolnyi, Vladimir M. Shalaev, and Alexandra Boltasseva, Plasmonic antenna resonance pinning and suppression of near-field coupling from epsilon near zero substrate, *2017 Conference on Lasers and Electro-Optics (CLEO)*